Università di Pisa

Facoltà di Scienze Matematiche, Fisiche e Naturali

Dipartimento di Fisica "E. Fermi"

CORSO DI LAUREA SPECIALISTICA IN SCIENZE FISICHE

Anno Accademico 2006 – 2007

Tesi di Laurea Specialistica:

Experimental Study of $W^{\pm}Z^{0}$ Intermediate Bosons Associated Production with the CDF Experiment at the Tevatron Collider

Candidato

Nicola Pozzobon

Relatori

prof. Giorgio Bellettini

dott. Gueorgui V. Velev

Contents

Introduction

Studying WZ associated production at the Fermilab Tevatron Collider is of great importance for two main reasons. On the one hand, this process would be sensitive to anomalies in the triple gauge couplings such that any deviation from the value predicted by the Standard Model would be indicative of new physics. In addition, by choosing to focus on the final state where the Z boson decays to $b\bar{b}$ pairs, the event topology would be the same as expected for associated production of a W and a Standard Model light Higgs boson ($m_H \lesssim 135$ GeV) which decays into $b\bar{b}$ pairs most of times. The process $WH \rightarrow Wb\bar{b}$ has an expected $\sigma \cdot B$ about five times lower than $WZ \rightarrow Wb\bar{b}$ for $m_H \simeq 120$ GeV. Therefore, observing this process would be a benchmark for an even more difficult search aiming at discovering the light Higgs in the $WH \rightarrow Wb\bar{b}$ process. After so many years of Tevatron operation only a weak WZ signal was recently observed in the full leptonic decay channel, which suffers from much less competition from background. Searching for the Z in the $b\bar{b}$ decay channel in this process is clearly a very challenging endeavour.

In the work described in this thesis, WZ production is searched for in a final state where the W decays leptonically to an electron-neutrino pair or a muon-neutrino pair, with associated production of a jet pair consistent with Z decays. A set of candidate events is obtained by applying appropriate cuts to the parameters of events collected by wide acceptance leptonic triggers. To improve the signal fraction of the selected events, an algorithm was used to tag b-flavored jets by means of their content of long lived b-hadrons and corrections were developed to the jet algorithm to improve the b-jet energy resolution for a better reconstruction of the Z mass. In order to sense the presence of a signal one needs to estimate the amount of background. The relative content of heavy flavor jets in the dominant W+multijet background is assumed as predicted by theory. This technique was originally developed in CDF to measure the $t\bar{t}$ production cross section in the final state with $W + 3$ or more jets.

This thesis was conceived as the first attempt within CDF to apply a customized version of it to look for evidence of diboson production in the final state with a W and two jets. Extracting the signal in this channel is very hard since with such a small number of jets the background is two orders of magnitude greater than the signal. Moreover, since the signal to background ratio is very small, the expected sensitivity depends critically on the theoretical uncertainties on the amount of background. While work is in progress to understand this background more reliably, this analysis provides an estimate of the achievable upper limit on the WZ production cross section.

1. The $W^{\pm}$, Z^0 and Higgs Bosons in the Standard Model

1.1 The Standard Model

Most experimental data in particle physics can be explained to an impressively high precision by the so-called Standard Model (SM) of fundamental interactions. All known matter is built, according to the SM, from spin-$\frac{1}{2}$ fermions: six leptons and six quarks. Each fundamental fermion is associated to its antiparticle, which carries opposite quantum numbers. The interactions that fundamental particles experience are of four kinds: gravitational, electromagnetic, weak and strong. The SM is a gauge theory including electromagnetic, weak and strong interactions ("gauge forces"), while incorporating gravity is still an open problem. Electromagnetic and weak interactions are described by a single interaction, named electroweak (EW). The strong interaction is described by an additional Quantum-Chromo-Dynamical interaction (QCD). A scalar field, the Higgs field, permeates the physical vacuum breaking the symmetry of the theory and giving masses to fundamental bosons and fermions.

Leptons are sensitive only to gravitational and EW interactions. The six known leptons are the electron e^-, the muon μ^-, the tau-lepton τ^- and their associated neutrinos ν_e, ν_μ and ν_τ. Quarks are sensitive to gravitational, EW and strong interactions. The six known quarks are distinguished by the so-called flavor: up u, down d, charm c, strange s, top t and bottom b. Only up and down quarks are stable and build the ordinary matter. Except for the top quark, all quarks are bound to other quarks into composite hadrons, either baryons (three quarks or three antiquarks) or mesons (one quark and one antiquark). Since according to Fermi-Dirac statistics identical fermions cannot be bound in the same quantum state, this finding shows that quarks posses a new quantum number named "color". Two quarks of the same flavor bound by strong interaction in a baryon are in a different color state.

The gauge interactions of fermions are described by the SM in terms of exchanges of spin-1 gauge bosons. The EW interaction is propagated by a massless photon γ and by three massive bosons W^+, W^- and Z^0. The strong interaction between quarks is carried by eight massless colored gluons g.

In a gauge theory as the SM, the fundamental particles are described by quantized fields ψ and

their interactions are expressed by the Lagrangian density $\mathcal{L}$. Each transformation of the fields that leaves unchanged the action $S = \int \mathcal{L}(\psi, \delta\psi)\mathrm{d}^4x$ can be associated to a conserved quantity (Noether's theorem). The Lagrangian density for a free fermion described by a Dirac spinor ψ in SM is

$$\mathcal{L}_{free} = \bar{\psi}(i\partial\!\!\!/ - m)\psi \ , \tag{1.1}$$

where $\partial\!\!\!/ = \gamma^\mu\partial_\mu$ and the γ^μ are the Dirac matrices. If the relativistic expression for the EM scalar and vector potentials A^μ is associated to the photon field, the Lagrangian density yielding the Maxwell equations can be expressed as

$$\mathcal{L}_\gamma = -\frac{1}{4}F^{\mu\nu}F_{\mu\nu} \ , \tag{1.2}$$

where $F^{\mu\nu} = \partial^\mu A^\nu - \partial^\nu A^\mu$. If the charge density current $Q\bar{\psi}\gamma^\mu\psi$ is associated to the interacting particle of charge Q times the electron charge e, the full Quantum-Electro-Dynamics (QED) Lagrangian density can be written then as the sum of the free particle Lagrangian, the free field Lagrangian and the interaction Lagrangian:

$$\mathcal{L}_{QED} = \bar{\psi}(i\partial\!\!\!/ - m)\psi - \frac{1}{4}F^{\mu\nu}F_{\mu\nu} + QeA^\mu\bar{\psi}\gamma_\mu\psi \ . \tag{1.3}$$

QED processes can be perturbatively calculated according to the Feynman's rules, often shown in graphic graphic representations of the processes called Feynman diagrams. The strength of the interaction depends on the constant associated to each fermion-fermion-boson vertex in Feynman diagrams, called coupling constant. QED equation of motion are invariant under the U(1) gauge transformation $A^\mu(x) \to A^\mu(x) + \partial^\mu\Lambda(x)$ where $\Lambda(x)$ is a scalar function of the coordinates[(1)].

The observed weak interaction phenomena are consistent with the fermions being organized into doublets of weak isospin $\chi = (\psi_u, \psi_d)$. To account for this nature of the weak interaction and to include QED into this description, a $\mathrm{SU}(2) \otimes \mathrm{U}(1)$ gauge theory was proposed and set up by Glashow, Salam and Weinberg (GSW) [3]. The two sectors can in principle have two different coupling constants g and g'. Analogously to QED, three EW currents, that can be linked to the positive and negative charged current interactions and to the neutral current interaction, are defined as

$$J^i_\mu(x) = \bar{\chi}\gamma_\mu\frac{\sigma^i}{2}\chi \ , \tag{1.4}$$

where σ_i are the Pauli matrices, J_3 is the neutral current, while J_1 and J_2 are linear combinations of the charged ones. The definition of the weak current in (1.4) is consistent with the observation that it couples only to left handed (LH) fermions if χ, in the case of leptons, is replaced by

$$\chi_L = \begin{pmatrix} \nu_\ell \\ \ell^- \end{pmatrix}_L , \tag{1.5}$$

[(1)] Such a gauge transformation is called local.

where ℓ stands for e, μ or τ. In the original GSW SM, neutrinos are massless[(2)] and therefore the right handed (RH) fields are weak isospin singlets ℓ_R. The LH quark field expression must take into account the observation of flavor changing charged currents coupled to it:

$$\chi_L = \begin{pmatrix} u_i \\ d'_i \end{pmatrix}_L , \tag{1.6}$$

where the index i runs on the quark families with $u_1 = u$, $u_2 = c$ etc. The d'_i are the fields expressed in terms of the Cabibbo-Kobayashi-Maskawa quark mixing matrix

$$d' = V_{CKM} d = \begin{pmatrix} V_{ud} & V_{us} & V_{ub} \\ V_{cd} & V_{cs} & V_{cb} \\ V_{td} & V_{ts} & V_{tb} \end{pmatrix} \begin{pmatrix} d \\ s \\ b \end{pmatrix} \tag{1.7}$$

which is requested to be unitary. Since the EM interaction is experienced by RH fermions too, the EM current is expressed in function of the weak one as

$$J_\mu^{EM} = J_\mu^3 + \frac{1}{2} J_\mu^Y \ , \tag{1.8}$$

$$J_\mu^Y = \bar{\psi} \gamma_\mu Y \psi \ , \tag{1.9}$$

where ψ is the fermion field including both leptons and quarks. If the fermion weak isospin is T^3, the charge Q is related to it via the hypercharge $Y = 2 \cdot (Q - T^3)$. Left handed fermions have $T^3 = \frac{1}{2}$ while right handed have $T^3 = 0$. The interaction Lagrangian density is thus written, including EM interactions, in terms of the weak fields B_μ and $\mathbf{W}_\mu = (W_\mu^1, W_\mu^2, W_\mu^3)$ as

$$\mathcal{L}_{EW} = g \mathbf{J}_\mu \cdot \mathbf{W}^\mu + \frac{g'}{2} J_\mu^Y B^\mu \ . \tag{1.10}$$

According to (1.4), the physical carriers of the weak charged current interaction are $W^\pm = \frac{1}{\sqrt{2}} \left(W^1 \pm i W^2 \right)$. One can decouple the EM current from the weak neutral current by mixing W_μ^3 and B_μ:

$$A_\mu = \frac{g' W_\mu^3 + g B_\mu}{\sqrt{g^2 + g'^2}} = W_\mu^3 \sin\theta_W + B_\mu \cos\theta_W \ , \tag{1.11}$$

$$Z_\mu^0 = \frac{g W_\mu^3 - g' B_\mu}{\sqrt{g^2 + g'^2}} = W_\mu^3 \cos\theta_W - B_\mu \sin\theta_W \ , \tag{1.12}$$

where A is the photon field and Z^0 is the neutral carrier of the weak interaction. The angle θ_W is called weak mixing angle. The Lagrangian density of the EM interaction can be rewritten in terms of the couplings to the $\mathbf{W}$ and B bosons as

$$\mathcal{L}_{EM} = e A^\mu J_\mu^{EM} = A^\mu \left(g \sin\theta_W J_\mu^3 + g' \cos\theta_W \frac{J_\mu^Y}{2} \right) \ , \tag{1.13}$$

[(2)] This picture has been modified by the discovery made in the Nineties that neutrinos have a tiny but non-zero mass.

leptons								
	Q	T^3	Y	approx. mass	grav.	EM	weak	strong
ν_e	0	$+1/2$	$-1/2$	< 2 eV	✓		✓	
e^-	-1	$-1/2$	$-1/2$	511 keV	✓	✓	✓	
ν_μ	0	$+1/2$	$-1/2$	< 2 eV	✓		✓	
μ^-	-1	$-1/2$	$-1/2$	106 MeV	✓	✓	✓	
ν_τ	0	$+1/2$	$-1/2$	< 2 eV	✓		✓	
τ^-	-1	$-1/2$	$-1/2$	1.78 GeV	✓	✓	✓	
quarks								
	Q	T^3	Y	approx. mass	grav.	EM	weak	strong
u	$+2/3$	$+1/2$	$+1/6$	$1.5 \div 3$ MeV	✓	✓	✓	✓
d	$-1/3$	$-1/2$	$+1/6$	$3 \div 7$ MeV	✓	✓	✓	✓
c	$+2/3$	$+1/2$	$+1/6$	~ 1.25 GeV	✓	✓	✓	✓
s	$-1/3$	$-1/2$	$+1/6$	~ 95 MeV	✓	✓	✓	✓
t	$+2/3$	$+1/2$	$+1/6$	$170 \div 175$ GeV	✓	✓	✓	✓
b	$-1/3$	$-1/2$	$+1/6$	$4.2 \div 4.7$ GeV	✓	✓	✓	✓

Table 1.1: Summary of lepton and quark properties; the 4 rightmost columns refer to the interactions experienced by the different fermions.

while the request of consistency between (1.8) and (1.13) implies

$$e = g \sin\theta_W = g' \cos\theta_W \quad . \tag{1.14}$$

Finally the free field Lagrangian density for the physical $W^{\pm}$ and Z^0 bosons can be written in analogy with (1.2) as

$$\mathcal{L}_{W,Z} = -\frac{1}{2} W^{+\mu\nu} W^-_{\mu\nu} - \frac{1}{4} Z^{\mu\nu} Z_{\mu\nu} \quad , \tag{1.15}$$

where the $W^{\pm}_{\mu\nu}$ and $Z_{\mu\nu}$ tensors are defined in the same way as $F_{\mu\nu}$. The sectors of the Lagrangian density introduced so far leak of the interactions among the EW gauge bosons, which are explicitly written in (1.29).

The symmetry of the Lagrangian density described so far must be broken in order to allow for non-zero physical masses of the particles. This is done by introducing additional scalar fields that interact with both the fundamental fermions and the gauge bosons. Since the EW interactions are local and the masses of the particles are different from zero also when non interacting (during free propagation), the scalar field must be always locally present. The scalar field is then usually said to have a non vanishing vacuum expectation value (v.e.v.). This mechanism is called Higgs mechanism, after the name of the scientist who proposed it [4]. The additional terms of the Lagrangian density describing the scalar field interaction with the gauge bosons and with itself can be written as

$$\mathcal{L}_{\phi W,\phi\phi} = \left| \left(i\partial_\mu - g T_i W^i_\mu - g' \frac{Y}{2} B_\mu \right) \phi \right|^2 - \mu^2 \phi^\dagger \phi + \lambda (\phi^\dagger \phi)^2 \quad , \tag{1.16}$$

keeping only monomials up to dimension 4 in order to preserve the renormalizability of the theory. The choice fell on a SU(2) doublet of complex (charged) scalars with $Y = 1$

$$\phi = \begin{pmatrix} \phi^+ \\ \phi^0 \end{pmatrix} = \frac{1}{\sqrt{2}} \begin{pmatrix} \phi_1 + i\phi_2 \\ \phi_3 + i\phi_4 \end{pmatrix} \ . \tag{1.17}$$

The symmetry is broken if the minimum of the $V(\phi) = \mu^2 \phi^\dagger \phi + \ \lambda(\phi^\dagger \phi)^2$ potential occurs at $\langle \phi^\dagger \phi \rangle = v^2/2 \neq 0$, or, in other terms, if $\mu^2 = -\lambda v^2 < 0$. The gauge freedom allows to choose the scalar field in its ground state:

$$\phi = \begin{pmatrix} 0 \\ v/\sqrt{2} \end{pmatrix} \ . \tag{1.18}$$

Once (1.18) is substituted into (1.16), $\mathcal{L}_{\phi W,\phi\phi}$ contains a mass term for the $W^\pm$ fields equal to

$$m_W = \frac{gv}{2} \ , \tag{1.19}$$

while the photon field A remains without mass term (the symmetry is still unbroken) and the neutral weak boson Z^0 becomes massive with

$$m_Z = \frac{v}{2}\sqrt{g^2 + g'^2} \ . \tag{1.20}$$

The masses of the weak gauge bosons are related then in SM by the weak mixing angle[(3)]:

$$\sin^2 \theta_W = 1 - \left(\frac{m_W}{m_Z}\right)^2 = \begin{cases} 0.222^\star \\ 0.23152 \pm 0.00015^\ddagger \end{cases} \ . \tag{1.21}$$

Another useful parametrization of the ϕ doublet is the one in terms of the Higgs boson H:

$$\phi(x) = \frac{e^{i\pi_i(x)T^i}}{\sqrt{2}} \begin{pmatrix} 0 \\ v + H(x) \end{pmatrix} \ . \tag{1.22}$$

Going to the unitarity gauge, the expression of $V(\phi)$ in terms of (1.22) includes the mass term of the Higgs boson, which is expected to be

$$m_H = 2v\sqrt{\lambda} = \mu\sqrt{2} \ . \tag{1.23}$$

To get the fermion masses in the correct way from the Lagrangian density of the scalar-fermion interaction, the easiest way is to distinguish between upper and lower components of the fermion isospin doublets. For the lower components ($D = \ell_i,\ d_i'$) the Lagrangian density is

$$\mathcal{L}_{\phi D} = -g_D \left[\left(\bar{\psi}_L^U,\ \bar{\psi}_L^D\right) \begin{pmatrix} \phi^+ \\ \phi^0 \end{pmatrix} \psi_R^D + \bar{\psi}_R^D \left(\phi^{+\dagger},\ \phi^{0\dagger}\right) \begin{pmatrix} \psi_L^U \\ \psi_L^D \end{pmatrix} \right] \ , \tag{1.24}$$

[(3)] In (1.21), which is a first-order result that can be subject to further corrections: * =prediction from measured m_W and m_Z, ‡ =from the measured couplings to Z^0.

where g_D are the couplings of the fermions to the Higgs boson. $\mathcal{L}_{\phi D}$ can be rewritten in terms of the fermion masses $m_D = g_D v/\sqrt{2}$ as

$$\mathcal{L}_{\phi D} = -m_D \bar{\psi}^D \psi^D - \frac{m_D}{v} H \bar{\psi}^D \psi^D \ . \tag{1.25}$$

Substituting ϕ^+ with $\phi^{0\dagger}$ and ϕ^0 with $-(\phi^+)^\dagger$, an identical expression for the upper components ($U = \nu_i,\ u_i$) of the fermion doublets can be found:

$$\mathcal{L}_{\phi U} = -m_U \bar{\psi}^U \psi^U - \frac{m_U}{v} H \bar{\psi}^U \psi^U \ . \tag{1.26}$$

The remaining sector of SM, the Quantum-Chromo-Dynamics (QCD) deals with the strong interaction binding quarks into hadrons. Since the charge associated to the strong interaction is the color which occurrs into three different states ("red", "blue" and "green"), the structure of the interaction term is dependent on 8 gauge bosons A_a, whose physical states are called gluons (g):

$$\mathcal{L}_{QCD} = \bar{\psi}(i\partial\!\!\!/ - m)\psi - \frac{1}{4} G^{\mu\nu}_a G^a_{\mu\nu} - g_S \bar{\psi}\gamma_\mu T^a_S \psi A^\mu_a \ , \tag{1.27}$$

where the index a runs on the 8 bosons. However, to satisfy gauge invariance, the $G^a_{\mu\nu}$ tensor cannot be defined analogously to the $F_{\mu\nu}$ of QED:

$$G^a_{\mu\nu} = \partial_\mu A^a_\nu - \partial_\nu A^a_\mu - g_S f_{abc} A^b_\mu A^c_\nu \ , \tag{1.28}$$

where the f_{abc} are the structure constants of the SU(3) group: $[T^a_S,\ T^b_S] = i2 f_{abc} T^c_S$. The final gauge structure of SM is then $\mathrm{SU}(3)_C \otimes \mathrm{SU}(2)_L \otimes \mathrm{U}(1)_Y$:

$$\begin{aligned}
\mathcal{L}_{SM} = \ & i\bar{\psi}_L \partial\!\!\!/ \psi_L + i\bar{\psi}_R \partial\!\!\!/ \psi_R \\
& -\tfrac{1}{2} W^{+\mu\nu} W^-_{\mu\nu} - \tfrac{1}{4} Z^{\mu\nu} Z_{\mu\nu} - \tfrac{1}{4} F^{\mu\nu} F_{\mu\nu} \\
& +ig\cos\theta_W \left[\left(W^-_\mu W^+_\nu - W^-_\nu W^+_\mu \right) \partial^\mu Z^\nu + W^+_{\mu\nu} W^{-\mu} Z^\nu - W^-_{\mu\nu} W^{+\mu} Z^\nu \right] \\
& +ie \left[\left(W^-_\mu W^+_\nu - W^-_\nu W^+_\mu \right) \partial^\mu A^\nu + W^+_{\mu\nu} W^{-\mu} A^\nu - W^-_{\mu\nu} W^{+\mu} A^\nu \right] \\
& +g^2 \cos^2\theta_W \left(W^+_\mu W^-_\nu Z^\mu Z^\nu - W^+_\mu W^{-\mu} Z_\nu Z^\nu \right) \\
& +g^2 \left(W^+_\mu W^-_\nu A^\mu A^\nu - W^+_\mu W^{-\mu} A_\nu A^\nu \right) \\
& +eg\cos\theta_W \left[W^+_\mu W^-_\nu \left(Z^\mu A^\nu + Z^\nu A^\mu \right) - 2 W^+_\mu W^{-\mu} Z_\nu A^\nu \right] \\
& +\tfrac{1}{2} g^2 \left(W^+_\mu W^-_\nu \right) \left(W^{+\mu} W^{-\nu} - W^{+\nu} W^{-\mu} \right) \\
& -\tfrac{g}{\sqrt{2}} \left[W^+_\mu \left(\nu_L \gamma^\mu \ell_L + V_{CKM} u_L \gamma^\mu d_L \right) + \text{h. c.} \right] \\
& -\tfrac{g}{\cos\theta_W} Z_\mu \left(T^3 - Q \sin^2\theta_W \right) \bar{\psi}_{L,R} \gamma^\mu \psi_{L,R} - eQ A_\mu \bar{\psi}\gamma^\mu \psi \\
& -v \left(\lambda_\psi \bar{\psi}_L \psi_R + \text{h. c.} \right) - m^2_W W^{+\mu} W^-_\mu - \tfrac{m^2_W}{2\cos\theta_W} Z^\mu Z_\mu \\
& +\tfrac{1}{2} \partial_\mu H \partial^\mu H + \tfrac{g^2}{4} (2v + H) H \left(W^+_\mu W^{-\mu} + \tfrac{1}{2\cos^2\theta_W} Z_\mu Z^\mu \right) - \lambda_\psi H \bar{\psi}\psi \\
& +\lambda \left(\tfrac{3}{4} v^4 + 2v^3 H + 2v^2 H^2 + v H^3 + \tfrac{1}{4} H^4 \right) \\
& -\tfrac{1}{4} G^{\mu\nu}_a G^a_{\mu\nu} - g_S \bar{\psi}\gamma_\mu T^a_S \psi A^\mu_a \ .
\end{aligned} \tag{1.29}$$

gauge bosons									
	force	strength	range (m)	Q	mass (GeV)	grav.	EM	weak	strong
photon γ	EM	1	∞	0	$< 6 \cdot 10^{-26}$	✓			
$W^{\pm}$	weak	10^{-4}	10^{-18}	± 1	80.4	✓	✓	✓	
Z^0	weak	10^{-4}	10^{-18}	0	91.2	✓		✓	
gluon g	strong	60	10^{-15}	0	0	✓			✓
graviton	grav.	10^{-41}	∞	0	not yet obs.	✓			

Table 1.2: Summary of SM gauge bosons; altough the SM does not include a complete quantum theory of gravitation, the expected carrier of gravity, the "graviton", is included in the list; strength is expressed relative to EM interaction for 2 u quarks $3 \cdot 10^{-17}$m far from each other.

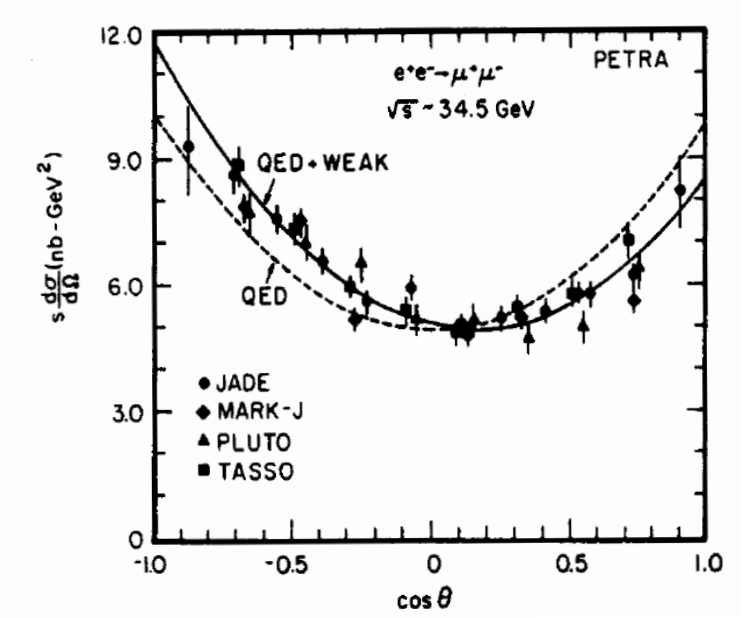

Figure 1.1: Compilation of the PETRA measurements for the angular distribution of $e^+e^- \to \mu^+\mu^-$ at 34.5 GeV center of mass energy. The full curve is a fit to the data allowing for an asymmetry. The dashed curve is for the symmetric QED prediction after correcting for a small asymmetry from α^3 diagrams.

1.2 Discovery of the W and Z Bosons

The evidence of massive carriers of weak interactions was clear after the $e^+e^- \to \mu^+\mu^-$ cross section measurements at PETRA (DESY), which showed a remarkable forward/backward asymmetry due to the γ/Z interference (Figure 1.1, [5]).

The direct search for W and Z bosons started with the construction of the CERN Sp$\bar{p}$S $p\bar{p}$ collider[4]. Two of the experiments housed at the Sp$\bar{p}$S, UA1 and UA2, were dedicated mainly to this search. UA1 was a 4π spectrometer exploiting a dipolar magnetic field designed to fully reconstruct a $p\bar{p}$ event and identify electrons and muons in gauge bosons decays. The tracking chamber immersed in the magnetic field was surrounded by EM and hadronic calorimeters up to 0.2° from the beam. Iron absorbers and tracking chambers for muon identification completed the apparatus, which is shown in Figure 1.2.

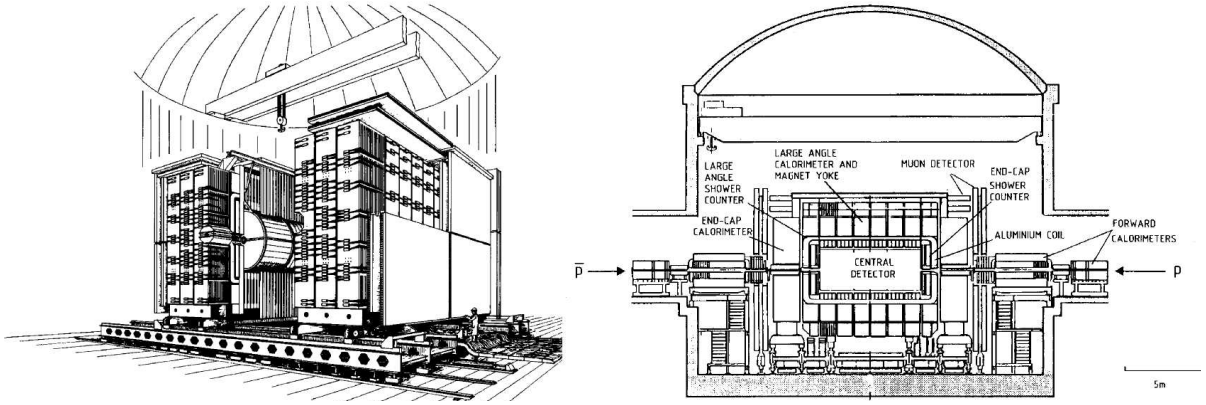

Figure 1.2: Schematic view of the UA1 detector.

UA2 (Figure 1.3) was a compact calorimetric detector designed to search for W and Z decaying into first generation leptons and tuned to high p_T jets studies. In its first generation version, at the time of W and Z discovery, it consisted of a small vertex tracking chamber, two toroidal spectrometer magnets in the forward region and highly segmented calorimeters covering the central region.

The search for W was carried on looking for W decaying to any lepton-neutrino pair of the firs two generations $W \to e\nu_e$, $W \to \mu\nu_\mu$. Lepton identification in UA1 and UA2 relied on calorimetric energy deposition and charged particle tracking (electrons) or high penetration power and charged particle tracking (muons, UA1 only), while the presence of neutrinos was inferred by the unbalance of the total transverse momentum. In the W^+ rest frame the differential cross section

[4] A clear and exaustive description of the discovery of W and Z bosons, together with more technical details on the experimental apparati and on the mechanism of W and Z production, can be found in [6].

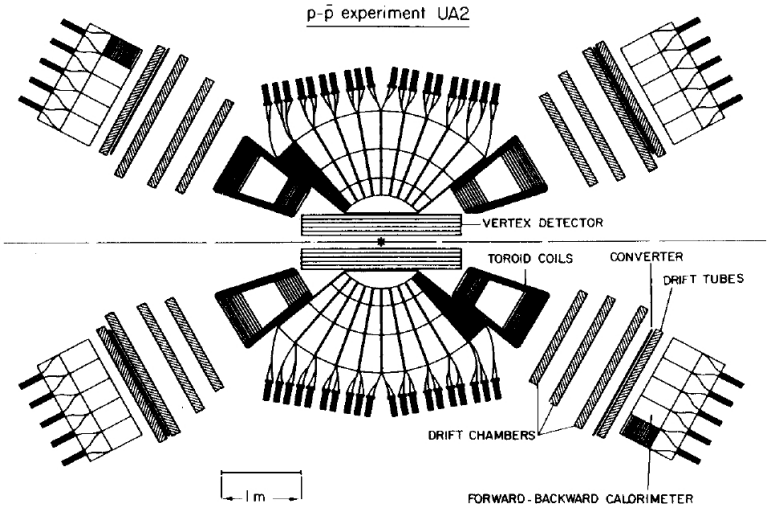

Figure 1.3: Schematic view of the UA2 detector.

behavior is

$$\frac{\mathrm{d}\sigma}{\mathrm{d}\cos\theta^*} \propto (1+\cos\theta^*)^2 \ , \tag{1.30}$$

where θ^* is the angle between the charged lepton momentum and the proton beam direction. Since θ^* is not measurable, one must make use of the p_T of the lepton to get an expression of the cross section in terms of measurable quantities in the laboratory frame. The lepton transverse momentum is invariant between the two frames if the W transverse momentum is neglected such that the W frame is boosted in the beam direction. Then, by expressing the transverse momentum in terms of θ^*

$$p_T = \frac{m_W}{2}\sin\theta^* \ , \quad \cos\theta^* = \sqrt{1-\left(\frac{2p_T}{m_W}\right)^2} \ , \tag{1.31}$$

one finally gets

$$\frac{\mathrm{d}\sigma}{\mathrm{d}p_T} = \frac{\mathrm{d}\sigma}{\mathrm{d}\cos\theta^*}\frac{\mathrm{d}\cos\theta^*}{\mathrm{d}p_T} \propto \left(\frac{m_W^2-2p_T^2}{m_W}\frac{1}{\sqrt{m_W^2-4p_T^2}}+1\right)\cdot\frac{4p_T}{m_W^2} \ . \tag{1.32}$$

This cross section is hence peaked at $p_T = m_W/2$ (Jacobean peak), but can be sensitive to the W transverse momentum if this is not null. This sensitivity is strongly reduced by using the transverse mass m_T instead of p_T:

$$m_T^2 = (E_{T_\ell}+E_{T_\nu})^2 - (\mathbf{p}_{T_\ell}+\mathbf{p}_{T_\nu})^2 \ . \tag{1.33}$$

Figure 1.5 shows the transverse mass plots for the electron-neutrino pairs in UA1 and UA2 data obtained after imposing kinematical constraints such as the relative back-to-back azimuthal directions of the electron and neutrino momenta (Figure 1.4). The search for Z was performed

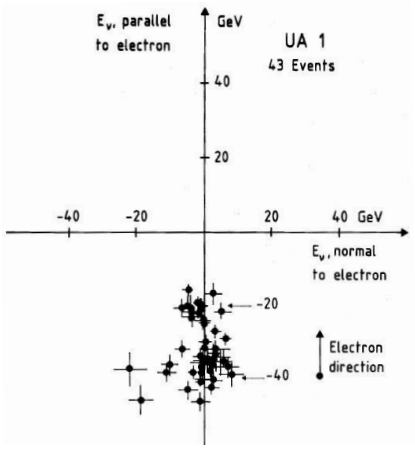

Figure 1.4: Two dimensional plot of the two azimuthal components of the missing transverse energy (neutrino momentum) relative to the electron direction (aligned along the positive y-axis in the plot) in UA1. This plot shows that the neutrino is emitted opposite to the charged lepton and with the same energy, as in the two-body decay of the W.

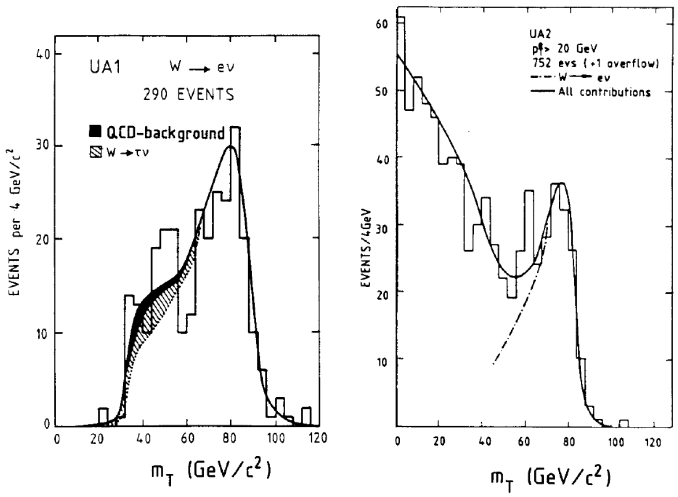

Figure 1.5: Electron-neutrino transverse mass plots of UA1 (left) and UA2 (right).

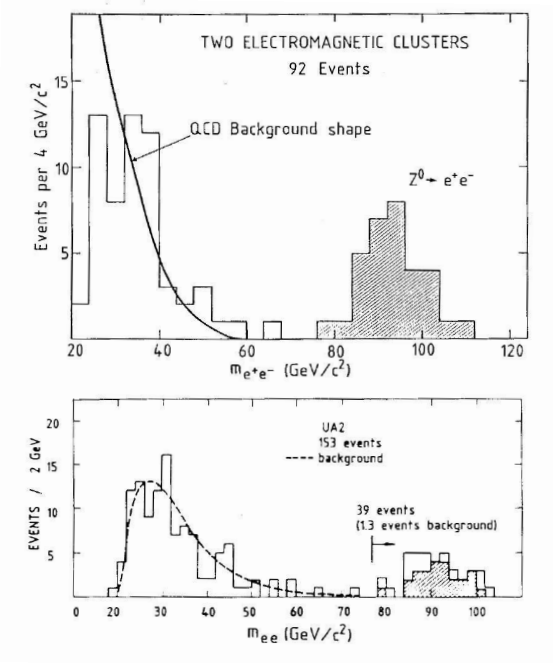

Figure 1.6: Electron-positron invariant mass plots for UA1 (top) and UA2 (bottom) collected data.

by looking for a peak in the invariant mass of opposite sign charged leptons (Figure 1.6). The discovery of the W boson which was announced in 1982 [7], followed next year by the Z one [8], is one of the most important results in experimental particle physics ever[(5)].

UA1 could observe decays of W and Z both in the e and μ channels. The UA2 experiment was not equipped with a muon detector but its calorimeters were capable of observing a weak signal of vector bosons decaying to hadrons, consisting of an excess of events with dijet invariant mass in W and Z mass region (Figure 1.7).

1.3 WZ Associated Production and Triple Gauge Couplings

The associated production of W and Z in $p\bar{p}$ collisions is described at leading order by two Feynman diagrams, the first one with fermionic propagator and the second one with virtual W propagator (Figure 1.8). The third and fourth line in (1.29) describe the WWZ and $WW\gamma$ couplings, called Triple Gauge Couplings (TGC), which can be measured by studying the diboson (WW, WZ and $W\gamma$) production. The virtual W propagator diagram in WZ production in particular is sensitive to the WWZ coupling.

[(5)] Carlo Rubbia, leading the UA1 collaboration, and Simon van Der Meer, inventor of the $\bar{p}$ cooling system used at Sp$\bar{p}$S, were awarded the 1984 Nobel Prize in Physics for the W and Z discovery.

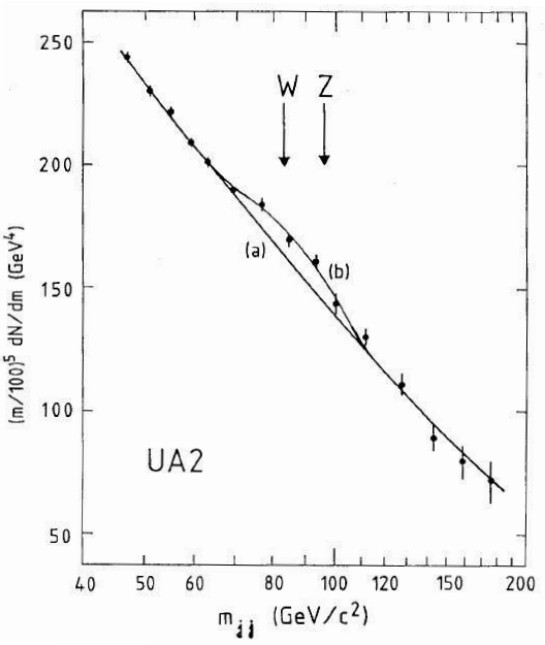

Figure 1.7: Invariant mass of the highest p_T jet pair obtained with UA2: an excess of data over the decreasing background in the IVB mass region is evident.

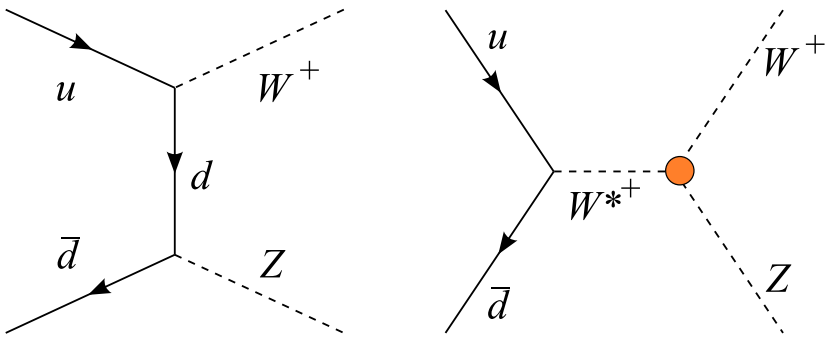

Figure 1.8: Leading order Feynman diagrams for WZ associated production in $p\bar{p}$ collisions with fermion propagator (left) and virtual W propagator (right): the latter one is sensitive to anomalous triple gauge couplings.

experiment	technique	$\int \mathcal{L} dt$	Λ	$\Delta\kappa$	λ
DØ	$WW \to \ell\ell\nu\nu$	250 pb^{-1}	1.5 TeV	$[-0.36, 0.47]$	$[-0.31, 0.33]$
DØ	$WW \to \ell\ell\nu\nu$	250 pb^{-1}	2.0 TeV	$[-0.32, 0.45]$	$[-0.29, 0.30]$
DØ	$W\gamma \to \ell\nu\gamma$	162 pb^{-1}	2.0 TeV	$[-0.88, 0.96]$	$[-0.20, 0.20]$
CDF	$W\gamma \to \ell\nu\gamma$	200 pb^{-1}	1.5 TeV	$[-0.74, 0.73]$	$[-0.21, 0.19]$
CDF	$WW, WZ \to \ell\nu$+jets	350 pb^{-1}	1.5 TeV	$[-0.50, 0.43]$	$[-0.28, 0.28]$

Table 1.3: Limits (95% CL) on the Anomalous Triple Gauge Couplings published by the CDF and DØ experiments; the table does not include the results from direct observation of WZ production, which are quoted in Section 1.4.

To account for non-SM physics, an effective theory can be built to describe the WWZ coupling [9], parametrizing the TGC in terms of 7 Anomalous Triple Gauge Couplings (ATGC), in the hypothesis of vector bosons coupled to massless fermions ($m_W \gg m_q$):

$$\begin{aligned}\mathcal{L}_{WWZ}/(-g\cos\theta_W) = \; & ig_1^Z \left(W^+_{\mu\nu} W^{-\mu} Z^\nu - W^+_\mu Z_\nu W^{-\mu\nu}\right) + i\kappa_Z W^+_\mu W^-_\nu Z^{\mu\nu} \\ & \tfrac{i\lambda_Z}{m_W^2} W^+_{\lambda\mu} W^{-\mu}{}_\nu Z^{\nu\lambda} - g_4^Z W^+_\mu W^-_\nu \left(\partial^\mu Z^\nu + \partial^\nu Z^\mu\right) \\ & + g_5^Z \varepsilon^{\mu\nu\rho\sigma} \left(W^+_\mu \left(\partial_\rho W^-_\nu\right) - \left(\partial_\rho W^+_\mu\right) W^-_\nu\right) Z_\sigma \\ & + i\tilde{\kappa}_Z W^+_\mu W^-_\nu \tfrac{1}{2}\varepsilon^{\mu\nu\rho\sigma} Z_{\rho\sigma} + \tfrac{i\tilde{\lambda}_Z}{m_W^2} W^+_{\lambda\mu} W^{-\mu}{}_\nu \tfrac{1}{2}\varepsilon^{\nu\lambda\rho\sigma} Z_{\rho\sigma} \; .\end{aligned} \tag{1.34}$$

$\mathcal{L}_{WWZ}$ can be reduced to the SM appearance at tree level if $g_1^Z = \kappa_Z = 1$ and $\lambda_Z = g_4^Z = g_5^Z = \tilde{\kappa}_Z = \tilde{\lambda}_Z = 0$. If the $WW\gamma$ coupling is considered instead of the WWZ one, the corresponding Lagrangian density remains unchanged in form, while by exploiting the relations between g, e, θ_W, A^μ and Z^μ one gets $\lambda_Z = \lambda_\gamma = \lambda$ and $\tilde{\lambda}_Z = \tilde{\lambda}_\gamma = \tilde{\lambda}$. If CP and gauge invariances are assumed, only four out of the 12 remaining couplings are independent and potentially different from zero: g_1^Z, $\kappa_{Z,\gamma}$ and λ. Under the further assuption[(6)] of equal ATGC for the WWZ and $WW\gamma$ vertices the set of parameters is finally reduced to two:

$$\lambda(\hat{s}) = \frac{\lambda}{(1+\hat{s}^2/\Lambda^2)^2} \;\; , \;\; \Delta\kappa(\hat{s}) = \frac{1-\kappa}{(1+\hat{s}^2/\Lambda^2)^2} \;\; , \tag{1.35}$$

where a form factor has been introduced in order to preserve unitarity. The actual limits on ATGC obtained at the Tevatron are shown in Table 1.3 [10].

1.4 Observations of WZ Associated Production at the Tevatron

WZ associated production was observed by both the CDF and DØ experiments [11] in the $\ell^+\ell^-\ell^\pm\nu$ final state. While WW production was available at LEP too, WZ production at a hadron collider

[(6)] This assumption is done in studies involving a WW final state, which is sensitive both to WWZ and $WW\gamma$ couplings. The results shown in Table 1.3 include the assumption that these couplings are equal to each other except for the $W\gamma$ results, where $\Delta\kappa$ sould be read as $\Delta\kappa_\gamma$.

Λ (TeV)	Δg_1^Z	$\Delta\kappa_Z$	λ_Z
1.0	$0^\star$	$0^\star$	$[-0.53, 0.56]$
1.5	$0^\star$	$0^\star$	$[-0.48, 0.48]$
1.0	$[-0.57, 0.76]$	$0^\star$	$0^\star$
1.5	$[-0.49, 0.66]$	$0^\star$	$0^\star$
1.0	$[-0.49, 0.66]$	$= \Delta g_1^{Z\star}$	$0^\star$
1.5	$[-0.43, 0.57]$	$= \Delta g_1^{Z\star}$	$0^\star$
1.0	$0^\star$	$[-2.0, 2.4]$	$0^\star$

Table 1.4: Limits (95% CL) on the Anomalous WWZ Couplings published by DØ jointly with the observation of WZ production, assumptions on couplings are marked with *.

offers an unique opportunity for the measurement of WWZ ATGC without the restrictions imposed by WW final states (Section 1.3).

The DØ observation was made on $\int \mathcal{L} dt \simeq 300$ pb^{-1}, searching for final states with three high p_T (> 15 GeV) charged leptons and large p_T unbalance (> 20 GeV, compatible with the presence of a neutrino from W decay). The Z boson is selected from oppositely charged electron (muon) pairs with invariant mass differing no more than 20 GeV (40 GeV) from the Z mass. The total number of observed events is three, one in the $e\nu ee$ channel and two in the $\mu\nu\mu\mu$ one. Since the total background is expected to be of 0.71 ± 0.08 events, the observation is claimed and a cross section is measured $\sigma_{WZ} = 4.5^{+3.8}_{-2.6}$ pb, where the quoted error includes systematic uncertainties. This value is in agreement with the NLO prediction of SM: $\sigma_{WZ}^{SM} = 3.96 \pm 0.06$ pb. Some limits on anomalous WWZ couplings[7] could be extracted under particular assumptions. The results are listed in Table 1.4.

The CDF Collaboration observed WZ production (Figure 1.9) in the same final state as DØ, unsing 1.1 fb^{-1} of integrated luminosity. The event selection requires 3 high p_T (> 20 GeV) charged leptons and large p_T unbalance (> 25 GeV). In order to limit the background due to detector malfunctioning, the angle between the direction of the candidate neutrino and any candidate lepton or reconstructed hadron jet is required to be greater than 9°. The flavor-like opposite-charge lepton pair is required to have invariant mass different from Z mass no more than 15 GeV. Further vetoes are applied to reject ZZ production. The total number of observed events is 16: six of $e\nu ee$ type, one of $e\nu\mu\mu$ type, one of $\mu\nu\mu\mu$ type, 8 with two well-identified leptons and one high p_T isolated track with unknown flavor. The total background is expected to be of 2.7 ± 0.4 events. The measured cross section is still in agreement with the SM prediction: $\sigma_{WZ} = 5.0^{+1.8}_{-1.4}$ (stat) ± 0.4 (syst) pb.

Some refinements of the described observations were presented in the latest conferences, in particular CDF was able to produce also limits on the WWZ coupling[8] [12]:

[7] Δg_1^Z is defined as $1 - g_1^Z$, in analogy with (1.35).
[8] The renormalization scale of the form factor is $\Lambda = 2$ TeV for both the results.

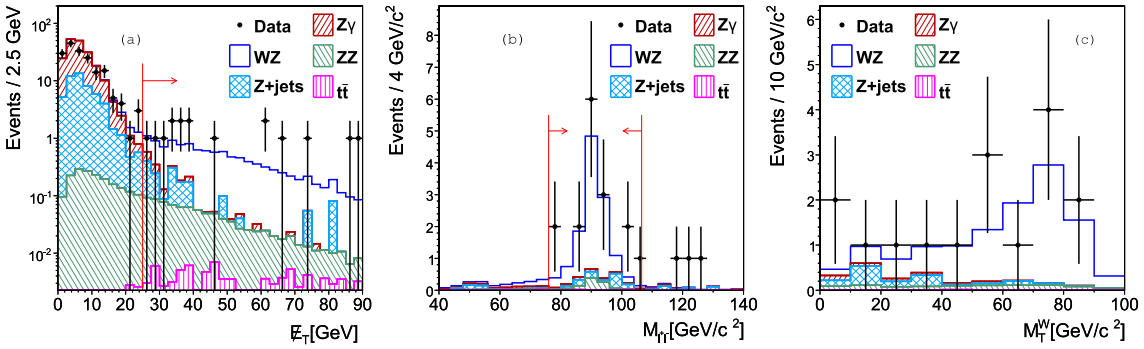

Figure 1.9: First observation of WZ production at CDF: distributions for WZ candidates of (left) $\not\!\!E_T$, (center) dilepton invariant mass of same-flavor opposite-sign dilepton pair closest to the Z mass and (right) W transverse mass calculated from the remaining lepton and the $\not\!\!E_T$; the signal region is identified by red arrows.

- DØ, on 1.0 fb^{-1} of collected data, produced a cross section measurement $\sigma_{WZ} = 2.7^{+1.7}_{-1.3}$ pb and 95% CL limits on the WWZ anomalous TGC: $-0.17 < \lambda_Z < 0.21$ (if $\Delta\kappa_Z = 0$) and $-0.12 < \Delta\kappa_Z = \Delta g_1^Z < 0.29$ (if $\lambda_Z = 0$);
- CDF, on 1.9 fb^{-1} of collected data, produced a cross section measurement $\sigma_{WZ} = 4.3^{+1.3}_{-1.0}$ (stat) ± 0.4 (syst) pb and 95% CL limits on each WWZ anomalous TCG, under the assumption of the other two being equal to zero: $-0.13 < \lambda_Z < 0.14$, $-0.15 < \Delta g_1^Z < 0.24$ and $-0.82 < \Delta\kappa_Z < 1.27$.

1.5 Looking Towards the SM Higgs Boson

WZ associated production in a final state involving hadrons has not been observed yet. It is natural to pursue this goal by looking for $Z \rightarrow$hadrons in a sample of inclusive $W \rightarrow \ell\nu$, which has a relatively large statistics. However, this search is particularly challenging because it is affected by a large background, whose cross section is orders of magnitude greater[9].

Two attempts of observing WZ production in the $\ell\nu+$ hadron jets final state have been made at CDF [13]. Both the searches are in reality inclusive searches for WW and WZ production. The first search was performed over 350 pb^{-1} of collected data. The W selection requires an electron with $E_T > 25$ GeV (or muon with $p_T > 20$ GeV), p_T of the candidate neutrino > 25 GeV and $\ell\nu$ transverse mass > 25 GeV. The selection of the second vector boson requires at least two jets in the $|\eta| < 2$ region (Section 3.1) reconstructed with a $R = 0.4$ cone algorithm (Section 4.4) and corrected $E_T > 20$ GeV (Section 5.1). Jets are required to be well separate from one

[9] The inclusive $p\bar{p} \rightarrow W + X$ cross section measured by CDF was $\sigma(p\bar{p} \rightarrow W + X) \cdot B(W \rightarrow e\nu) = 2780 \pm 14$ (stat only) pb, $\sigma(p\bar{p} \rightarrow W + X) \cdot B(W \rightarrow \mu\nu) = 2768 \pm 16$ (stat only) pb. These cross sections are 750 times larger than $\sigma(p\bar{p} \rightarrow WZ + X) \simeq 4$ pb, inclusive of all possible W and Z decays.

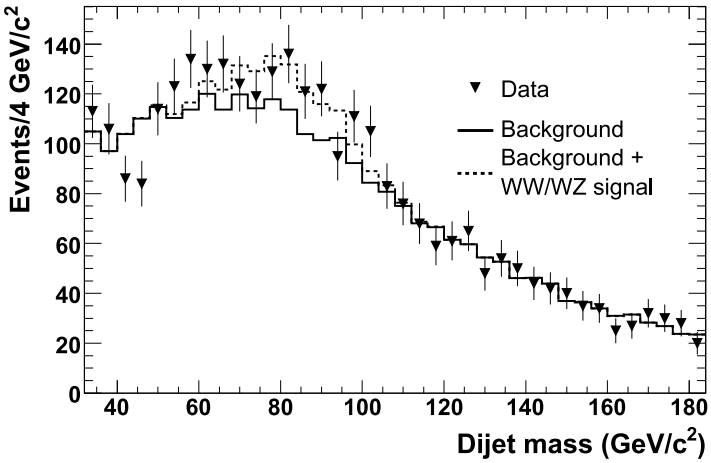

Figure 1.10: Search for WW and WZ production in $\ell\nu$+hadrons final state at CDF: invariant mass reconstructed from the two jets with highest E_T; the measured data are fitted to the hypothesis of combined signal and background shapes.

another and from the candidate charged lepton from W decay. The two highest p_T jets are associated to the second vector boson and their dijet invariant mass (Figure 1.10) is required to be in the $[56,113]$ GeV range. The main expected backgrounds arise from QCD multijet production, W+jets production and by other electroweak processes. This study could only produce a 95% CL upper limit to the $WW+WZ$ production cross section of 36 pb (SM expectation is ~ 16.5 pb).

In addition to this work, an attempt is currently on-going by another CDF group working on the total amount of collected data so far. This study is still in progress and only preliminary results in the $W \to e\nu$ channel have been presented in public conferences with ~ 1.3 fb^{-1} of collected data. The W selection requires an electron with $E_T > 10$ GeV and a p_T of the candidate neutrino greater than 25 GeV. The selection of the second vector boson requires at least two jets in the $|\eta| < 2.4$ region reconstructed with a $R = 0.4$ cone algorithm and corrected $E_T > 15$ GeV. The study relies on the analysis of the shape of the invariant mass distribution of the 2 leading jets selected in the event. The signal region is the one with dijet invariant mass comprised between 60 and 100 GeV. The background rejection is performed with a neural network trained on several variables mainly belonging to the kinematic description of jets in the event. A likelihood function depending on the $WW+WZ$ fraction is built and tested in the sidebands. The fit is then performed in the signal region allowing for signal contribution (Figure 1.11). The expected $\sigma \cdot B$ from SM is 2.1 pb, while the extracted limit from data is 3.4 pb (95% CL).

The large W+hadron jets background can be reduced by restricting the search for WZ in a final state with two quark jets of the same flavor as in Z decays. In practice, this can be done by tagging b-flavored jets, as several b-flavor jet tagging techniques have been developed in the

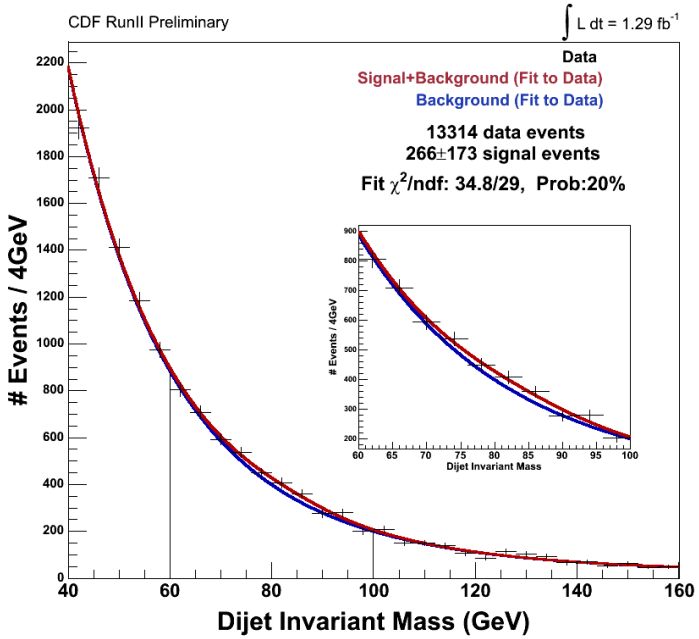

Figure 1.11: Search for WW and WZ production in $\ell\nu$+hadrons final state at CDF with neural network selection: invariant mass reconstructed from the two jets with highest E_T with the fit of the shape allowing for contribution from the signal.

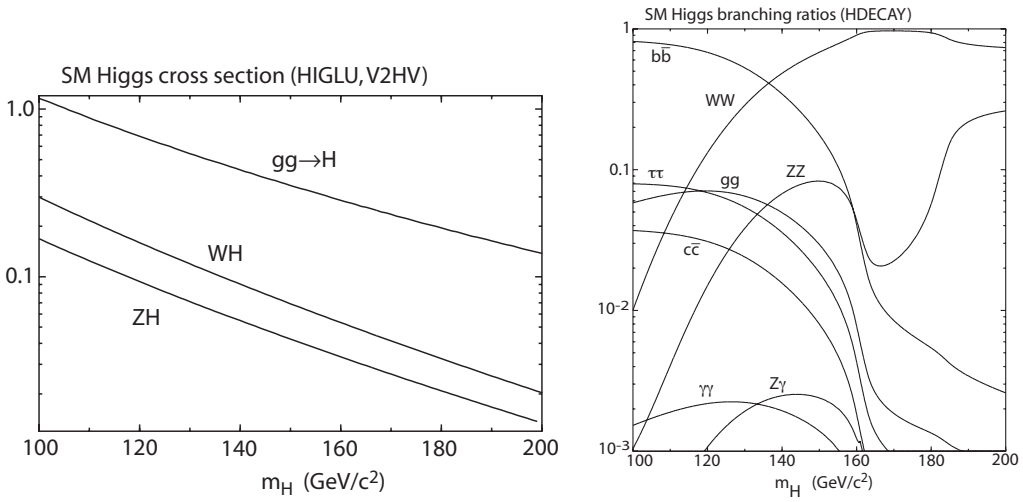

Figure 1.12: SM Higgs boson production cross section (in pb) at the Tevatron Collider (left) and branching ratios (right) as functions of H mass: the WH associated production even if carachterized by a lower cross section is the one leading to the the lowest background for a light Higgs boson.

years. Moreover, a reliable[10] procedure has been developed by CDF to discriminate between signal and background in W samples with identified b-flavored jets, in the course of the measurement of the $t\bar{t}$ production cross section. The work presented in this thesis is the first attempt to apply these powerful although complex tools in a new contest where the signal is smaller and the background is much larger than in the $t\bar{t}$ production[11].

Observing both the WW and WZ processes are fundamental steps in the search for a SM Higgs boson. Electroweak WW production is a background for a $H \to W^+W^-$ decay which is the dominant final state for Higgs masses $\gtrsim 140$ GeV, while the WZ production is a background for a lighter ($m_H \sim 120$ GeV) SM Higgs decaying to $b\bar{b}$ pairs. Since inclusive production of light Higgs which has the largest cross section competes with an insurmountable QCD background, the $W + b\bar{b}$ is actually the only final state where a light SM Higgs boson could be found in the next years. Being able to observe WZ production at the Tevatron is therefore fundamental to justify any hopes of finding the Higgs boson before the start of LHC.

[10] By "reliable" it is meant that the procedure was found to be effective in the particular kind of measurement it was developed for.

[11] $\sigma(p\bar{p} \to t\bar{t} + X) \sim 8$ pb, $B(t \to bW) \sim 1$ while $\sigma(p\bar{p} \to WZ + X) \sim 4$ pb, $B(Z \to b\bar{b}) \sim 0.15$.

2. The Tevatron Collider in Run II

The Tevatron Collider is the $p\bar{p}$ storage ring of Fermi National Accelerator Laboratory, located in Batavia, Illinois, about 45 km west of Chicago. With its c.m.s. energy of $\sqrt{s} = 1.96$ TeV, the Tevatron provides the highest energy particle collisions available until the CERN Large Hadron Collider is completed and operating.

The Tevatron Collider is part of the Fermilab Accelerator Chain (Figure 2.1), which is composed by several machines that drive protons and antiprotons from production up to a momentum of 980 GeV [15]. These main components are:

- the proton source, including a linear accelerator and a booster synchrotron;
- the Main Injector, feeding the antiproton source and the Tevatron collider;
- the antiproton source, including a debuncher, an accumulator and a recycler ring;
- the Tevatron;
- the extraction lines to fixed target experiment (not described below).

The so-called Run II is the data acquistion period which started in 2002 and is expected to end in autumn 2009.

2.1 The Proton Source

Protons are produced from gaseous hydrogen H_2, which is negatively ionized to be accelerated by a 750 kV Cockroft-Walton DC accelerator. Negative H^- ions are produced in two steps: first the H_2 molecule is broken and the electrons are stripped away from the hydrogen atom by an electric field. These protons are then collected on a negatively charged Cs-doped metal surface, where they are linked to two free electrons. H^- ions are kicked away by other incoming protons and move away from the metal surface because of their like-sign charge (Figure 2.2).

750 keV H^- ions are then accelerated up to 400 MeV by a 130 m long Alvarez type linear accelerator. The H^- beam pulse lasts typically 20 ms and is injected into a booster synchrotron. When entering the booster, H^- ions pass through a carbon foil where the two electrons are removed. The booster has a circumference of 475 m and accelerates protons from $p = 400$ MeV to

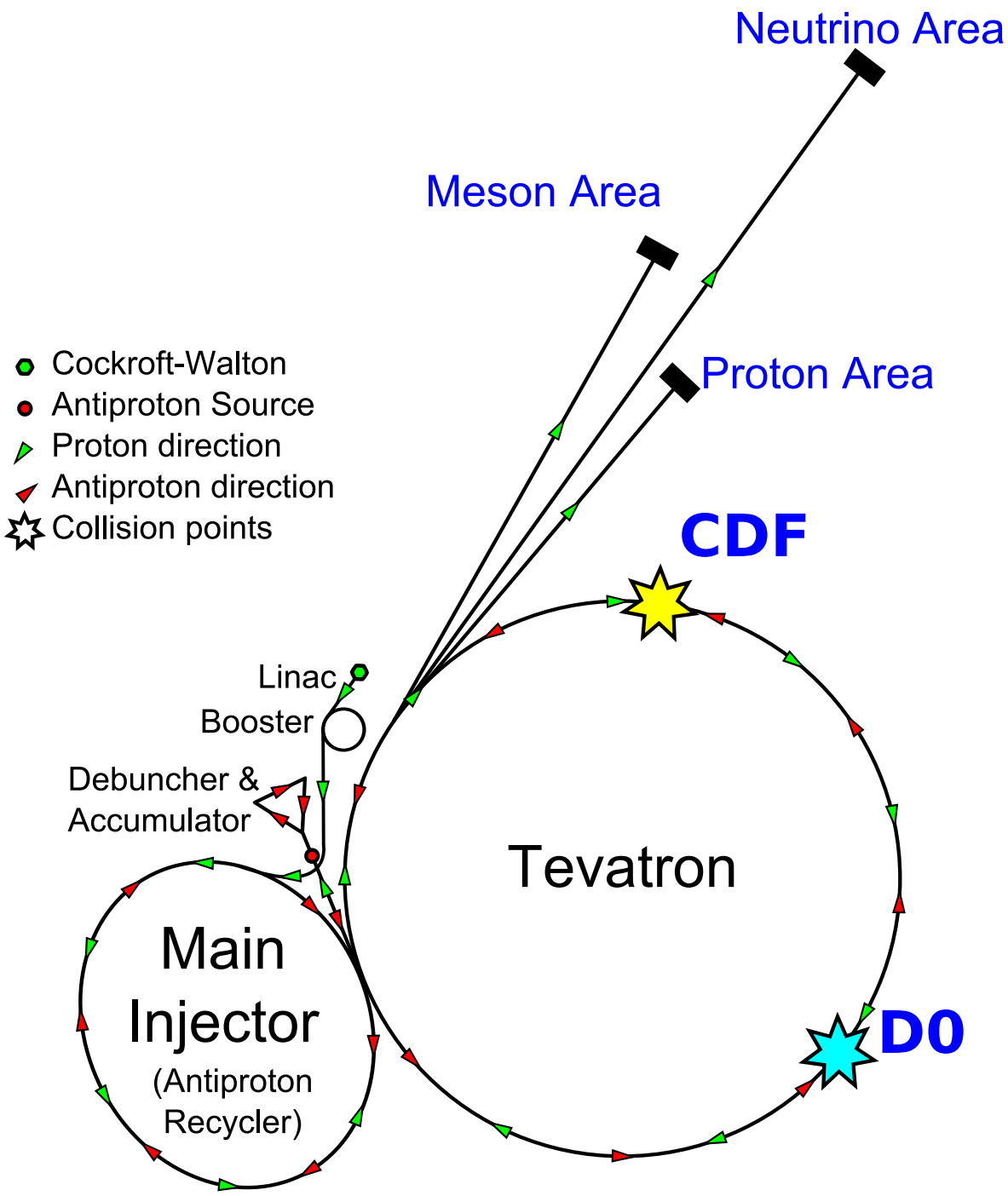

Figure 2.1: The Fermilab accelerator chain.

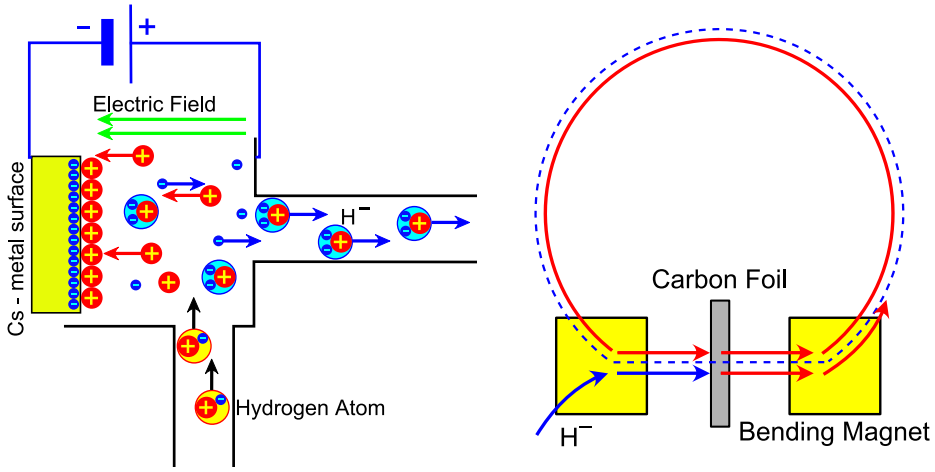

Figure 2.2: H^- ions production (left) and multiturn injection in the booster (right).

$p = 8$ GeV. Since the Linac pulse lasts longer than the revolution period in the booster (2.2 ms), injection is performed in a multi-turn booster cicle (Figure 2.2).

2.2 The Main Injector

Protons exiting the booster with a momentum of 8 GeV are transferred to the Main Injector. This synchrotron was built as un upgrade of the Fermilab accelerator chain that took place between 1998 and 2002 to achieve better Tevatron performances in Run II. The Main Injector replaced the Main Ring, an older synchrotron of similar energy which was housed in the Tevatron tunnel. The Main Injector carries more current with faster cycling rate than the Main Ring, leading to a higher luminosity of the Tevatron Collider. Protons are extracted at 120 GeV for $\bar{p}$ production and for fixed target experiments, while protons and antiprotons are extracted at 150 GeV for the final injection into the Tevatron.

2.3 The Antiproton Source

The Tevatron operates as a $p\bar{p}$ collider where a proton and an antiproton beam run in opposite directions in the same accelerator vacuum pipe. Except for this technical advantage (one only synchrotron rather than two) there is only a minimal or no advantage versus a proton-proton collider in the reach for large p_T physics studies[(1)].

The radiofrequency bunched proton beam is extracted from the Main Injector at 120 GeV and brought to collide against a 7 cm thick nickel target, where many secondary particles, including

[(1)]The slightly greater production cross section for interesting processes (e.g. the $t\bar{t}$ production) is an advantage that disappears at a c.m.s energy of $\sqrt{s} \simeq 3$ TeV.

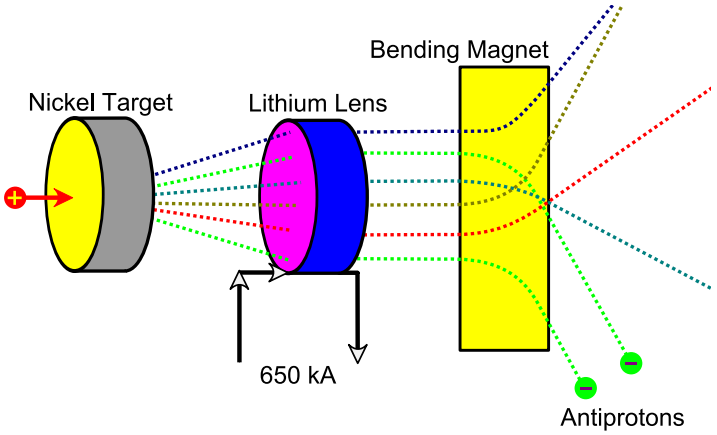

Figure 2.3: Antiproton production target.

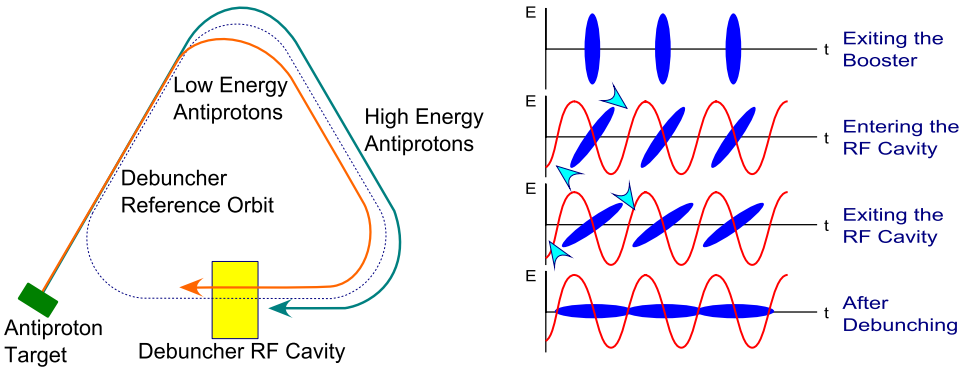

Figure 2.4: Debuncher operation (left) and evolution of the longitudinal phase space diagram during the debunching (right).

antiprotons, are produced. The produced particles are focussed by a lithium lens and analyzed in a magnetic spectrometer selecting negatively charged particles in the p mass range. Antiprotons are produced over a wide momentum range, with a broad maximum around 8 GeV and an efficiency of about $2 \cdot 10^{-5}$ per interacting proton. This system is pictured qualitatively in Figure 2.3.

The bunched antiproton beam is accepted with a momentum spread of about 2.5% by a "debuncher" synchrotron where, by radiofrequency manipulation, it is turned into a continuous nearly monochromatic 8 GeV beam, as shown in Figure 2.4.

The $\bar{p}$ debunched beam is transferred to the Accumulator Ring, housed in the same tunnel of the debuncher, which collects pulses from the debuncher over a long period of time, usually many hours. In the accumulator a higher intensity antiproton beam is stored, as much as allowed by its larger acceptance. In both the debuncher and the accumulator the longitudinal and transverse

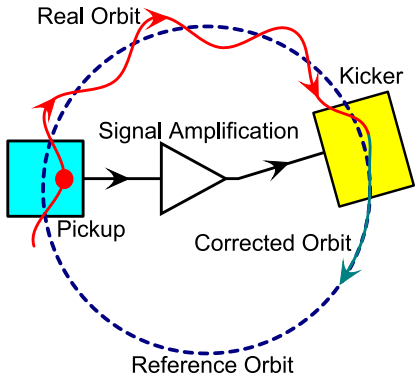

Figure 2.5: Stochastic $\bar{p}$ cooling.

momentum spread of the beam is reduced ("cooled") by stochastic cooling[(2)].

2.4 The Recycler

The "recycler" is an antiproton accumulator of increased acceptance housed in the tunnel of the Main Injector. When the beam has filled the accumulator acceptance it is transferred to the recycler where approximately twice more current can be stored, up to about 350 mA. The recycler is a static 8 GeV storage ring realized with ferrite permanent magnets, supported only by a relatively small number of corrector electromagnets.

2.5 The Tevatron Collider

The Tevatron sarted operating in 1975 as the first superconducting synchrotron. Since the year 2002 it operated only in the collider mode. It employs about 1000 dipole bending magnets with niobium-titanium superconducting coils in a 1 km radius ring. Each dipole magnet (Figure 2.6) is 6.4 m long and is cooled with liquid helium down to 4.3 K. The magnetic field inside the dipoles reaches 4.2 T while the proton/antiproton beam momentum is 980 GeV. In the two high-luminosity interaction points, conventionally named B0 and D0, the colliding beams are shrunk to a diameter of approximate Gaussian shape with about 32 μm width. The main features of Tevatron in history are listed in Table 2.1.

While in previous runs the Tevatron Collider operated with a smaller number of beam bunches (6 at the end of Run I in 1998), in the on-going Run II the Collider operates with 36×36 bunches. By doing this, the instantaneous luminosity could be increased while limiting the number of

[(2)]The principle of stochastic cooling is illustrated in Figure 2.5. An "error signal" on the energy or position of a lump of particles is picked up along the orbit, amplified and driven to generate a correction pulse after an odd number of betatron oscillation half-periods.

RUN	Run Ib	Run IIa	Run IIa	Run IIb
p bunches $\times \bar{p}$ bunches	6×6	36×36	140×103	140×103
p/bunch	$2.3 \cdot 10^{11}$	$2.7 \cdot 10^{11}$	$2.7 \cdot 10^{11}$	$2.7 \cdot 10^{11}$
$\bar{p}$/bunch	$5.5 \cdot 10^{10}$	$3.0 \cdot 10^{10}$	$4.0 \cdot 10^{10}$	$1.0 \cdot 10^{11}$
Total antiprotons	$3.3 \cdot 10^{11}$	$1.1 \cdot 10^{12}$	$4.2 \cdot 10^{12}$	$1.1 \cdot 10^{13}$
$\bar{p}$ production rate (hr^{-1})	$6.0 \cdot 10^{10}$	$1.0 \cdot 10^{11}$	$2.1 \cdot 10^{11}$	$5.2 \cdot 10^{11}$
p emittance (mm·mrad)	23π	20π	20π	20π
$\bar{p}$ emittance (mm·mrad)	13π	15π	15π	15π
β^* (cm)	35	35	35	35
$\sqrt{s}$ (GeV)	1.8	1.96	1.96	1.96
Bunch length RMS (m)	0.60	0.37	0.37	0.37
Crossing angle (μrad)	0	0	136	136
Design $\mathcal{L}$ ($\mathrm{cm}^{-2}\mathrm{s}^{-1}$)	$0.16 \cdot 10^{31}$	$0.86 \cdot 10^{32}$	$2.1 \cdot 10^{32}$	$5.2 \cdot 10^{32}$
$\int \mathcal{L} dt$ (pb^{-1}/week)	3.2	17.3	42	105
Bunch spacing (ns)	~ 3500	396	132	132
Interactions/crossing	2.5	2.3	1.9	4.8

Table 2.1: Main Tevatron performance parameters since 1993. In the current phase of Run II the number of bunches has been reset to 36×36 and the increase of the luminosity has been obtained by improving the antiproton storage.

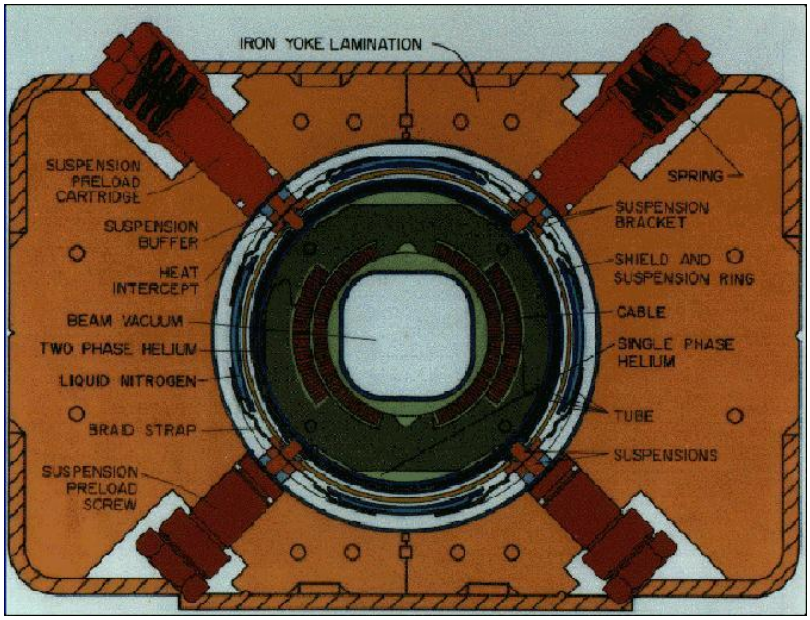

Figure 2.6: Cross section of a superconducting Tevatron magnet.

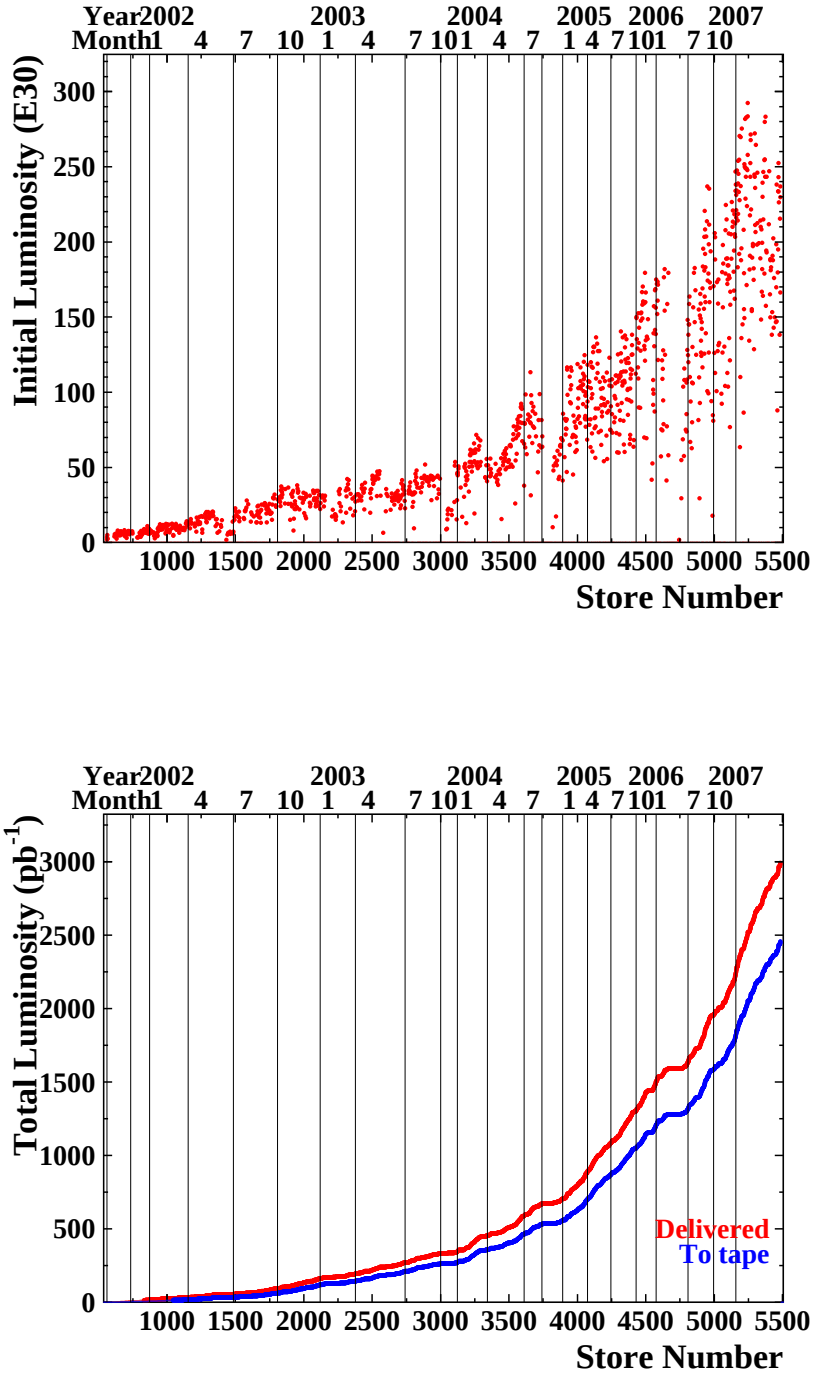

Figure 2.7: Initial instantaneous luminosity per data store (top) and total integrated luminosity in Run II (bottom).

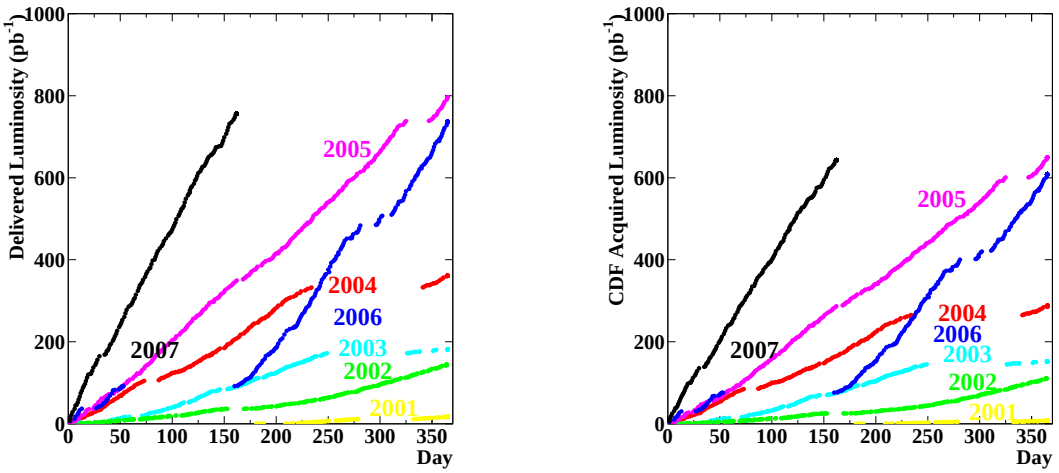

Figure 2.8: Integrated luminosity in Run II delivered by the Tevatron (left) and recorded by CDF (right).

interactions per bunch crossing to a few units. At present day[3] the Tevatron Collider record luminosity has been $\mathcal{L} = 2.92 \cdot 10^{32}$ cm^{-2}s^{-1}, corresponding to about 5 interactions per bunch crossing. The total luminosity delivered by August 2007 in Run II is over 3 fb^{-1}. It is planned to deliver about 6 to 8 fb^{-1} by the end of Run II in autumn 2009. CDF has collected data with about 80% efficiency [16].

[3] Summer 2007.

3. The Run II Collider Detector at Fermilab

3.1 Overview and Coordinate Frame

CDF is a multi-purpose high-energy particle detector with an approximately cylindrical and forward-backward symmetry with respect to the Tevatron beam axis [17], [18]. Its nominal center coincides with the B0 high luminosity interaction region of the Tevatron. CDF comprises a number of coaxial sub-detectors that provide different information:

- a tracking system composed by two silicon microstrip trackers (SVX II and ISL) and an open-cell drift chamber (COT) housed inside a superconducting solenoid providing a 1.4 T magnetic field;
- a time of flight detector backing the COT for particle identification up to momenta of few GeV;
- a set of calorimeters located outside the magnet and used to measure the energy of electrons, photons and hadron jets;
- dedicated detectors used to identify muons that pass through the calorimeters interacting as minimum-ionizing-particles;
- two small angle spectrometers in the very forward and backward regions with respect to the main detector for specialized studies of diffraction processes;
- luminosity monitors.

Two views of the CDF detector composition are shown in Figures 3.1 (isometric cutaway) and 3.2 (projection on a vertical plane containing the beam axis).

A standard Cartesian coordinate frame with orthogonal axes is defined:

- the origin coincides with the geometrical center of the detector;
- the x axis points horizontally out of the Tevatron center;
- the y axis is vertically upward;
- the z axis defined by the proton beam direction.

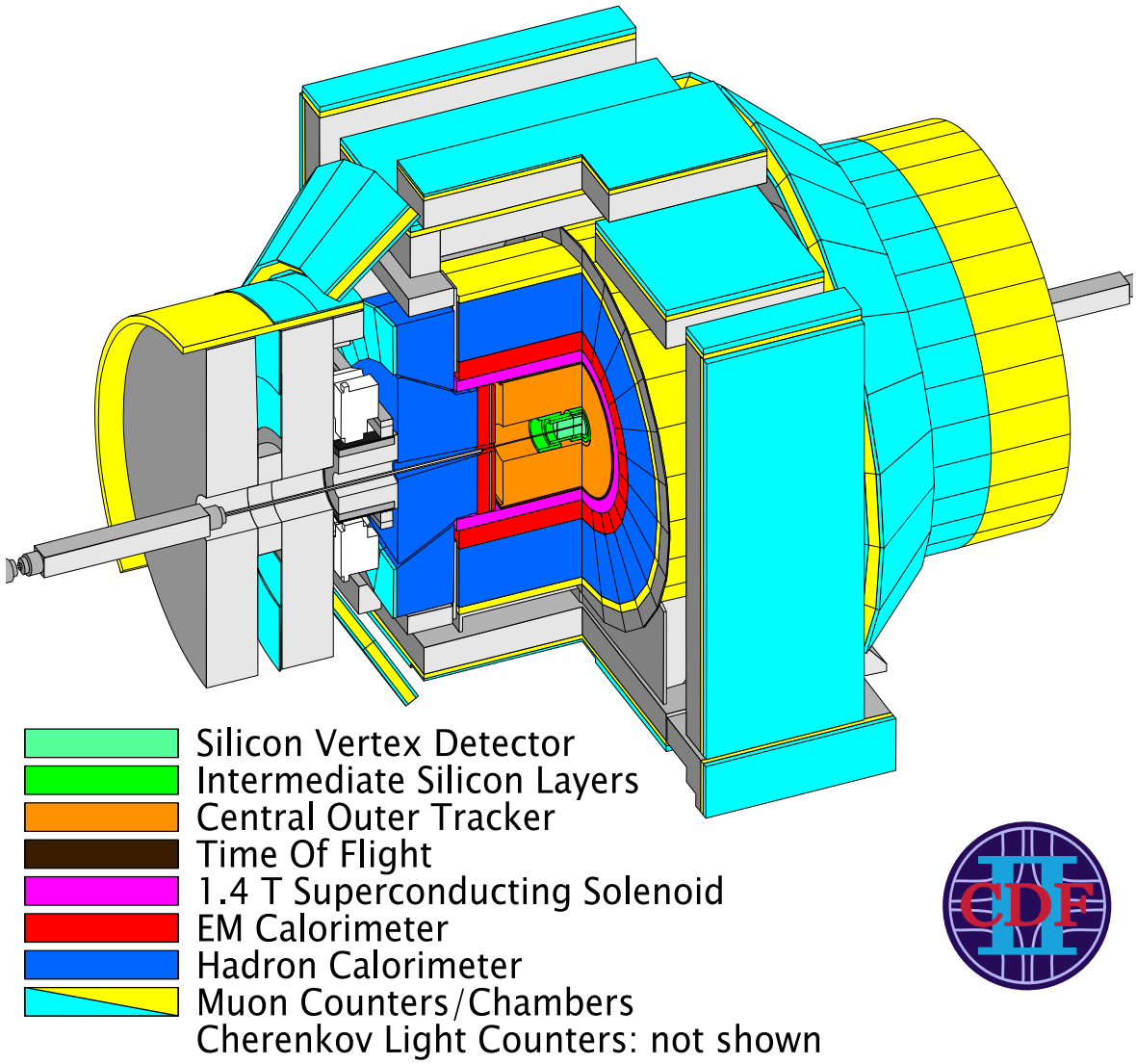

Figure 3.1: Isometric view of the CDF Run II Detector.

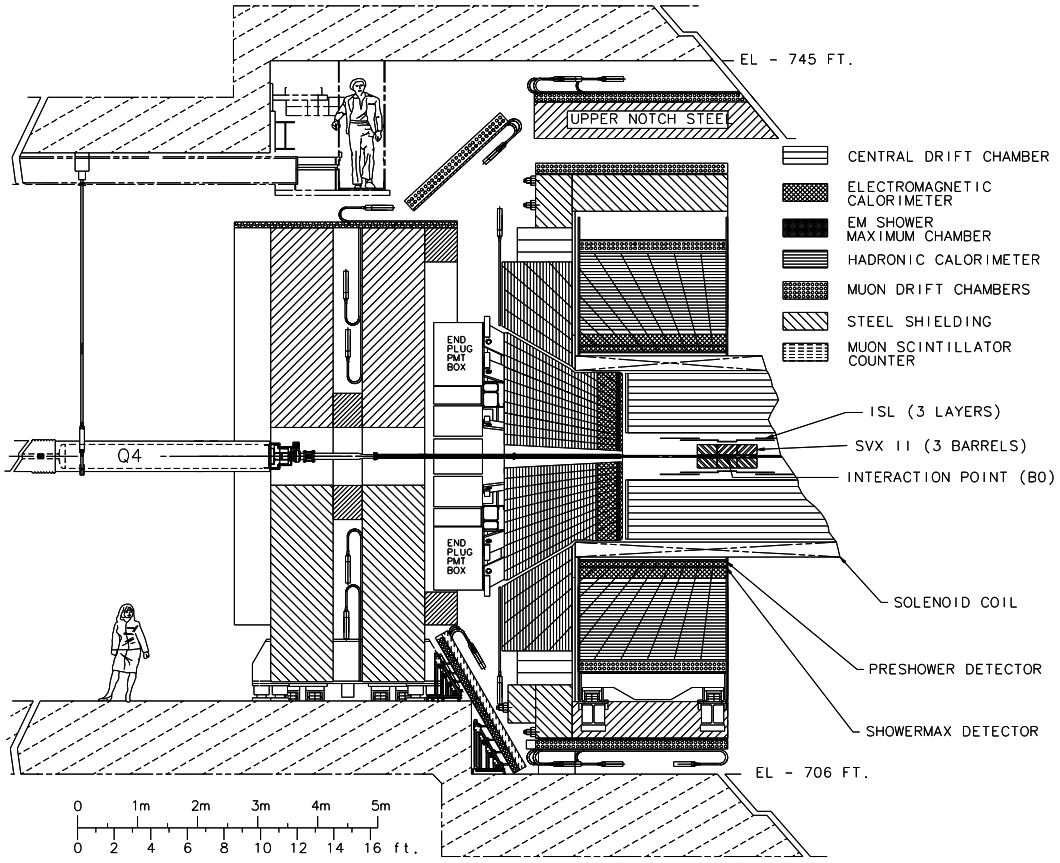

Figure 3.2: Longitudinal view of the CDF RunII detector: TOF is not pictured, Central Muon Extension and forward muon detectors are clearly visible on the left side.

Pseudo-spherical coordinates are more commonly used at CDF, with standard definition of polar angle θ and azimuthal angle ϕ. The polar angle is used to build the pseudrapidity η, defined as $\eta = -\ln(\tan(\theta/2))$. This variable is equivalent to the rapidity $\tilde{y}$ in the limit of massles particles:

$$\lim_{m\to 0} \tilde{y} = \lim_{m\to 0} \frac{1}{2} \cdot \ln \frac{E+p_z}{E-p_z} = \frac{1}{2} \cdot \ln \frac{p+p_z}{p-p_z} = -\ln\left(\tan\left(\frac{\theta}{2}\right)\right) = \eta \ . \tag{3.1}$$

Such a property is useful in view of the nature of hadron collisions: rapidity differences are invariant under boosts on the z axis, therefore the effects of having a moving reference frame for the elementary process (parton collision) are considerably reduced. Many CDF subdetectors are segmented in η with respect to the origin of the coordinate frame ("detector η", or η^{det}). Due to the non-zero length of p and $\bar{p}$ bunches, the effective interaction point can be different from the origin. In such a case the pseudorapidity of the various final state objects is computed with respect to the actual primary vertex of the event ("event η"). In the following chapters η will indicate the "event η" unless differently stated, while for the remaining sections of this chapter it will refer only to the "detector η".

Another fundamental convention used at CDF and which is related to the coordinate frame is the one of cones in the $\eta \times \phi$ space. An euclidean metric is given on the $\eta \times \phi$ space and a cone of radius R centered at $P_0 = (\eta_0, \phi_0)$ is the set of all the points P_i satisfying[1]:

$$\sqrt{(\eta_i - \eta_0)^2 + (\phi_i - \phi_0)^2} \leqslant R \ . \tag{3.2}$$

3.2 Tracking

Tracking and momentum measurement are performed by three subdetectors inside a magnetic field. Two of them (SVX II and ISL) employ silicon microstrips, the third (COT) is an open-cell drift chamber. These three detectors cover different regions in η, as shown in Figure 3.3. The detailed coverage of the silicon trackers is shown in Figure 3.5. The so-called "central region" ($|\eta| < 1$) is the one with the best transverse momentum resolution since a charged particle crosses all COT layers. The other region covered by CDF subdetectors ($1 < |\eta| < 3.6$) is called the "plug region".

• The 1.4 T Superconducting Solenoid

The CDF detector employs a superconducting solenoid for momentum measurements. This solenoid generates a nearly uniform magnetic field of 1.4 T in the tracking region ($|z| < 1.5$ m, $r < 1.4$ m), oriented in the $-z$ direction. The coil has an internal radius of 1.4 m, is 25 cm thick and 4.8 m long. It is made of 1164 Al-stabilized NbTn alloy wire turns carrying a total current of 4650 A. The total amount of material in the coil corresponds to 0.85 radiation lengths for electrons X_0.

[1] The quantity $\sqrt{(\eta_i - \eta_0)^2 + (\phi_i - \phi_0)^2}$ in (3.2) is usually called ΔR_{i0}.

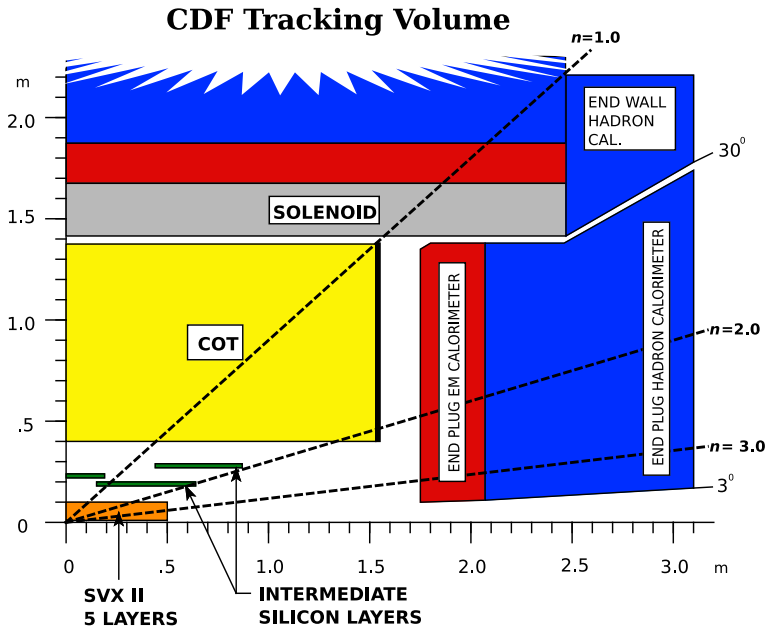

Figure 3.3: Longitudinal view of the CDF II tracking volume.

• Silicon Vertex Detector and Layer 00

The innermost CDF tracker is the Run II Silicon Vertex Tracker (SVX II) [17], [19]. This detector is the evolution of the Run I SVX detector, the first microvertex silicon detector ever used in a hadron collider experiment, whose main purpose was the identification of long-lived hadrons.

The SVX II detector is composed of three 29 cm long barrels carrying 5 layers of double-sided microstrip silicon wafers each. Each barrel is segmented into twelve ($\sim 30^\circ$ wide in ϕ) wedges. The innermost layer (L0) is at 2.45 cm radial distance from the beam axis, while the outermost (L4) is located at 10.6 cm radius. This detector provides both $\mathrm{d}E/\mathrm{d}x$ and position information with a 12 μm resolution on the single hit. The double-side structure of the wafers allows three-dimensional position measurements: one side of the wafer has axial strips (parallel to the beam axis), the other one has either 90° stereo strips (perpendicular to the beam axis) or 1.2° stereo strips (at small angle with respect to the beam axis). The main features of the strip arrangement in SVX II can be found in Table 3.1.

In 2002 the original SVX II was extended with an additional layer (L00) of single-sided microstrip wafers located at about 1.5 cm from the beam axis and supported on the beam pipe [18]. This solution allows L00 to be as close as possible to the interaction point in order to improve the resolution on track impact parameter measurements.

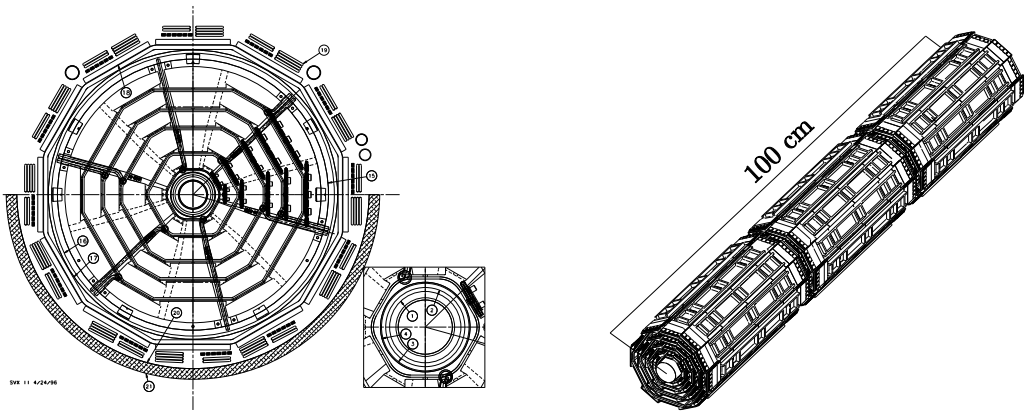

Figure 3.4: Cross section view (left) and isometric view (right) of the SVX II detector.

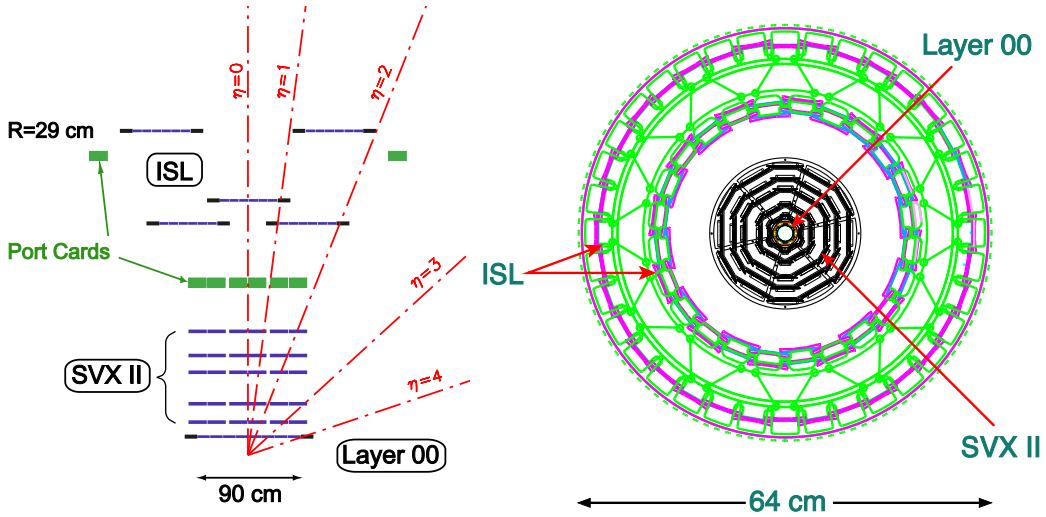

Figure 3.5: Longitudinal coverage of the silicon trackers (left) and cross section view of the integrated SVX II-ISL tracking system (right).

	L0	*L1*	*L2*	*L3*	*L4*
number of stereo strips	256	384	640	768	896
stereo strip pitch (μm)	60	62	60	60	65
stereo angle ($^\circ$)	90	90	$+1.2$	90	-1.2
number of axial strips	256	576	640	512	896
axial strip pitch (μm)	141	125.5	60	141	65

Table 3.1: Parameters of the SVX II layers structure.

• Intermediate Silicon Layers

The Intermediate Silicon Layers (ISL) are an extension of SVX II which provide precision tracking in the forward region ($1 < |\eta| < 2$) [19], [20] and help the matching between SVX II and COT tracks in a dense environment. It consists of double-sided silicon microstrip wafers analogous to those of SVX II, placed at about 20, 22 and 28 cm from the beam axis.

The space resolution of the whole CDF silicon tracker (L00, SVX II and ISL) is about 40 μm in impact parameter and 70 μm in the distance of closest approach to the z axis [21]. The silicon trackers are read by 722432 readout channels. The relative position of the silicon trackers is shown in Figure 3.5.

• Central Outer Tracker

The main tracker at CDF is the Central Outer Tracker (COT), a cylindrical multi-wire open-cell drift chamber [22]. Charged particles in the solenoidal magnetic field perform helical paths whose radius measures their momentum. The internal radius of COT is 44 cm, the external one is 132 cm, the COT total length is 3.1 m. The COT is filled with an Ar-Ethane-CF_4 mixture (in the proportion 50:35:15) that provides fast drift of ionization electrons. The maximum drift time in the COT cells is 100 ns, less than the time interval between bunch crossings (132 ns). The single hit resolution is about 110 μm.

The COT cells are grouped in 8 superlayers (Figure 3.6), 4 with axial wires and 4 with stereo wires, having alternatively a $\pm 3^\circ$ tilt with respect to the z axis. The number of cells per superlayer increases from 168 in SL1 to 480 in SL8. Each cell contains 12 gold-plated tungsten potential wires and 12 sense wires (Figure 3.7). The cells themselves are tilted by 35° respect to the radial direction to allow the Lorentz force to drift ionization in the direction transverse to the radius for optimal momentum resolution. The total amount of material in the COT, including the filling gas mixture, corresponds to 0.017 radiation lengths (X_0) for electrons.

The COT is read by 30240 linear electronic channels and is capable of measuring $\mathrm{d}E/\mathrm{d}x$ besides charged particles momenta.

3.3 Time Of Flight Detector

Between the COT and the solenoid a layer of 1.4 m inner radius of scintillator bars measures the track time of flight (TOF) from the collision point to the solenoid [18], [23]. TOF information can be combined with $\mathrm{d}E/\mathrm{d}x$ to separate pions from kaons up to a momentum of about 1.5 GeV in high precision B-physics measurements[(2)]:

[(2)] In (3.3), T =time of flight, p =particle momentum, L =distance of flight, m =particle mass.

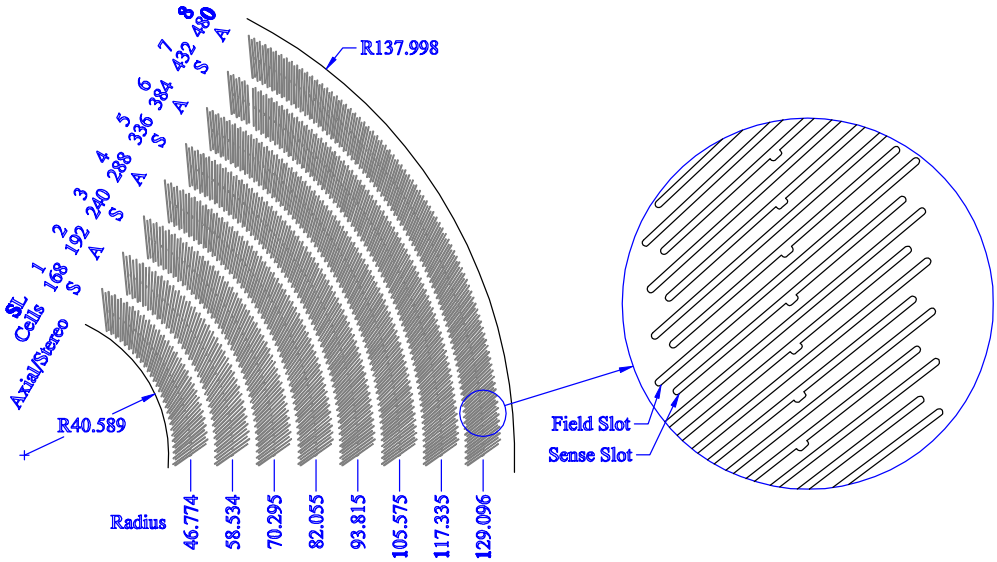

Figure 3.6: Portion of a COT endplate with the 8 superlayer structure for the different cell slots.

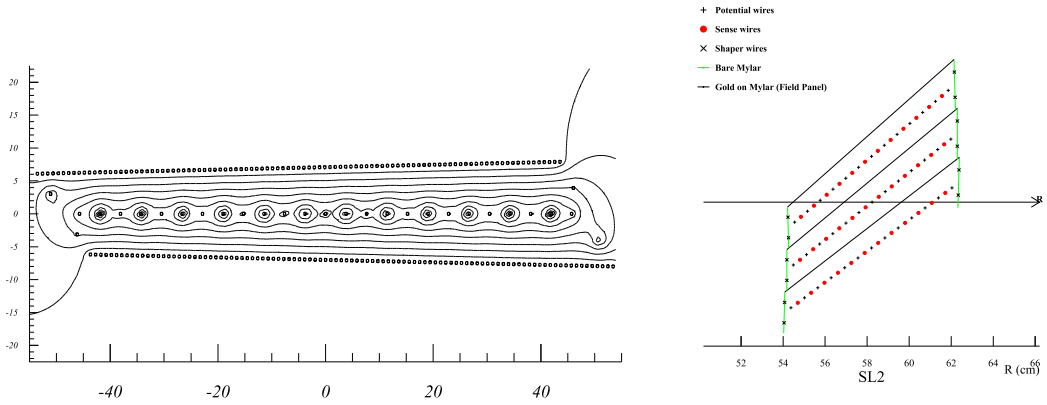

Figure 3.7: Equipotential lines in one COT SL1 cell (left) and wire layout in a COT SL2 portion (right).

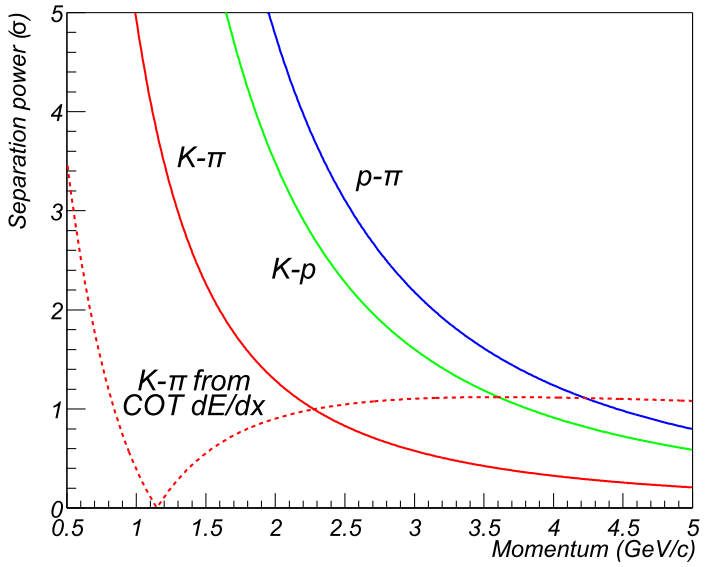

Figure 3.8: Performance of the TOF particle ID (comparison with COT $\mathrm{d}E/\mathrm{d}x$ is shown too).

$$m = \frac{p}{c} \cdot \sqrt{\left(\frac{cT}{L}\right)^2 - 1} \quad . \tag{3.3}$$

The TOF detector is composed by 216 scintillator bars, with a slightly trapezoidal square cross-section of 4 cm basis and a length of 2.79 m. Light is collected by photomultipliers at both ends of each scintillator bar. Single hit position in the TOF is determined by the comparison of the signal times of the photomultipliers. The TOF time resolution is 100 ps. Figure 3.8 shows the CDF pion/kaon/proton separation power by the combined $\mathrm{d}E/\mathrm{d}x$ and TOF measurements.

For the TOF measurement the collision time t_0 must be known. This is found with a ~ 50 ps uncertainty by a best-fit process over all tracks in the event.

3.4 Calorimetry

The energy of final state hadrons is measured with a set of sampling calorimeters [24] which are segmented in projective towers in the $\eta \times \phi$ space and are split into a front electromagnetic and rear hadronic compartment. The CDF calorimeters cover approximatively the entire 4π solid angle up to $|\eta| < 3.6$. However, in between detector sections there are regions ("cracks") where the response is poor.

• Electromagnetic Calorimetry

Electrons and photons are identified and have their energy measured in the EM calorimeter by a set of lead absorbers with fine scintillator sampling. The EM calorimeter is split into three parts: the central EM calorimeter (CEM) covering the region $|\eta| < 1.1$ and the two plug EM calorimeters (PEM) covering the forward regions $1.1 < |\eta| < 3.6$.

CEM

The CEM is composed by two parts joining at $z = 0$, divided into 24 azimuthal wedges subtending $\sim 15^\circ$ in ϕ each. Each wedge is segmented into 10 towers which are projective in polar angle, each subtending 0.1 pseudorapidity units, so that the total number of towers is 480. All towers are read independently on both aides along the ϕ coordinate. The CEM absorber is made of 21 lead layers (3.18 mm thick) alternate to 5 mm polystyrene scintillator layers. The total amount of material in the CEM is $\sim 20 \cdot X_0$. In order to maintain the calorimeter thickness as seen by traversing particles constant in η, some parts of the lead sheets are replaced with plexiglas and the number of absorber layers decreases from 30 at $\eta = 0$ to 20 at the border with the plug region. This arrangement is made in order to ensure the same average energy release by particles independent of their production angle. The blue light produced in the scintillators is collected by wavelength shifters (shifting the light into the frequency region of PMT sensitivity) and sent to photomultipliers on the back of the calorimeters (Figure 3.9). The electron transverse energy[3] resolution of the CEM as measured on a test beam is:

$$\frac{\sigma_{E_T}}{E_T} = \frac{13.5\%}{\sqrt{E_T[\text{GeV}]}} \oplus 2\% \ . \tag{3.4}$$

The CEM comprises two additional specialized detectors: the Central Electron Strip Chambers (CES) and the Central Preshower (CPR) [25]. The CES detector is a set of modules of MWPC, embedded in the EM calorimeter approximatively at the shower maximum depth, which is used to separate EM from hadron showers and to determine the azimuthal position of the showers. The CES modules are between the 8th lead layer and the 9th scintillator layer, where the maximum of the shower is expected to be, at a depth of $\sim 5.9 \cdot X_0$ from the beam axis[4]. Each CES module has 64 axial anode wires, 0.73 cm far from one another and split and read out separately at $|z| = 121$ cm, and 128 cathode strips, whose pitch is 1.67 cm for $|z| < 121$ cm and 2.01 cm for $|z| > 121$. The typical resolution in locating a shower center is about 2 mm. The central CPR is a set of scintillator tiles which helps separating electrons from charged hadrons by tagging their shower early in the shower development, after about $1 \cdot X_0$.

PEM

The PEM calorimeter has a similar structure as the CEM: 22 layers of 4.5 mm thick lead alternate with 22 layers of 4 mm thick scintillator [26]. The PEM tower segmentation is 7.5° in ϕ for

[3] The transverse energy E_T is defined as $E_T = E/\sin\theta$, where E is the energy measured by the tower and θ is the polar angle of the tower.

[4] The amount of material includes the trackers and the solenoid.

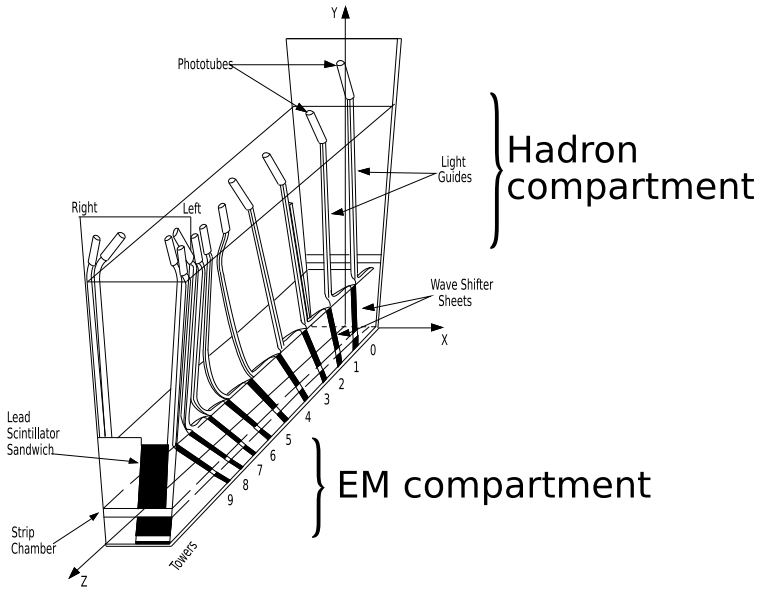

Figure 3.9: Structure of a wedge in the central calorimeters. The front compartment (lower section in figure) is the electromagnetic calorimeter CEM, while the rear one (upper section) is the hadron calorimeter CHA.

$|\eta| < 2.11$ and 15° for $2.11 < |\eta| < 3.6$. The segmentation in η can be understood by an inspection of Figure 3.10. Each scintillator tile is coupled to a different PMT, except for the first layer which is a 1 cm thick plane of scintillator bars read by a multi-anode PMT and acting as a preshower detector. The energy resolution of the PEM is:

$$\frac{\sigma_{E_T}}{E_T} = \frac{16\%}{\sqrt{E_T[\mathrm{GeV}]}} \oplus 1\% \quad . \tag{3.5}$$

Also the PEM is equipped with a shower maximum detector (PES), made of three planes of scintillating strips rotated by 60° and providing a spatial resolution of about 1 mm on the shower location [27].

• Hadronic Calorimetry

The identification of hadrons and the measurement of their energy are performed by a set of calorimeters located behind the EM ones: the central hadronic calorimeter (CHA), covering the region $|\eta| < 0.9$, the two plug hadron calorimeters (PHA) covering the forward regions $1.3 < |\eta| < 3.6$ and two calorimeter rings that cover the gap between CHA and PHA in the region $0.7 < |\eta| < 1.3$, called the wall hadron calorimeters (WHA).

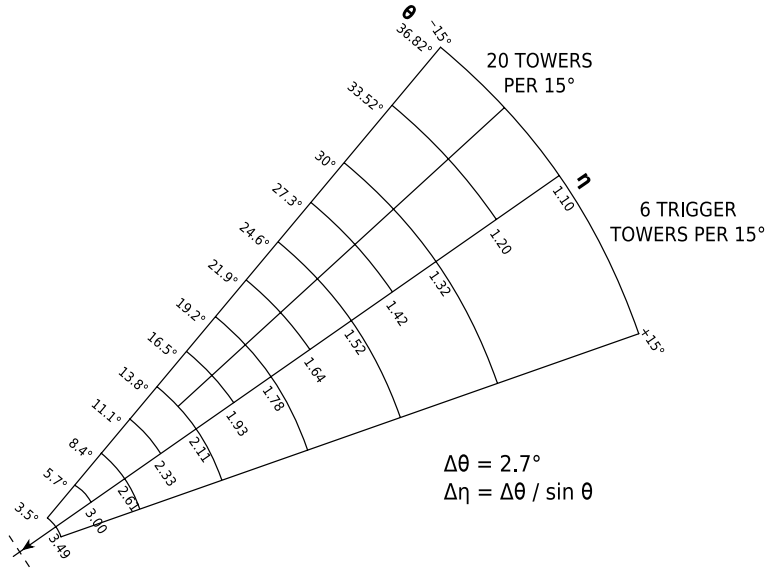

Figure 3.10: Tower segmentation for the PEM and PHA calorimeters.

CHA and WHA

The CHA backs the CEM (Figure 3.9) with the same tower segmentation. The CHA is a sampling calorimeter made of 32 alternate layers of steel (2.5 cm thick) and scintillator (1 cm thick) and it is composed by two parts joining at $z = 0$. The technology of the WHA is the same as of CHA, with a more coarse sampling of 15 layers and thicker converter (5 cm steel, 1 cm scintillator). The number of interaction lengths ($\sim 5 \cdot \lambda$) is approximately constant in the $|\eta| < 1.3$ region. The total number of projective towers of CHA+WHA is 12, 6 entirely contained in the CHA, 3 entirely contained in the WHA and 3 shared between the two. Each tower is read by 2 photomultipliers. The resolutions of CHA and WHA found in test beam measurements (response to single pions) are:

$$\text{CHA: } \frac{\sigma_E}{E} = \frac{50\%}{\sqrt{E[\text{GeV}]}} \oplus 3\% \ , \ \text{WHA: } \frac{\sigma_E}{E} = \frac{75\%}{\sqrt{E[\text{GeV}]}} \oplus 4\% \ . \tag{3.6}$$

PHA

The Plug Hadron calorimeter (PHA) is located behind the PEM [28] and has the same tower segmentation (Figure 3.10). The technology is the same as of CHA, with 23 layers alternating 2 cm thick steel absorber and 6 mm thick scintillator, for a total amount of material corresponding to $7 \cdot \lambda$. Its resolution in single pion test beam was found to be:

$$\frac{\sigma_E}{E} = \frac{80\%}{\sqrt{E[\text{GeV}]}} \oplus 5\% \ . \tag{3.7}$$

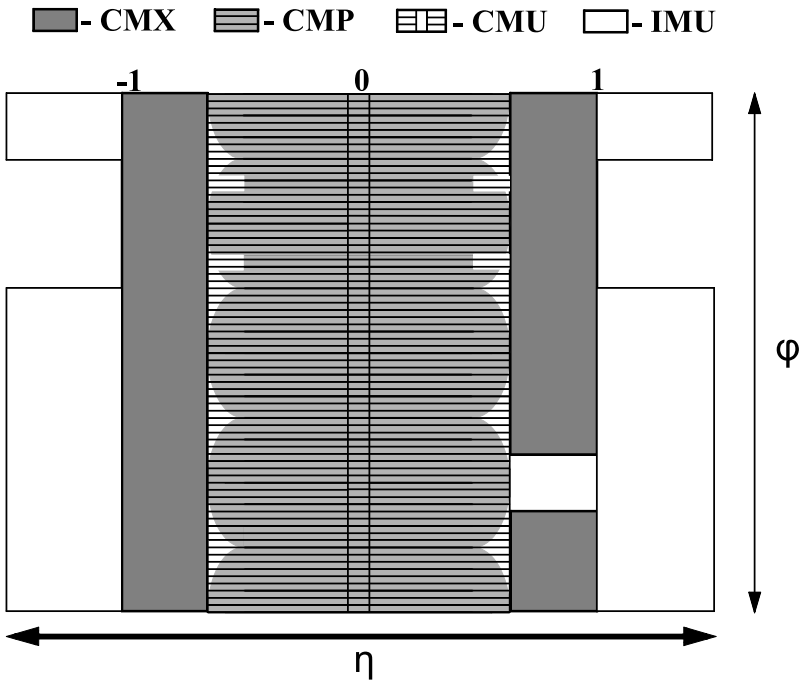

Figure 3.11: Coverage of muon detectors in the $\eta \times \phi$ space.

3.5 Muon Detectors

Muons can be separated from other particles because their typical radiation length is $\sim 4 \cdot 10^4$ times greater than for electrons. This means that muons can pass through a thickness of dense materials large enough to absorbe most hadrons, while interacting as a MIP. To exploit the penetration power of muons, the CDF calorimeters are surrounded by muon detectors which signal crossing charged particles which were not absorbed in the calorimeters (Figure 3.1) [29].

CMU and CMP

The muon detectors are grouped into different sets according to the region they cover (Figure 3.11). The Central Muon detectors (CMU) are a set of 144 drift chamber modules of 16 cells each. These cells are 266 cm $\times$ 2.68 cm $\times$ 6.35 cm wide with a single 50 μm steel wire at their center (Figure 3.12). Scintillation counters are sandwiched to the chamber to help finding the ϕ and z position of the hit and matching the muon to a COT track. The maximum drift time for CMU is 800 ns.

In the $|\eta| < 0.65$ region an additional set of muon chambers, the Central Muon Upgrade detectors (CMP), surrounds the CMU detectors in the $|\eta| < 0.65$ region behind a 60 cm thick

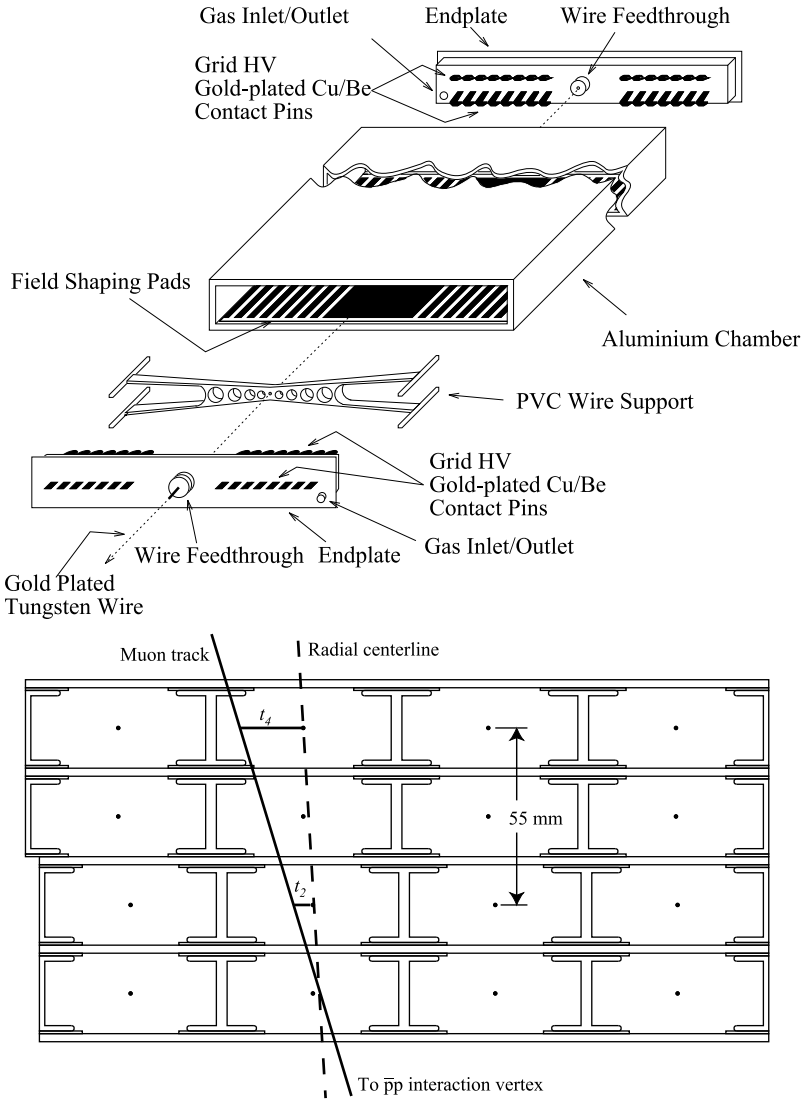

Figure 3.12: Exploded view of CMP/CMX/IMU tubes (top) and cross section of CMU layers (bottom).

steel absorber. As the CMU, the CMP are rectangular chambers stacked in four layers (Figure 3.12), typically 640 cm $\times$ 15 cm $\times$ 2.5 cm in size. The first and fourth layer have different cell width in order to remove left-right ambiguities in position finding and help in triggering on muons. CMP chambers are sandwiched to scintillator layers (CSP) on the outermost side, for the identification of the bunch crossing. Scintillators are colored in light blue in Figure 3.1, while drift chambers are yellow. The maximum drift time in CMP is 1.4 μs.

CMX

A set of muon detectors arranged in a truncated conical shape around the plug calorimeters, the Central Muon Extension (CMX), provides muon identification in the $0.65 < |\eta| < 1$ region. Their structure is analogous to the CMP, with a different cell length (180 cm) and scintillators on both sides (CSX).

IMU

The CDF detector is shielded in the forward regions by two pairs of steel toroids (Figure 3.1), around which the Intermediate Muon detectors (IMU) are laid. These are scintillation counter/drift chamber sandwiches similar to CSP/CMP and CSX/CMX, arranged in azimuthal rings [(5)] to cover the $1 < |\eta| < 1.5$ region. The IMU tubes (Barrel Muon Chambers - BMU) are 8.4 cm wide and 363 cm long and are coupled to scintillators (BSU). There is a scintillator layer between the two toroids of each pair (TSU), laying on the transverse plane and covering the $1.3 < |\eta| < 2$ region.

3.6 Čerenkov Luminosity Counters

The Tevatron collider Run II design luminosity ($\sim 2 \cdot 10^{32}$ cm^{-2}s^{-1}) and time spacing between bunch crossings (132 ns) require a suitably designed subdetector for precision luminosity measurement [30]. The Čerenkov Luminosity Counter (CLC, Figure 3.13) is composed of two identical modules housed inside the plug calorimeters and sorrounding the beam pipe ($3.7 < |\eta| < 4.7$). The CLC measure the rate of inelastic processes of known cross section in the forward region. Each of the two modules is composed by 48 conical gaseous Čerenkov counters pointing to the origin of the coordinate frame. The cone size is variable from the 110 cm long innermost layer to the 180 cm long outermost layer.

The Čerenkov light is collected by conical mirrors at the rear end of the cones and detected by high gain ($\sim 2 \cdot 10^6$) photomultipliers. The Čerenkov light radiator is Isobuthane at a pressure which can be varied between 1 and 2 atm, according to the desired yield. In this conditions the Isobuthane refraction index is relatively high ($n = 1.0043$) and the gas is transparent to UV radiation. Particles originated at small angles from $p\bar{p}$ collisions can travel through a large portion of the CLC cones and produce a measurable amount of Čerenkov photons, while stray particles

[(5)] The barrels are not complete: they surround the toroids for 3/4 of their circumference, in the lower part they meet the floor, as in Figure 3.11.

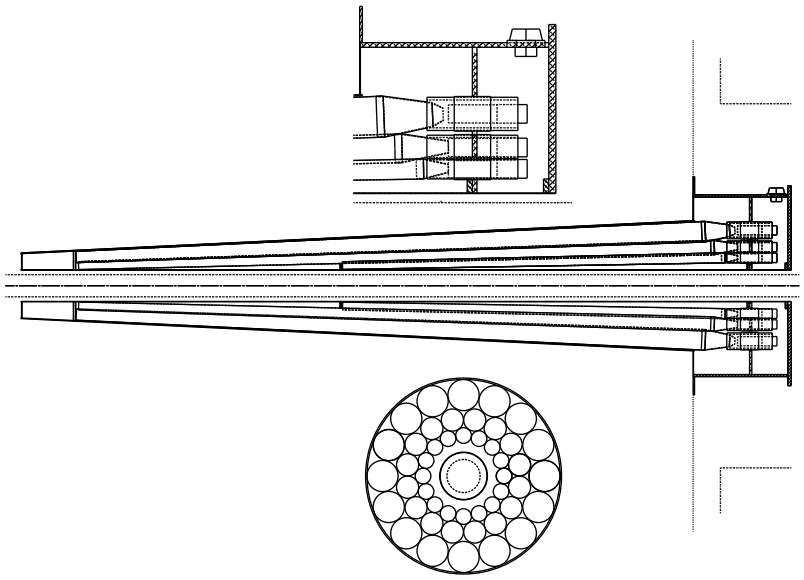

Figure 3.13: Structure of the CDF Čerenkov luminosity monitors.

from the beam halo do not. Beam-beam events, whose rate measures the luminosity, are selected by setting a lower threshold on light yields. The CLC time resolution is < 100 ps and beam-beam events can be selected with a left-right coincidence between the two modules. The luminosity can then be determined from the bunch crossing frequency f, the $p\bar{p}$ inelastic cross section σ_I, the CLC acceptance ε, the average number of hits per bunch crossing $\langle N \rangle$ and the average number of hits per inteaction $\langle N_1 \rangle$:

$$\mathcal{L} = \frac{f}{\sigma_I \cdot \varepsilon} \cdot \frac{\langle N \rangle}{\langle N_1 \rangle} \ . \tag{3.8}$$

The value used in (3.8) for σ_I is derived from the one obtained by combining the CDF Run I measurement of forward diffractive cross section and the E811 measurement of elastic scattering and total cross section at $\sqrt{s} = 1.8$ TeV. The obtained values were extrapolated to the present Tevatron c.m.s. energy $\sqrt{s} = 1.96$ TeV:

$$\sigma_I(1.8 \text{ TeV}) = 60.4 \pm 2.3 \text{ mb} \longrightarrow \sigma_I(1.96 \text{ TeV}) = 61.7 \pm 2.4 \text{ mb} \ . \tag{3.9}$$

The resolution on $\mathcal{L}$ is limited to 5.9% by systematic uncertanties due to detector stability (1.8%), CLC acceptance (4.0%) and σ_I (3.8%).

3.7 Forward Detectors

A set of forward detectors, not shown in Figures 3.1 and 3.2, are used for the measurement of diffractive processes at small angle [31]. Their location is outside the CDF calorimeters, at

Step	rate
L1 Accept	$\sim$ 25 kHz
L2 Accept	$\sim$ 750 Hz
Event Builder	75 MB/s
L3 Accept	$\sim$ 85 Hz
Storage Rate	20 MB/s

Table 3.2: Rate of accepted events for each step of the Trigger and DAQ system.

different distances up to 57 m from the origin of the interaction region. The diffractive event detector comprises the:

- Miniplug Calorimeter (MNP): a Pb/liquid scintillator sampling calorimeter in the $3.6 < |\eta| < 5.2$ region;
- Beam Shower Counters (BSC): a set of scintillation counters on the two sides of the main CDF enclosing the beampipe;
- Roman Pot Spectrometers (RPS): a set of 3 "Roman Pots" housing miniaturized scintillator hodoscopes building two diffractive proton spectrometers on the two sides of CDF.

3.8 Data Aquisition and Trigger

The time spacing between bunches implies a bunch-bunch crossing rate of about 7.6 MHz, much higher than the event writing rate which is of the order of 100 Hz. Of course, only a small fraction of bunch crossings produce interesting events. Even so, the problem of collecting most of them is a very serious one. Only a tiny fraction of the interactions are physically interesting and are hidden in a huge amount of elastic, inelastic and diffractive $p\bar{p}$ interactions. The total $p\bar{p}$ cross section for such processes is $\sim$ 100 mb, while the cross sections of interest at CDF are many orders of magnitude smaller. Examples are the $b\bar{b}$ production cross section which is ~ 0.1 mb and the $t\bar{t}$ production cross section which is $\sim 7-9$ pb. The trigger must be very selective and reject most of uninteresting events. Once this is done, the event rate that one would like to collect is still much larger than what can be done in practice and a hard selection must be made by which only the events of the greatest interest are eventually collected at a rate that would not compromise the live time of the electronics.

This online event selection is performed with a three-level structured trigger, whose architecture is shown in Figure 3.14. The trigger levels perform increasingly tighter selections reducing the data flow to the next level to an acceptable level for the more elaborate and time-consuming filtering to be performed. The rates of accepted events at each level are shown in Table 3.2.

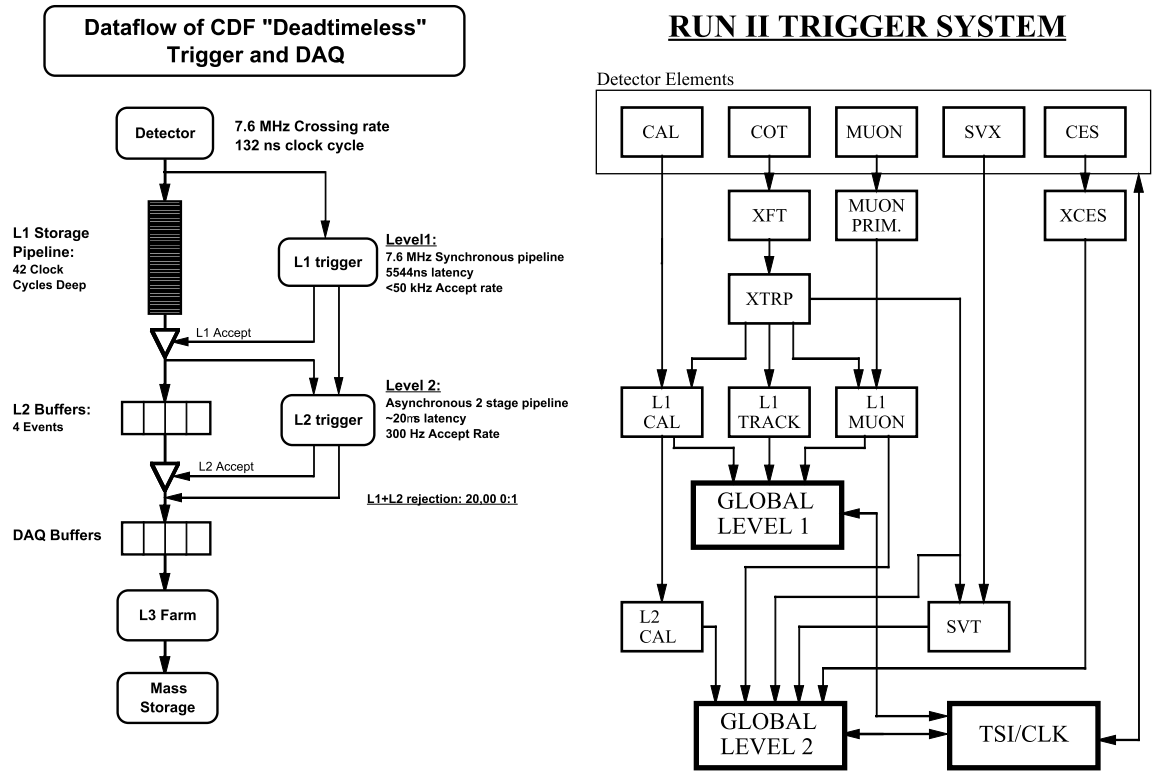

Figure 3.14: Data flow in the CDF trigger (left) and structure of the L1 and L2 triggers (right).

• Level 1

The level 1 (L1) trigger stores the events in a synchronous 42-stages pipeline through which events are shifted for 5.7 μs at the same rate as bunch crossings. Three parallel streams are read: one for calorimeter information, one for muon detectors information and one for COT information. The total amount of different triggers that can be obtained by performing simple logical operations on the events is 64. The Extremely Fast Tracker (XFT) finds tracks with $p_T \gtrsim$ 1.5 GeV using only the axial COT superlayers: first the Finder Board searches the 4 axial SL for track segments, then the Linker Board tries to link together at least 3 of them. The maximum time required to check if the event satisfies one of the L1 trigger conditions is 5.5 μs in order to cause no dead time. For each event, all the information from the CDF subdetectors are stored in the pipeline. In order to operate at the required speed, the L1 involves only hardware. After 42 bunch crossings the L1 decision is taken and, if an event is accepted, its information is stored in a L2 local buffer.

• Level 2

The L2 event selection is based on the parameters of reconstructed physical objects, like hadron jets, electrons and muons. When an event is considered good its physical objects are read by the Event Builder (EVB), where the entire event is merged [32]. At level 2 one may suffer some dead time, because if an event is being analyzed, the corresponding L2 buffer is not available to receive data from L1. The block diagram of the various L1 and L2 interconnections and involved subdetectors are schematized in Figure 3.14.

• Level 3

Once the event is assembled by the EVB it is sent to the L3 farm. This is a parallel processors farm that reconstructs the entire event to the same accuracy as in the offline analysis. Accepted events are split in streams of particular physical interest and are stored on tape at $\sim$ 100 Hz rate.

4. Identification and Definition of Objects

The raw outputs of several CDF subdetectors must be combined in order to reconstruct the physical objects such as electrons, muons or hadron jets, that are of interest in the analysis of the entire event. Refinements of object reconstruction are possible and some of them are explained in Chapter 5. The requirements on the physical objects used in the analysis (the so-called "event selection") are described in Chapter 6.

4.1 Tracks

Charged particle trajectories are reconstructed from COT, SVX II, L00 and ISL information [34]. The different kind of information available from these detectors are listed in the respective sections of Chapter 3. All CDF tracking detectors are immersed in a 1.4 T solenoidal magnetic field aligned along the antiproton beam direction. Charged particles crossing the tracking volume perform a trajectory that can be described by a helix. The relevant parameters of the reconstructed helix are:

- the curvature $C = 1/(2 \cdot r)$, where r is the curvature radius in the transverse plane; the curvature is positive if the track is clockwise in the $x \times y$ plane and negative in the opposite case. By measuring C and the charge q one gets the transverse momentum of the track:

$$p_T = \frac{B \cdot q}{2 \cdot C} \ ; \tag{4.1}$$

- the impact parameter d_0, which is the minimum distance (corresponding to the "track vertex" location) between the track trajectory and the z axis; d_0 has opposite sign to the angular momentum of the track relative to the z axis[(1)]:

$$|d_0| = \sqrt{x_0^2 + y_0^2} - r \ ; \tag{4.2}$$

- the z coordinate of the track vertex (z_0);
- the cotangent of the polar angle θ_0 that the track makes with the z axis;
- the azimuthal angle ϕ_0 of the track at its vertex.

[(1)] In (4.2), x_0 and y_0 are the coordinates of the center of the circle which is the projection of the helix on the transverse plane.

• COT Tracking

Track pattern recognition in the COT is performed in four steps. The first step is the segment finding: each of the 8 COT superlayers is searched for groups of three aligned hits, which are fitted to a straight line with the method of the least squares. All hits closer than 1 mm to the fitted 3-hits seed line (1 mm road) are attached to the line and the fit is repeated.

Tracks are reconstructed from the information of the axial superlayers only, with either one of two different algorithms. One algorithm ("segment linking") links segments in different superlayers and fits them to a circle with the minimum χ^2 method. The other one ("histogram linking", [35]) starts with a default circle defined by one COT segment and the beam axis, fills a 200 μm binned histogram with the distance from the center of the circle of all hits in 1 cm wide road. If the most populated bin contains at least 10 hits, those hits are added to the track. The "histogram linking" algorithm ends with the attempt of adding more hits in a 750 μm road around the track and refitting it. If a track is reconstructed by both algorithms, duplicates are removed.

The third step in COT track reconstruction is the addition of stereo hits. For each axial track, a "segment linking" algorithm tries to attach stereo hits from the outer superlayer, refits the track and then tries to add hits from inner superlayers. The second phase of stereo reconstruction is "histogram linking"-based and is used to find the vertex of the track. The fourth and last step of COT tracking is a global refit of the track taking into account all known corrections for the non-uniformity of the magnetic field and for the modeling of the electron drift.

• Standalone Tracking

The Standalone Tracking Algorithm (called this way because it does not need any prior information as input) reconstructs tracks in the silicon detectors [36]. The Standalone Tracking groups aligned three-dimensional silicon hits into triplets. The first step of the algorithm is the building of 3D hits from each possible pair of axial and stereo hits in the SVX II layers. Next, all hits in the inner and outer layers are explored as extremes of a candidate track. Hits close to the candidate track are searched for in the intermediate layers to build hit triplets. If more than one hit can be matched to a candidate track, the track is cloned and each new hit is matched to a clone track. A full fit on the hits with a helix is performed and only one track for each clone group is selected.

• Outside-In Tracking

The Outside-In Tracking in the silicon detectors requires a COT track as input [37]. Starting from the outermost layer, the silicon hits are iteratively attached to the track, starting with axial layers and attaching the hits on the stereo layers in a second iteration. If more than one attachable hit is found, an iterative fit with a heilx is performed until only one track is accepted. The accepted track has the largest number of hits. If this criterion is satisfied by more than one track, the one with the lowest χ^2 is selected.

• "Phoenix" Forward Electron Tracking

The Phoenix tracking algorithm [38] combines calorimetric information and standalone silicon tracks to track electrons in the forward region. The position of the EM shower in PES and the primary event vertex are used as seed points of the track helix and the helix curvature is varied to match the calorimeter E_T. If such a match is found, the track is called Phoenix electron (PHX).

• Event Vertex Finding Algorithm

The position of the effective interaction point, the so-called "primary vertex" of the event, is reconstructed by two algorithms: `PrimVtx` and `ZVertex`.

The seed vertex used by `PrimVtx` is the average event z position measured during collisions. All tracks with $|z_{trk} - z_{vtx}| < 1$ cm, $|d_0| < 1$ cm and $|d_0/\sigma_{d_0}| < 3$ are selected, ordered in decreasing p_T and fitted to a common vertex. The tracks with $\chi^2 > 10$ after the fit are removed and the procedure is iterated until all accepted tracks have $\chi^2 < 10$.

`ZVertex` selects vertices from tracks passing minimal quality requirements and removes those without a minimal associated number of tracks with $p_T > 300$ MeV[(2)]. The z position of each vertex is the mean z_0 of its associated tracks, weighted on the respective σ_{z_0}.

4.2 Electrons and Photons

Electrons[(3)] and photons are identified from their showers in the EM calorimeters, which are usually entirely contained into them. The discrimination between electrons and photons is obtained by requiring a reconstructed track pointing to the energy cluster in the EM calorimeter for the electrons and no tracks for photons. The discrimination power from hadrons, which are in general not-fully contained in the EM calorimeter, is enhanced by the different shower shape detected with the shower maximum detectors and the preshower detectors. Given a cone with radius $R = 0.4$, as wide as the typical hadron jets, centered on the EM cluster[(4)], the "no track" requirement for photons consists of:

- the difference between the EM signal E_{EM} and the sum $\sum_i E_i$ over all calorimeter towers within the cone must be less than $0.15 \cdot E_{EM}$;
- the sum $\sum_j p_{T_j}$ over all tracks within the cone must be less than 2 GeV.

Photons can be faked by electrons when their track fails to be reconstructed. Electrons can be faked by charged hadrons showering in the EM calorimeters or in the solenoid or by converting photons ($\gamma\gamma^* \to e^+e^-$, being γ^* an atomic or molecular field) when a track happens to point to

(2) A track is associated to a vertex if its distance from the vertex is less than 1 cm (silicon vertex) or 5 cm (COT vertex).
(3) In this work "electron" stands for both e^+ and e^-.
(4) See Section 3.1 and (3.2).

the photon EM cluster. Electrons from photon conversion are identified if two opposite-sign COT tracks are close in space showing $|\Delta(\cot\theta_0)| < 0.04$ and $|\Delta(xy)|$[5] < 2 mm.

4.3 Muons

Muons do not shower in the calorimeters because their radiation length is ~ 40000 times smaller than the electron one and because they are not subject to strong interactions: therefore they behave as MIPs when interacting with the calorimeters. A muon is therefore defined as a COT track pointing to a muon "stub" (a track segment reconstructed in the four-layered muon chambers – see Figure 3.12). Muons can be faked by hadrons showering deep in the calorimeters or not showering at all and by cosmic muons. Cosmic muons crossing the COT may look like an opposite sign muon pair. They can be rejected by imposing tight requirements on their distance from the beam line and by exploiting the timing information given by hits in TOF counters.

4.4 Hadron Jets

Quarks and gluons suffering a large momentum transfer interaction manifest themselves as hadron jets. The strong potential binding quarks and gluons within nucleons can be roughly parametrized as a function of the inter-parton distance as

$$V(r) = -\frac{a}{r} + b \cdot r \ , \tag{4.3}$$

with positive a and b. When the inter-parton distance increases, hadron jets are generated because the production of new partons (eventually hadrons) is energetically less consuming than stretching the parton bound (4.3) further[6]. Therefore jets are the observable objects to be associated to the final state partons in a large momentum transfer interaction. Because of the intrigued multi-step relationship relating jets to primary partons one must be careful in their treatment and definition since any inappropriate handling would limit the sensitivity to new discoveries. For example, a poor jet energy resolution would reduce the sensitivity in the search for a SM light Higgs Boson $H \to b\bar{b}$. A wrong jet energy scale can introduce a bias in delicate measurements, like in measuring the top quark mass.

A hadron jet has its properties measured primarily by calorimeters[7]. The information it carries can be degraded on three levels, for non-accounted physical reasons and for instrumental features of the detectors (Figure 4.1):

1. the quark or the gluon from which the jet is generated corresponds to the "parton level": whether the jet is generated by a quark or by a gluon is not known and their parton emission in the slowing-down process is different;

[5] $\Delta(xy)$ is the distance between the two tracks on the $x \times y$ plane.
[6] This phenomenon is called "hadronization" or "fragmentation".
[7] The ripartition of jet energy is typically $\sim 60\%$ in EM calorimeters and $\sim 40\%$ in hadron ones.

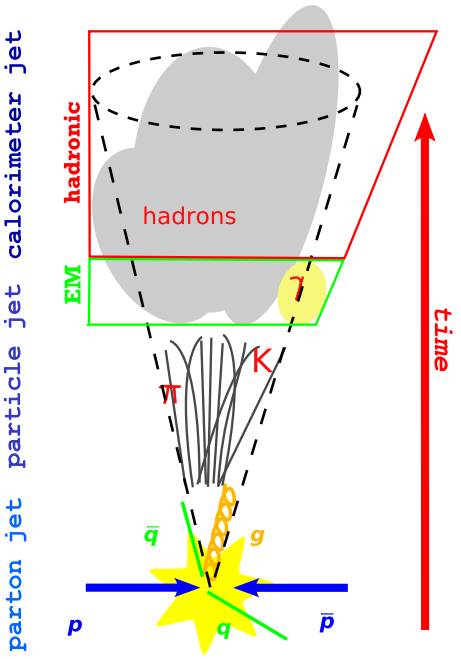

Figure 4.1: The three levels through which the initial state partons are thought to evolve into a final state hadron jet.

2. the particles produced in the evolution of the jet correspond to the "particle (or hadron) level": the details of particle production the fragmentation process are unknown;

3. the signal pulses of the calorimeters employed to identify the jet correspond to the "calorimeter level": the calorimeter response to hadrons is only approximately known and the calorimeter signals are subject to measurement errors.

A universally valid way of defining a jet does not exist because there is no control on how the hadronization process takes place: the experimentalist's task is to concieve an algorithm that allows the extrapolation of the parton properties from the calorimeter jet ones. In this section the first step of this backwards path from calorimeter level to the parton level, the jet reconstruction, is described as it is performed at CDF [39], [40]. Other steps, related to jet corrections, are described in Sections 5.1 and 7.2.

The reconstruction algorithm, also called clustering algorithm, tries to label a set of energy depositions in the calorimeters as "jets". It can be implemented in different ways, according to physical considerations and practical convenience. However, any reconstruction algorithm must satisfy some requirements which are independent on the actual implementation. These ideal attributes of a clustering algorithm are [39]:

- correct treatment of jet properties by a conceptual point of view ("theoretical attributes")

1. it should not be "infrared sensitive", which means that jets originating from different partons should not be merged because of soft radiation in the region between them (Figure 4.2, left);
2. it should not have any "collinear sensitivity", which means that jet identification and energy should not depend on how jet prongs are distributed on the calorimeter cells (Figure 4.2, center and right);
3. the reconstructed transverse energy should not be sensitive to longitudinal Lorentz boosts;
4. the algorithm should give the same results if applied at any of the three levels of jet evolution;
5. it should be implemented in a computational environment with reasonable easiness;

- application flexibility to experimental conditions ("experimental attributes")

1. it should be able to reconstruct jets in detectors of different design;
2. it should not degrade the instrumental resolution;
3. its performances should be stable against multiple interactions in the same bunch crossing;
4. it should be optimized in terms of computing time;
5. it should identify all interesting jets;
6. it should allow an easy calibration of the jet properties;
7. it should applicable in a wide range of jet multiplicity, space distribution and energy;
8. it should be easily applicable.

• Jet Reconstruction by Cone Algorithm

Cone algorithms group together all calorimeter towers whose center (or, at particle level, all particles whose trajectories) fall within a cone of given radius in the $\eta \times \phi$ space (Section 3.1). The official jet algorithm at CDF is a cone algorithm called `JetClu`:

1. each calorimeter tower is identified by a vector in the $r \times \eta \times \phi$ space, that joins the origin of the coordinate frame with the center of the calorimetric tower[(8)], whose E is the magnitude of the vector;
2. all towers with $E_T = E^{EM} \cdot \sin\theta^{EM} + E^H \cdot \sin\theta^H > 1$ GeV are marked as precluster seeds and ordered in decreasing E_T;

[(8)] The center of a tower is identified by the geometrical η and ϕ center of the tower and at a $6 \cdot X_0$ for the EM calorimeters or $1.5 \cdot \lambda$ for the hadron ones: θ^{EM} (θ^H) is the polar angle of the vector pointing to the geometrical center of the EM (hadron) compartment of the calorimeter tower.

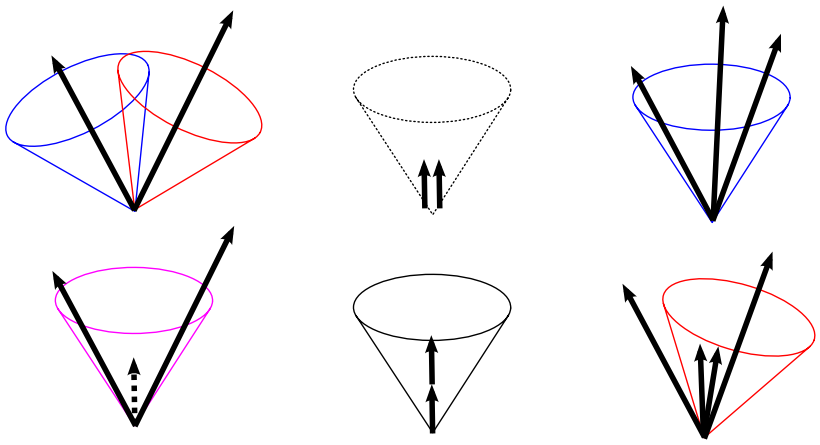

Figure 4.2: Schematic representation of the "sensitivities" of a clustering algorithm: "infrared sensitivity", when two jets from different primary partons are merged because of some intermediate soft radiation (left); "collinear sensitivities", when one jet is below or above the acceptance threshold depending on the energy distribution in the calorimeters (center) or when the properties of the final jet are largely different because of a slightly different energy distribution in the prongs (right).

3. the seeds contained in a 49-towers square centered on the highest E_T seed are grouped into a precluster (Figure 4.3), the centroid of the precluster is evaluated by mediating over all precluster towers weighting each tower with its E_T;

4. a cone of fixed radius[(9)] is drawn centered on the precluster centroid and all vectors with $E_T > 0.1$ GeV falling inside the cone are added to the precluster and its centroid is recalculated:
$$\eta_{PC} = \frac{\sum_{i \in PC} \eta_i \cdot E_{T_i}}{\sum_{i \in PC} E_{T_i}} \quad , \quad \phi_{PC} = \frac{\sum_{i \in PC} \phi_i \cdot E_{T_i}}{\sum_{i \in PC} E_{T_i}} \quad ; \tag{4.4}$$

5. this procedure is iterated until the list of the towers included in the cluster does not change any more;

6. these stable candidate jets can overlap and must be merged or split according to the amount of the shared E_T:

   - if the shared E_T is greater than 75% of the less energetic jet E_T, the two jets are merged and the centroid of the jet is recalculated;
   - if not, the shared towers are assigned to the closest jet in the $\eta \times \phi$ space.

[(9)] At CDF the standard cone radii are 0.4, 0.7, 1.0: the choice depends on the jet multiplicity of the events (usually the smallest R is chosen for events with many jets) and on the features of the analysis.

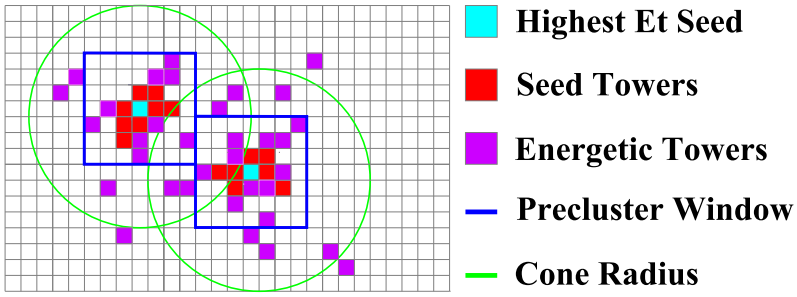

Figure 4.3: Jet reconstruction by the `JetClu` cone algorithm.

Once the jet is identified, the information coming from all related towers must be combined to obtain the jet parameters according to a recombination scheme. Two recombination schemes have been used at CDF: the "Snowmass scheme", whose definition of the jet vector is extracted by (4.4), and the "E-scheme", which is used in current analyses:

$$E_J = \sum_{i\in J}\left(E_i^{EM}+E_i^H\right) \quad , \tag{4.5}$$

$$p_{x_J} = \sum_{i\in J}\left(E_i^{EM}\cdot\sin\theta_i^{EM}+E_i^H\cdot\sin\theta_i^H\right)\cdot\cos\phi_i \quad , \tag{4.6}$$

$$p_{y_J} = \sum_{i\in J}\left(E_i^{EM}\cdot\sin\theta_i^{EM}+E_i^H\cdot\sin\theta_i^H\right)\cdot\sin\phi_i \quad , \tag{4.7}$$

$$p_{z_J} = \sum_{i\in J}\left(E_i^{EM}\cdot\cos\theta_i^{EM}+E_i^H\cdot\cos\theta_i^H\right) \quad . \tag{4.8}$$

Towers and jets are treated as massless particles[(10)] and from their total four-momentum all relevant quantities for the analysis are computed:

$$p_{T_J} = \sqrt{p_{x_J}^2+p_{y_J}^2} \quad , \tag{4.9}$$

$$E_{T_J} = E_J\cdot\frac{p_{T_J}}{p_J} \quad , \tag{4.10}$$

$$\eta_J = \frac{1}{2}\cdot\ln\frac{E_J+p_{z_J}}{E_J-p_{z_J}} \quad . \tag{4.11}$$

The use of seeds in `JetClu` is a source of infrared and collinear sensitivities which may be avoided by the use of other algorithms that are currently under study and are briefly summarized in Appendix A.

[(10)] This is why η_J is calculated as $\tilde{y}_J$.

4.5 Neutrinos (Missing E_T)

Neutrinos do not leave any sign of their passage in the detector and their presence can be inferred only by momentum conservation. Since the p_z of the reference frame of the elementary parton collision is unknown and many particles are produced in the very forward region escaping down the beam pipe, only transverse momentum can be used to look for neutrinos. If the total transverse momentum measured by the calorimeters (as a vector) is significantly different from zero, its negative can be attributed to the presence of neutrinos among the final state particles produced in the event and is called "missing E_T" ($\not{E}_T$ or MET)[11]:

$$\not{\mathbf{E}}_T = -\sum_i E_i \cdot \sin\theta_i \cdot \hat{n}_i \ . \tag{4.12}$$

[11] $\not{E}_T$ can be computed this way because neutrinos can be considered massless; $\hat{n}$ is the unit vector identifying the position of the tower in the transverse plane and the index i runs on all calorimeter towers.

5. Auxiliary Tools

The reconstruction of the event as described in Chapter 4 does not take into account the specific performances of the various CDF subdetectors, which may depend on time (stability and aging of materials) or on the peculiarities of the single components. The reconstruction does not take into account also some information that may be needed in specific case. Some of the auxiliary tools employed in offline event reconstruction and useful for the presented work are described in this chapter. These tools are of general interest in CDF and are provided in a flexible form so that they can be adapted to any physics analysis.

5.1 Corrections to the Raw Measured Jet Energy

As discussed in Section 4.4, the information obtained by jet reconstruction can be incomplete or degraded by different phenomena and experimental features[(1)]:

- event depending degradation
    1. jet overlap;
    2. pile-up from multiple interaction;
    3. background from spectator partons ("underlying event" – UE);
- detector depending degradation
    1. incomplete hermeticity of the calorimeter;
    2. non uniform or time-dependent detector response;
    3. finite detector resolution;
    4. biased clustering algorithm;
    5. electronics dead time.

Correction algorithms, the "jet energy corrections" (or, simply, "jet corrections"), were developed to overcome these limitations and allow extrapolating the jet parameters to the parton level

[(1)] Because of these effects the jet energy as obtained from direct calorimeter measurements is often referred as "raw" jet energy.

[41]. There are several levels of generic[(2)] jet corrections for `JetClu` jets at CDF: each level is conceived to correct for a different degradation cause. The level numbering scheme is as in Run I, although the Run I corrections at level 2 and 3 are now included in other levels.

• η-dependent Correction (L1)

The level 1 of generic jet corrections takes into account aging of the calorimeters and the different detector response in η, depending on cracks, on different technologies employed in different sectors and on the dead zones occupied by the mechanical structure of the detectors. This correction is data-driven and is obtained by studying p_T balancing in dijet events. The response is normalized to the central calorimeter, which is better calibrated and understood (Section 3.4). The events are selected by requiring only two jets in the calorimeters, with one (called "trigger" jet) in the $0.2 < |\eta| < 0.6$ region of the central calorimeter which is far away from the cracks, the second jet (called "probe jet") being free to span all over the covered eta range up to $|\eta| \simeq 3$. For each dijet pair the balancing fraction is defined as:

$$f_b = 2 \cdot \frac{p_T^{prb} - p_T^{trig}}{p_T^{prb} + p_T^{trig}} \ . \tag{5.1}$$

As it is found that the distribution of f_b in each pseudorapidity bin is nearly Gaussian (not true for p_T^{prb}/p_T^{trig}) the chosen correction factor is then (Figure 5.1):

$$\beta = \frac{2 + \langle f_b \rangle}{2 - \langle f_b \rangle} \ , \tag{5.2}$$

which is in average equal to p_T^{prb}/p_T^{trig}. The actual L1 correction function is $f_\eta(R, E_T^{raw}, \eta) = 1/\beta(\eta)$. After multiplying $E_T^{raw}(R)$ by $f_\eta(R, E_T^{raw}, \eta)$, the new distribution of β is nearly flat around $\beta \simeq 1$. The remaining discrepancies are associated to the uncertainty in the evaluation of the global correction factor. This error can vary from 0.5% to 7.5%.

• Multiple Interaction Correction (L4)

The number of $p\bar{p}$ interactions per bunch crossing is Poisson distributed with a mean value which is luminosity dependent. Some reference values at Tevatron are $\mathcal{L} = 10^{32}$ cm^{-2}s^{-1} $\Rightarrow \langle N \rangle \simeq 3$ and $\mathcal{L} = 3 \cdot 10^{32}$ cm^{-2}s^{-1} $\Rightarrow \langle N \rangle \simeq 8$. Some particles produced from the additional interactions may fall into the jet cone and their energy must be subtracted from the raw jet energy after the η-dependent rescaling. A correction for this phenomenon is obtained from minimum-bias events, where a cone is drawn at random positions in the $0.1 < |\eta| < 0.7$ region and the corresponding E_T is measured. Then the E_T distribution is parametrized as a linear function of the number of vertices composed by at least 2 COT tracks (Figure 5.2). This correction is R-dependent and its total uncertainty is $\sim 15\%$, depending on $\mathcal{L}$, event topology, vertex reconstruction efficiency and fake rates.

[(2)]The word "generic" means that the jet corrections do not take into account the process or the parton from which the jet was generated. In Chapter 7 a type of specific jet corrections tuned on $WZ \to \ell\nu b\bar{b}$ production and decay is described.

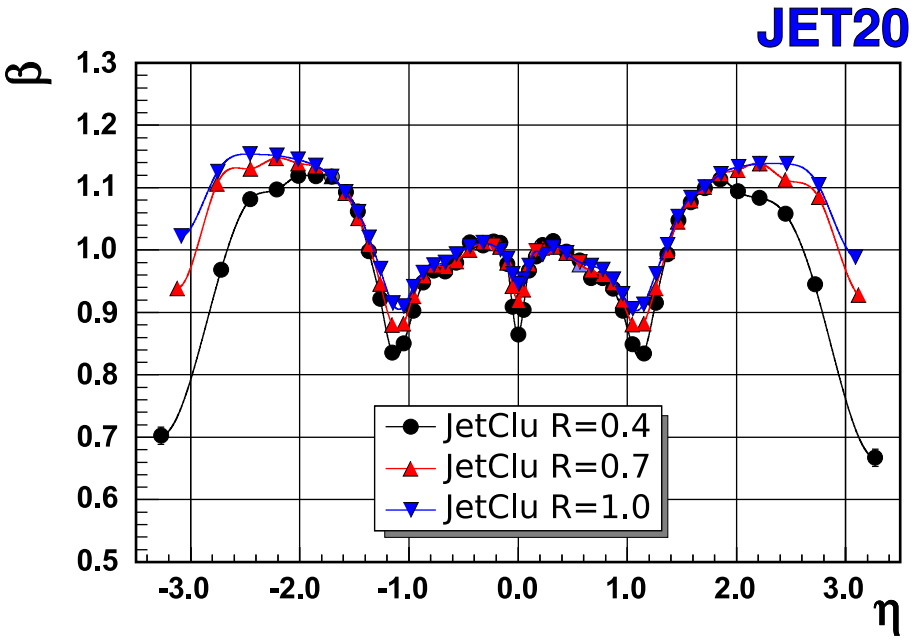

Figure 5.1: Dijet balancing as a function of η of the "probe jet" for different cone radii in the `Jet20` sample, which is made of events passing L3 trigger with at least one jet above 20 GeV.

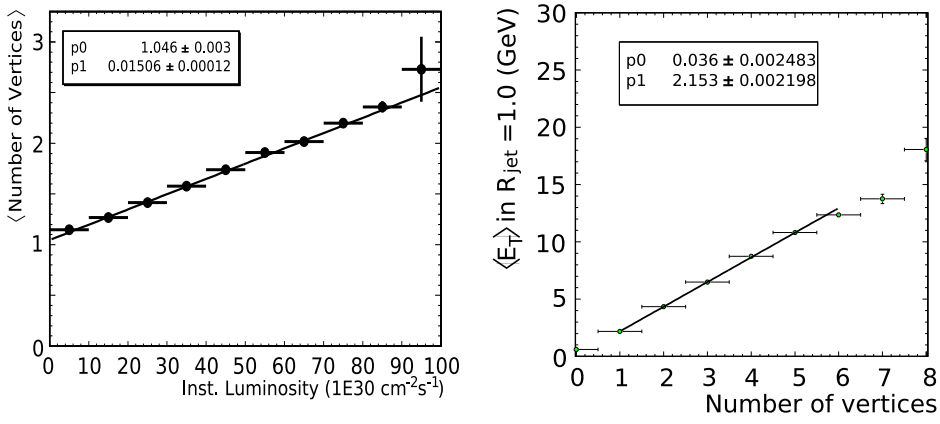

Figure 5.2: Number of reconstructed primary vertices as a function of luminosity $\mathcal{L}$ (left) and average E_T in R= 1.0 cones as a function of the number of reconstructed primary vertices in minimum bias events (right).

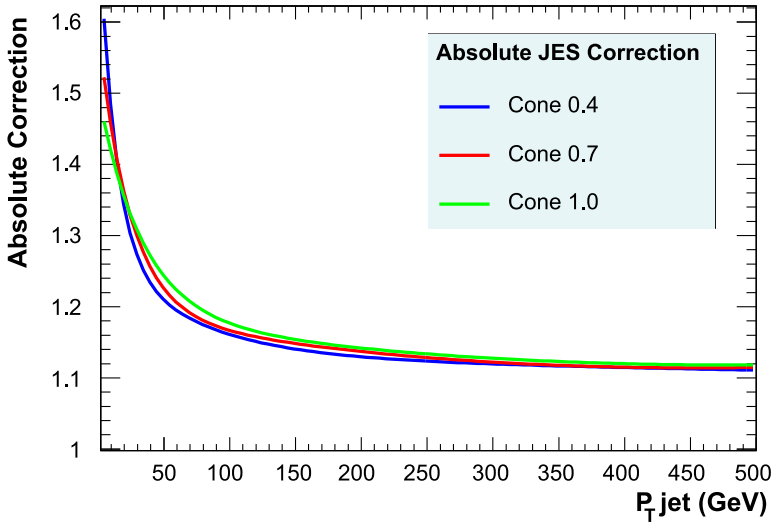

Figure 5.3: Correction factor for the absolute energy scale as a function of the jet p_T.

• Absolute Energy Scale Correction (L5)

All corrections up to L4 are at calorimeter level. The L5 jet corrections step from the calorimeter level back to the particle level. The cluster transverse momentum is converted to the sum the transverse momenta of the particles composing the jet. A large set of MC samples is generated with full CDF detector simulation and jets are reconstructed at both calorimeter and hadron levels with the same algorithm. Each calorimeter level jet C is associated to the corresponding hadron level jet H if $\Delta R_{HC} < 0.1$. The absolute jet energy is defined as the expectation value of p_T^C given p_T^H. The differences between jets from quarks and jets from gluons are not taken into account. The fragmentation model, the single particle response of the calorimeter and the calorimeter calibration in the simulations are fundamental to keep the value close to the correct one and the uncertainty small (the actual uncertainty on the correction factor is $\sim 2-3\%$). The absolute correction (Figure 5.3) brings in average the measured p_T^C to the expected value of p_T^H

• Underlying Event Correction (L6) and Out-of-Cone Correction (L7)

The final step from particle level to parton level is obtained with two additional corrections (Figure 5.4). The first one corrects for the underlying event (the background from the interaction of spectator partons and initial state gluon radiation), while the second one corrects for the fraction of energy lost because not all the jet energy flow is contained in the cone. To correct for the UE, dijet events are simulated and relative losses with respect to the parton fragmenting into the jet are computed as a function of jet energy and cone size.

The out-of-cone (OOC) corrections are needed because the radius used in the clustering al-

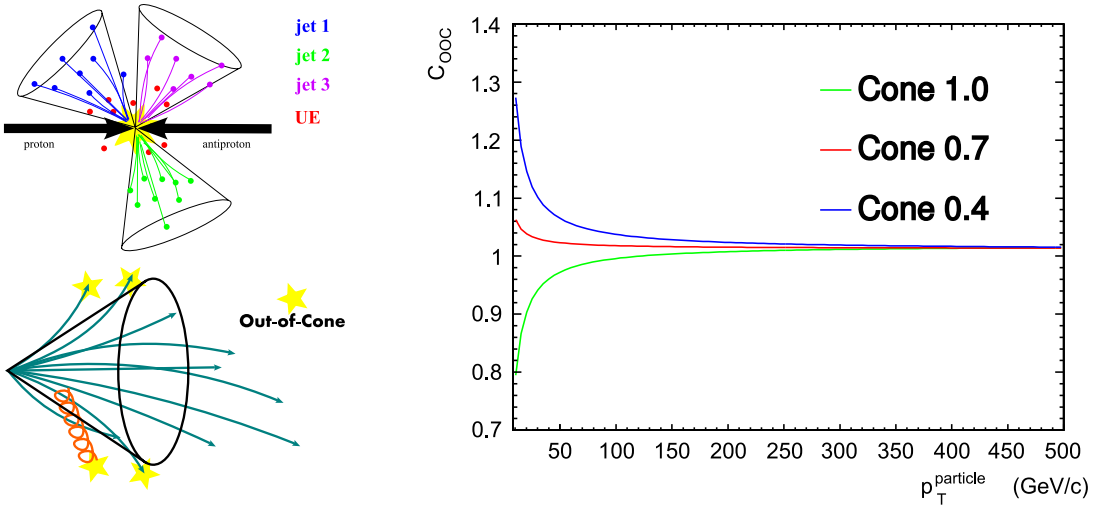

Figure 5.4: Schematic representation of UE and OOC (left) and OOC correction factor (right) as a function of jet p_T.

gorithm may not be large enough to contain the whole jet and also because gluon radiation can take some energy away from the jet. The procedure of parametrizaton is as for the UE correction. Events with exclusively one jet and one photon (γ+jet events) are used to compare the jet energy flow in a $R = 1.3$ cone balancing photon energy and p_T. Simulations show that to a high accuracy the entire jet energy is contained in such a wide cone.

The total correction to the raw jet energy is then:

$$\begin{aligned} &E_T(R, E_T^{raw}, \eta) = \\ &= (E_T^{raw}(R) \cdot f_\eta(R, E_T^{raw}, \eta) - A_{MI}(R)) \cdot f_{JES}(R, E_T^{raw}) - A_{UE}(R) + A_{OOC}(R, E_T^{raw}) \quad , \end{aligned} \tag{5.3}$$

where f_η is the L1 η-dependent correction, A_{MI} is the L4 multiple interaction correction, f_{JES} is the L5 absolute energy scale correction, A_{UE} is the L6 underlying event correction and A_{OOC} is the L7 out-of-cone correction. These corrections can equally well be applied to the E_T and the p_T of a jet, since they both rely on calorimetric information (see (4.5) and following). The contributions of the jet corrections to the uncertainty on the jet energy are shown in Figure 5.5.

5.2 Corrections to the Raw Measured $\not\!\!E_T$

The raw missing E_T for any event is defined as a vector in the $x \times y$ plane, according to (4.12) and must be corrected for the presence of muons and for errors in the raw jet energy, according to the desired level of jet corrections. The correction for muons is performed in two steps:

- the muon track is extrapolated to the calorimeters and an energy corresponding to a MIP ($\sim$ 350 MeV in CEM and $\sim$ 1.6 GeV in CHA) is removed from the total $\mathbf{p}_T$ balance;

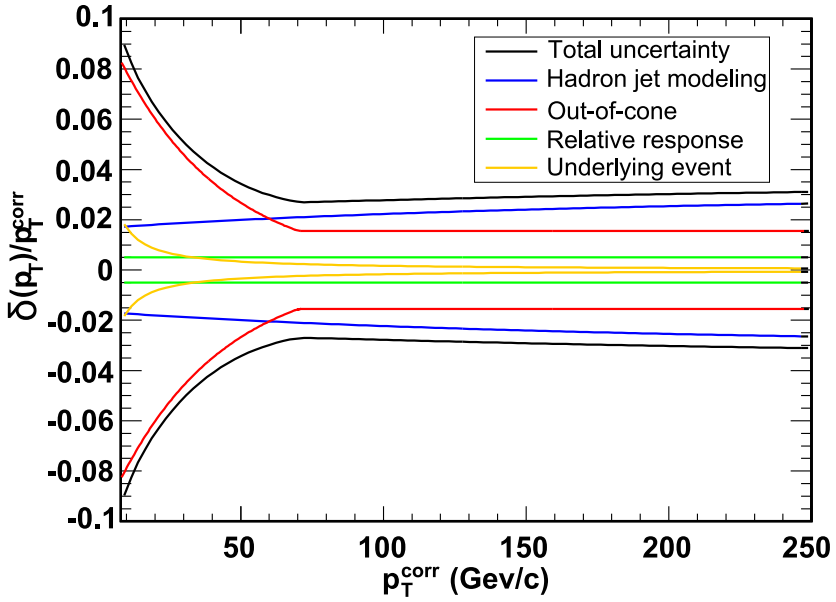

Figure 5.5: Relative systematic uncertainty on the corrected jet energy introduced by the generic jet correction as a function of jet p_T.

- the muon $\mathbf{p}_T$ is included in the total $\mathbf{p}_T$ balance.

Equation (4.12) is then changed into (5.4) in the presence of a muon:

$$\not\!\!E_T = -\sum_i E_i \cdot \sin\theta_i \cdot \hat{n}_i + E_{T_{MIP}} \cdot \hat{n}_\mu - \mathbf{p}_{T_\mu} \quad . \tag{5.4}$$

The $\not\!\!E_T$ must take into account the level of jet energy corrections too. The procedure is analogous to the correction for muons:

- the contribution given by the raw measured energy of the identified jets is excluded from the total $\mathbf{p}_T$ balance;
- each jet is corrected at the level used in the analysis and the $\mathbf{p}_T$ of all jets, corrected at the desired level, is included in the total $\mathbf{p}_T$ balance.

In order to avoid underestimating the total activity in the calorimeters because of the minimum bias energy subtraction in jet corrections, the jets are corrected in this case excluding L4 correction if the applied level is superior[3]. The final expression for the corrected $\not\!\!E_T$, for a level n of jet energy corrections, is then[4]:

$$\not\!\!E_T^{@Ln} = -\sum_i E_i \cdot \sin\theta_i \cdot \hat{n}_i + E_{T_{MIP}} \cdot \hat{n}_\mu - \mathbf{p}_{T_\mu} + \sum_j \mathbf{p}_{T_j}^{RAW} - \sum_j \mathbf{p}_{T_j}^{(@Ln-L4)} \quad . \tag{5.5}$$

[3] This is what is meant by the superscript $^{(@Ln-L4)}$ in (5.5). It is assumed that the energy due to MB events be randomly distributed in ϕ.

[4] The index j runs on all the identified and reclustered jets.

5.3 Identification of Heavy Flavored Hadrons in Jets

Jets originating from a b or c quark contain a "heavy flavored" hadron (HF), which binds the primary heavy quark. These hadrons, when identified, are a clear signature of the presence of a b or c quark in the final state of the elementary interaction which took place in the event. Some examples are the decays of top quark, SM light Higgs boson and $Z \rightarrow b\bar{b}$, all of which contain large pt b quarks. The identification of b-hadrons in jets was fundamental for the discovery of the top quark in 1995 (see Figure 5.6) and is one of the crucial features of the searches for SM light Higgs boson at the Tevatron collider. Since b quarks are involved in the most interesting processes studied at the Tevatron, the HF identification algorithms are tuned to the properties of b-jets, although some of them have a significant efficiency for c-hadrons too. Such algorithms are called "b-taggers" and exploit different properties of the b-hadrons, from the lifetime to the semileptonic decays [42].

• Identification of b-hadrons by Secondary Vertices

The main procedure to identify b-hadrons inside jets relies on their long lifetime, $c\tau \sim 450\ \mu$m, and, besides being the one adopted throughout this work, it is the first and most succesful b-tagger developed by the CDF collaboration. A long-lived heavy hadron decaying to hadrons produces a small jet whose associated tracks have large impact parameter with respect to the primary vertex of the event. The vertex of origin of these tracks may also be distinguishable from the primary one, due to the macroscopic distance traveled by the b-hadron before decay. For this reason this algorithm is called Secondary Vertex b-tagger (SECVTX). SECVTX exploits primarily the information provided by the high-precision silicon trackers SVX II, L00 and ISL (Section 3.2).

SECVTX tries to match large impact parameter (d_0) tracks to a common vertex different from the primary one. For each jet only the tracks within the jet cone (i.e. $\Delta R_{jet,trk} < R_{jet}$) are examined. The standard SECVTX mode of operating ("Tight SECVTX") is described below. Two additional modes (called "Loose" and "Ultratight") differ only in the applied thresholds.

Selected tracks must have a minimum number of hits in the silicon detectors (the requested number of hits depending on track quality and location), $p_T > 0.5$ GeV, $|d_0/\sigma_{d_0}| > 2$ and must be seeded or confirmed by a COT track. Tracks are combined together two by two in order to find a seed secondary vertex. Once a seed is found, other tracks from previous selection are added to the vertex and a quality χ^2 is computed. Tracks are iteratively checked and removed if their contribution to the χ^2 is too large. Once a "stable" vertex is found, some further quality cuts are applied, in particular the vertex is required to be associated to at least 3 tracks. Vertices consistent with long lived light flavor hadrons (K_L, $\Lambda \ldots$) or nuclear/material interactions are removed. Each candidate secondary vertex is characterized by its distance L_{xy} from the primary one. The jet is Tight-SECVTX b-tagged if $|L_{xy}/\sigma_{L_{xy}}| > 7.5$.

If no secondary vertex is found, a second attempt is made with candidate seeds with 2 tracks of improved quality. The tag is defined positive or negative according to the sign of $\mathbf{L}_{xy} \cdot \mathbf{p}_{T_{jet}}$.

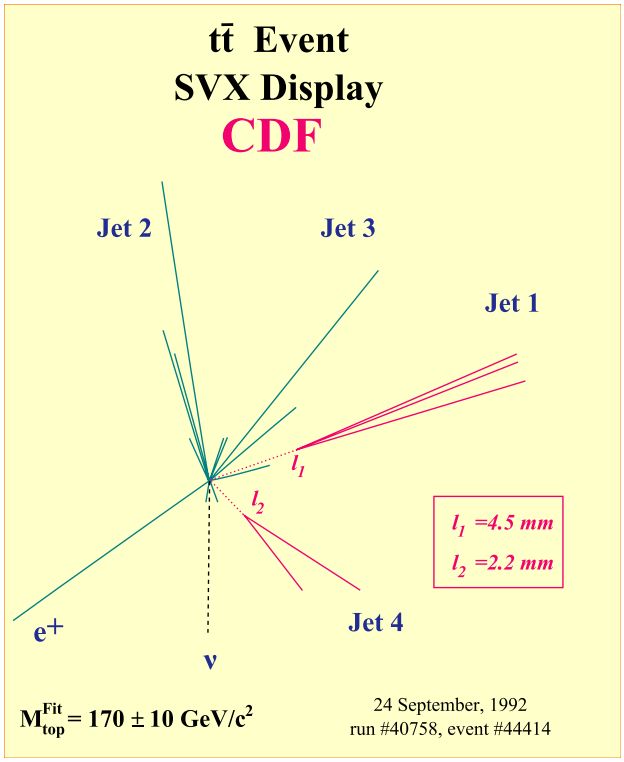

Figure 5.6: Display of one of the first candidate $t\bar{t}$ production events observed at CDF in Run I: two clear secondary vertices are identified with the aid of the SVX detector.

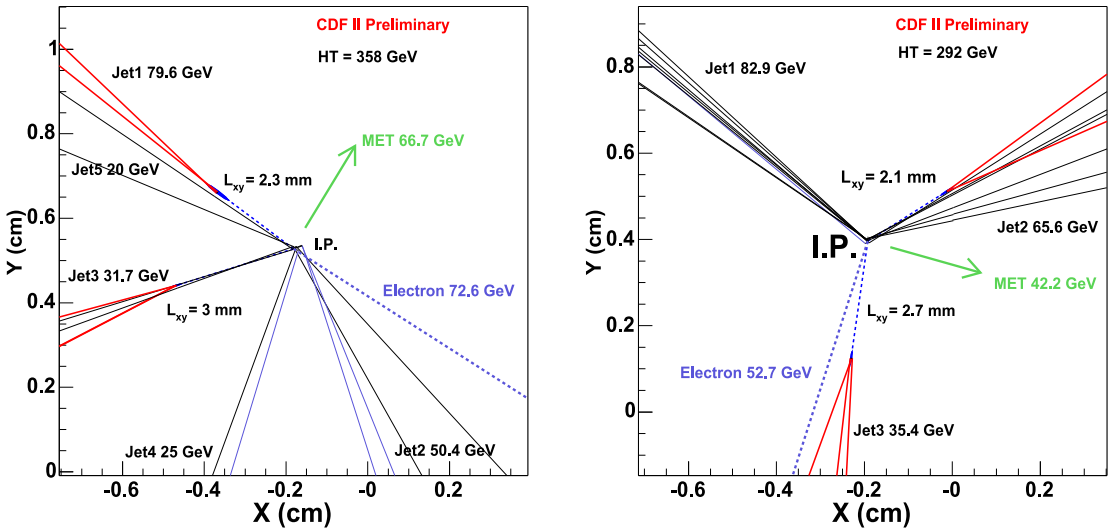

Figure 5.7: Display of two double-tag $t\bar{t}$ candidates in Run II.

Negative tags have no physical meaning (the secondary vertex is further away than the primary one in the jet direction) and are due to the finite tracking resolution. The SECVTX tagging performances are evaluated according to two parameters: tagging efficiency and purity.

Efficiency and Scale Factors

The efficiency of SECVTX is the ratio of the number of SECVTX b-tagged jets and the number of jets contained in the fiducial region of the COT and the calorimeters. Since no available MC models b-hadrons production and decay and charge deposition in the trackers well enough to allow a reliable estimate of the efficiency, efficiency measurements are data-driven. Two methods are used at CDF. The first method looks in the inclusive jet event sample for jet pairs consistent with HF pair production. If two jets are back-to-back in ϕ and one of them is matched to a high p_T muon according to the usual $\Delta R_{\mu,jet} < R_{jet}$ criterion, while the other one is SECVTX b-tagged, the jet pair is assumed to be generated by HF pair production. The muon p_T relative to the jet axis, which is large in b-jets, is used to separate b-jets from background from c and LF jets, whose fractions are determined from MC. The jet matched to the muon is used to compute the efficiency. The same procedure is performed on MC dijet events and the ratio between the efficiencies is used as scale factor (often indicated by Φ) between data and MC when simulations are needed.

The second method exploits electrons instead of muons and deserves particular attention in excluding electrons from photon conversion. The tagging efficiency is a function of the kinematics of the event, as shown in Figure 5.8. The combined scale factors for the different operating points of SECVTX obtained with 1.2 fb^{-1} of collected data at CDF are [43]:

$$\begin{array}{lll} \text{Loose:} & \Phi_L = & 0.95 \pm 0.01\ (\text{stat}) \pm 0.05\ (\text{syst})\ , \\ \text{Tight:} & \Phi_T = & 0.95 \pm 0.01\ (\text{stat}) \pm 0.04\ (\text{syst})\ , \\ \text{Ultratight:} & \Phi_U = & 0.88 \pm 0.01\ (\text{stat}) \pm 0.05\ (\text{syst})\ . \end{array} \tag{5.6}$$

Purity and False Positive Tags

The second parameter of interest in SECVTX performances is the fraction of b-tagged jets which are true b-jets. Mistags are due to tracks having large d_0 because of the finite detector resolution, interactions with the detector material and early decays of long lived LF hadrons.

The rate of mistags due to detector resolution can be inferred by the number of negative tags, since they are expected to be symmetric with respect to the primary vertex. The probability of having a mistagged jet is obtained from the probability of having a negative tag, which is parametrized as a function of jet E_T, ϕ, η, track multiplicity and number of jets in the event. The predicted mistag rates at CDF are calculated from inclusive jet data samples. The contribution of other sources of mistags are derived from MC simulations. Further details are given in Section 8.3.

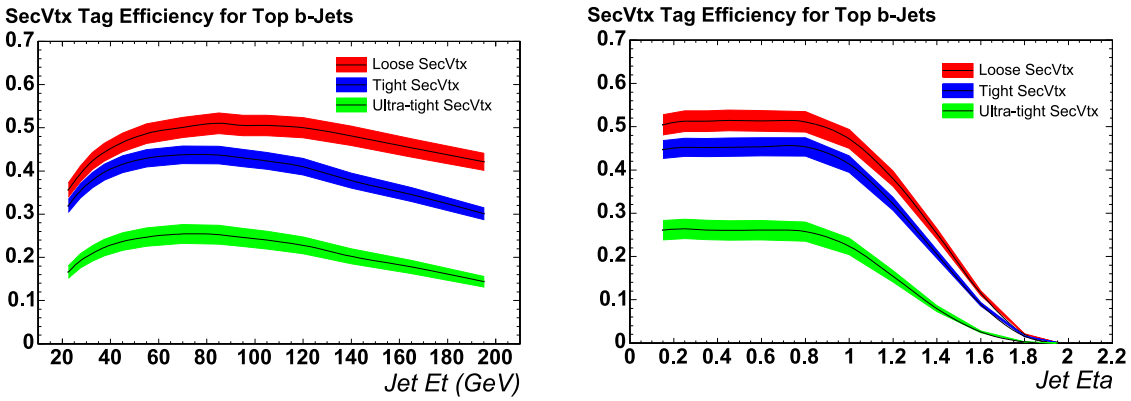

Figure 5.8: Efficiency to tag jets in top quark Monte Carlo samples which have been matched to b quarks, using the "tight", "loose" and "ultra-tight" tunes of the SECVTX tagger in function of jet E_T (left) and $|\eta|$ (right). The efficiency is obtained by multiplying the tag rate in the Monte Carlo by the measured data/MC scale factors of (5.6). The bands represent the systematic error on the data/MC scale factors. The decrease in efficiency at high jet E_T is due to declining yield of good silicon tracks passing the quality cuts.

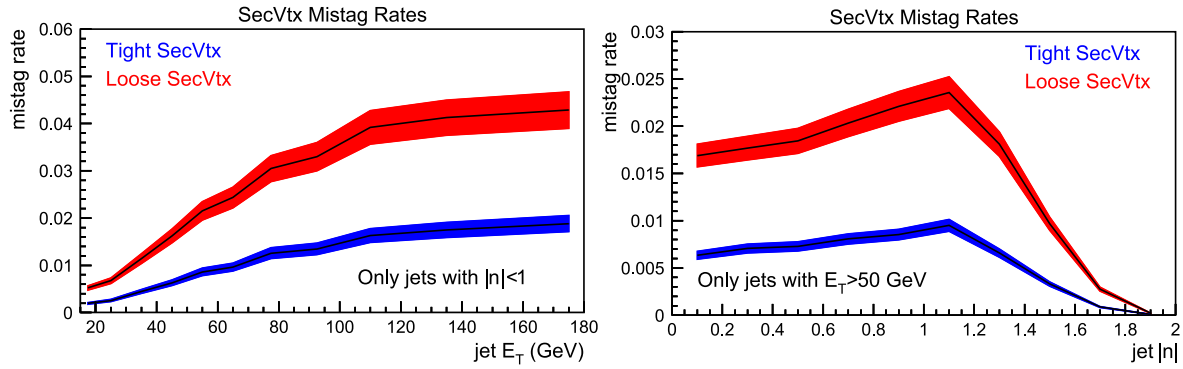

Figure 5.9: Mistag rate from light quark jets, measured from inclusive jet data, using both "tight" and "loose" tunes of the SECVTX tagger as a function of jet E_T (left) and $|\eta|$ (right).

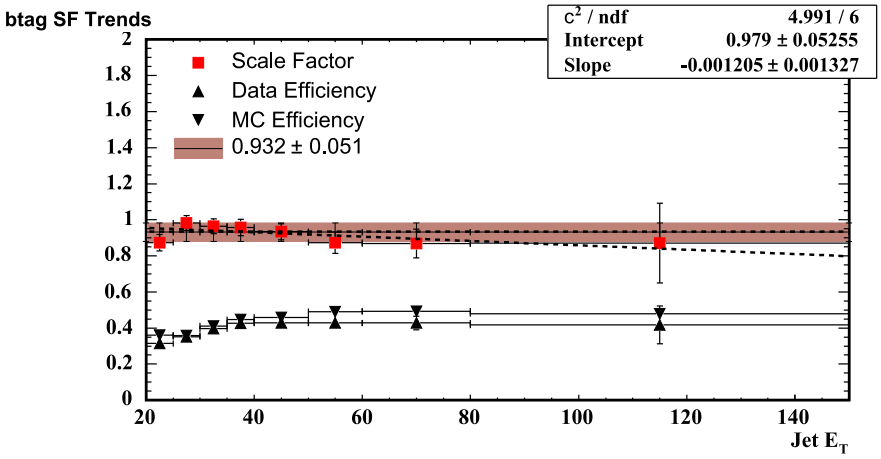

Figure 5.10: Determination of the data/MC scale factors (SF) for the "tight" SECVTX tagger with the muon method, as a function of jet E_T.

• Other b-taggers

Other b-taggers at CDF exploit a number of properties of b-jets. The Soft Lepton Tagger (SLT) [44] exploits the high rate of large p_T semileptonic decays of b-hadrons and is also of frequent use. Currently a SLT for decays involving muons is available at CDF, while a similar code exploiting electronic decays is being developed. The SLTμ tagger makes use of a likelihood function combining all the available information about the candidate soft muon as gauged by studies of certified heavy flavor data sample. The SLTμ tagging efficiency is $\sim 13\%$ while the mistag probability is $\sim 0.7\%$. Another b-tagger of frequent use at CDF is the Jet Probability Algorithm (JP) [45]. By scanning the impact parameters of the tracks contained in a jet and their uncertainties, it returns the probability for all of them to come from the primary vertex of the interaction. The probability distribution for heavy flavor jets is peaked at 0 JP. Setting the tagging threshold at 1% (5%) the Jet Probability tagging efficiency is measured to be $\sim 26\%$ ($\sim 33\%$). In addition some neural network multivariable b-taggers have been developed by different groups at CDF. These taggers have not been widely used so far but a remarkable effort is being produced now to create a new neural network b-tagger to be capable of incorporating all the information exploited by others into the same one. This new b-tagger is expected to be capable of identifying secondary, tertiary vertices and soft leptons in heavy flavor jets and distinguishing between b- and c-jets.

6. Event Selection and Overview of the Measurement

6.1 Event Selection

This study is an attempt to observe the associated production of W and Z bosons in the "golden" channel for the light SM Higgs boson search at the Tevatron ($WH \rightarrow Wb\bar{b}$). The event selection was tuned with this goal in mind:

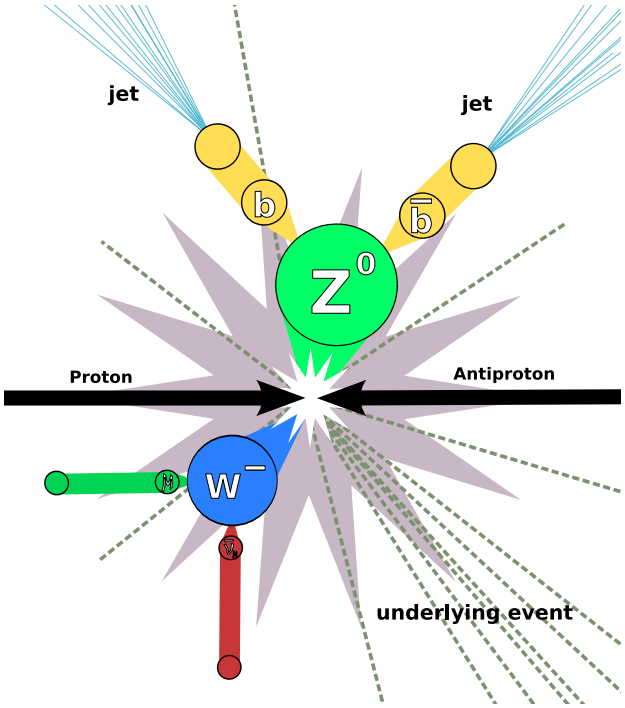

Figure 6.1: Pictorial view of the signature of $WZ \rightarrow \ell\nu b\bar{b}$ events.

- the selected events must show a signature consistent with W production: to have a clear W signature, events are searched for semileptonic decays of the produced $W \rightarrow \ell\nu_\ell$, where the

Period	Dates Taken	Run Range
`0d`	Up to 22 Aug, 04	138425 – 186598
`0h`	7 Dec, 04 – 4 Sep, 05	190697 – 203799
`0i`	5 Sep, 05 – 22 Feb, 06	203819 – 212133
`0i/8`	9 June, 06 – 1 Sep, 06	217990 – 222426
`0i/9`	1 Sep, 06 – 22 Nov, 06	222529 – 228596

Table 6.1: Stored run ranges for the different data acquisition periods used in this analysis.

lepton ℓ can be a final state electron or muon[(1)];

- the selected events must show a signature consistent with a Z decaying to b-quark pairs: $Z \rightarrow b\bar{b} \rightarrow 2$ jets. This is checked by making use of both SECVTX b-tagging and by requirements on the dijet invariant mass.

Events tagged by SECVTX enter the so-called b-tagged "lepton+jets" event sample. Additional strict requirements are imposed on the the reconstructed objects of this sample in order to improve the event quality.

• Requirements on the Whole Event

Event Storage and Triggers

Since the first property of selected events is the presence of a leptonically decaying W boson, the trigger paths used for this analysis require a high p_T lepton. The run ranges corresponding to the different data acquisition periods are listed in Table 6.1. Good runs are selected from dedicated lists differing in the CDF subdetectors required to be active. These lists include only runs corresponding to an optimal beam status. This analysis requires either electron or muon identification, including the early Run II period when CMX was not available, and active silicon detectors when making use of SECVTX b-tagging. The specific physical properties of each used trigger path are listed in Appendix B.

Requirements on the Physical Objects and Vetoes

The selected events must be characterized by the following reconstructed objects. Jets and $\not\!\!E_T$ are corrected at L5 of generic jet corrections before applying any cut:

- one tight and isolated lepton (the definition of tight lepton is given in Section 6.1, distinguishing by lepton type) matched to the correct fired trigger, according to Table 6.2;
- the trigger lepton can be an electron (either CEM plus COT track or PEM plus PHX track) or a muon (either CMUP, i.e. CMU plus CMP stubs, CMX or BMU muons associated to COT tracks);

(1) W decays to taus can also satisfy these conditions if the τ decays leptonically: $W \rightarrow \tau\nu_\tau \rightarrow \ell\nu_\ell\nu_\tau$.

Lepton	Lepton type	Trigger path
electron	CEM	ELECTRON_CENTRAL_18
	PHX	MET_PEM
muon	CMUP	MUON_CMUP18
	CMX	MUON_CMX18
		MUON_CMX18_L2_PT15
		MUON_CMX18_&_JET10
	BMU	MUON_CENTRAL_JET20_L1_BMU10_BSUR
		MUON_CENTRAL_JET20_L1_BMU10_PT11

Table 6.2: Summary of the triggers used for the different lepton types. The different trigger paths are described in Appendix B.

- exactly two JetClu jets with $R = 0.4$, both with $E_T > 15$ GeV and $|\eta^{det}| < 2$ ("tight jets"), or, in alternative, one tight jet plus one additional jet with $E_T > 12$ GeV and $|\eta^{det}| < 2.4$ ("loose jet");
- $\not\!\!E_T > 20$ GeV.

In addition, the selected events must pass certain vetoes built to reject specific classes of events which are not interesting in this work:

- Dilepton Veto: the total number of tight/isolated, tight/non-isolated, loose and extra leptons must be exactly 1;
- Z Veto: the invariant mass $m_{\ell,trk}$ of the reconstructed lepton and the highest p_T track must be outside the Z mass window $[76, 106]$ GeV;
- Cosmic Veto: the vertex of the tracks associated to muons must be within a fiducial region around the interaction point;
- Different Interaction veto: the track z_0 of the trigger lepton must within 5 cm from the z of primary vertex of the event;
- non-W Veto: the transverse mass of the lepton-candidate neutrino pair must be larger than 20 GeV, the angle $\Delta\phi_1$ between the lepton $\mathbf{p}_T$ and $\not\!\!\mathbf{E}_T$ must have $\cos\Delta\phi_1 < 0.9$ and, if $\not\!\!E_T < 30$ GeV, the angle $\Delta\phi_2$ between the leading selected jet and $\not\!\!\mathbf{E}_T$ must be $0.5 \leqslant \Delta\phi_2 \leqslant 2.5$.

Since this analysis relies on Tight SECVTX b-tagging, the selected events are classified according to the number of SECVTX b-tagged jets:

- pretagged: jets are not inspected for b-tags, no request is made on the status of silicon. This sample is fully inclusive;
- non-tagged: none of the jets is tagged or the silicon detectors were not active during the collection of the event;

- tagged: at least one of the selected jets is tagged;
- 1-tag: exactly one of the selected jets is tagged;
- 2-tags: both the selected jets are tagged.

Electrons are identified by their large energy deposition into EM calorimeters and therefore are included in the jet list. Therefore one must remove their contribution to the jet list before handling jets. In this analysis both tight isolated and tight non-isolated electrons are removed.

Since the 2-tags events are too few to allow a separate study, it is assumed that the second selected jet is a b-jet even if non-tagged. Even so, because of the Z-window cut (Chapter 7) and of the exclusive 2-jets requirement made in order to limit the $t\bar{t}$ contamination (Figure 6.2 [46], [47]) the tagged event sample is still rather limited. The motivation for the choice of $R = 0.4$ jets relies mainly on the portability of some calibration factors, which were measured for $R = 0.4$, and on the availability of SECVTX information, which is complete only for $R = 0.4$ in the standard CDF information provided to the users. A comment on the impact of choosing $R = 0.4$ rather than $R = 0.7$, is made in Chapter 7, together with the presentation of the final steps of the event selection and the choice of the dijet invariant mass window[(2)]. The MC "acceptance tables", from which the efficiency of each selection step for the signal and the main backgrounds can be evinced, are listed in Appendix C.

• Individual Requirements for Reconstructed Leptons

Electron

A tight electron must have $E_T \geqslant 20$ GeV and the z_0 of its track must be < 60 cm. Further requirements are different between CEM and PHX electrons:

- CEM[(3)]
  - ▷ the associated track must have $p_T \geqslant 10$ GeV, must be built from at least 3 COT axial segments and 2 COT stereo segments and must lie in the COT fiducial region;
  - ▷ the energy share between hadronic and EM calorimeters must satisfy the condition $E^{had}/E^{EM} < 0.055 + 0.00045 \cdot E$;
  - ▷ the electron must not be compatible with photon conversion;
  - ▷ $E/p \leqslant 2$ unless track $P_T \geqslant 50$ GeV;

[(2)] As already stated, this work is a first attempt to observe WZ production in the $\ell\nu b\bar{b}$ channel. Many of the selection cuts (particularly in terms of jet energy, jet pseudorapidity, jet number and dijet invariant mass) can be further optimized in future studies.

[(3)] The definition of "loose" CEM electrons differ from the "tight" ones for the absence of the E/p and CES requirements.

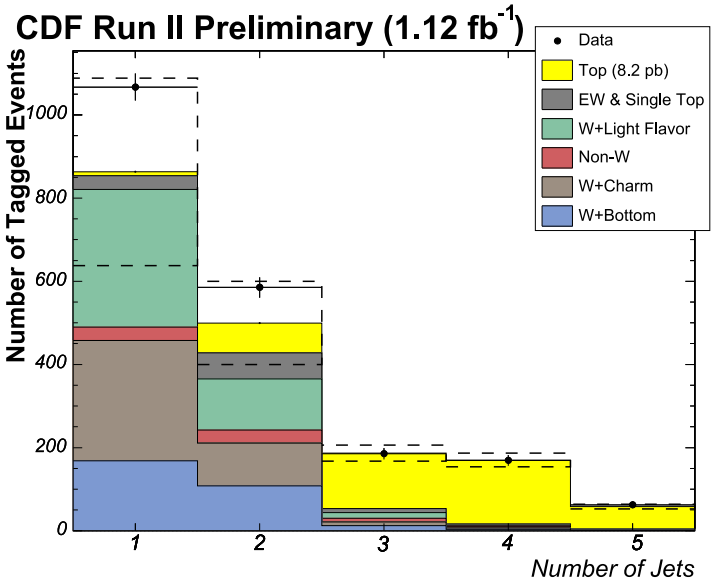

Figure 6.2: b-tagged lepton+jets sample composition leading to $t\bar{t}$ production cross section measurement. At large jet multiplicity $t\bar{t}$ production dominates and any observation of other small cross section processes would be very difficult. Dashed lines indicate the uncertainty on the $t\bar{t}$ contribution when renormalized to the measured cross section.

- ▷ the measured charge Q and the distance Δx on the transverse plane between the extrapolated track and the CES shower must satisfy the condition $1.5 < \Delta x \cdot Q < 3$ cm, as determined for test beam electrons;
- ▷ the distance Δz between the extrapolated track and the CES shower on the longitudinal plane must be < 3 cm;
- ▷ the shower profile in CES must be analogous to the one obtained in test beam measurements;

• PHX

- ▷ the track must be built from at least 3 hits in the silicon detectors;
- ▷ the energy share between hadronic and EM calorimeters must satisfy the condition $E^{had}/E^{EM} < 0.05$;
- ▷ the shower in the PES must be in the $1.2 < |\eta| < 2$ region;
- ▷ if $E_T \leqslant 100$ GeV, the shower profile in PES is checked against test beam results;
- ▷ the quality χ^2 of the PEM cluster match to the track must be $\leqslant 10$;
- ▷ the distance between the PEM cluster and the PES shower must be at most 3 cm.

Finally, the electron is called "isolated" if the ratio between additional E_T flow in a $R = 0.4$ cone centered on the electron and the E_T of the EM cluster (called "isolation") is < 0.1.

Muon

A number of general requirements must be satisfied for a track to be listed as a muon candidate:

- ▷ a tight muon must have $p_T \geqslant 20$ GeV and the z_0 of its track must be < 60 cm;
- ▷ the associated track must be built from at least 3 COT axial segments and 2 COT stereo segments (except for BMU muons);
- ▷ the associated track must lie in the proper fiducial region, according to the muon type;
- ▷ the associated track must have impact parameter $d_0 < 2$ mm if no silicon hits are used in track building, $d_0 < 0.2$ mm otherwise;
- ▷ the distance Δx on the transverse plane between the extrapolated track and the stubs must be smaller than a reference value comprised between 5 and 9 cm, depending on muon type;
- ▷ the maximum energy deposition must be $(6 + \max(0, 0.028 \cdot (p_T - 100)))$ GeV in the hadron calorimeter and $(2 + \max(0, 0.0115 \cdot (p_T - 100)))$ GeV in the EM one;
- ▷ the quality χ^2 of the reconstructed track must be less than 2.3 (13 for BMU).

The definition of isolated muon is the same as for the electron. There are further requests which are peculiar of the different muon types:

- CMUP: the extrapolated track must be matched to both CMU and CMP stubs;
- CMX: the selected muons must not be triggered by non-operating wedges of CMX arches during particular runs and the exit radius of the track from the COT must be $\geqslant 140$ cm;
- BMU: the ratio between the total number of stereo and axial hits in the COT and the number of possible hits compatible with the track must be > 0.6.

6.2 Overview of the Analysis

The main purpose of this analysis is the identification of b-jets consistent with Z production in a $W+2$ jets sample and the measurement of the $p\bar{p} \to WZ+X$ cross section. Should a cross section measurement be out of reach, an upper limit would be derived.

The first step in this procedure is to constrain the dijet invariant mass to be consistent with the $Z \to b\bar{b}$ hypotesis. This constraint was made more accurate by developing a set of event-specific jet energy corrections that can be used instead of levels 6 and 7 generic jet corrections, which do not take into account the specific nature of the process nor the possible HF nature of the associated jets to the W. This part of the work is described in Chapter 7.

A wide set of MC samples is used to determine acceptance and tagging efficiency for all processes leading to the final state $\ell\nu + 2$ jets. These efficiencies are then used to determine of the composition of the selected data. The procedure adopted is the called "method 2" in CDF jargon, which constrains the background composition by weighting the contributions of the background processes by their theoretical cross section. The implementation of "method 2", with some changes tuned to $WZ \to \ell\nu b\bar{b}$, is described in Chapter 8.

Once the background composition of the sample is known, the cross section of the signal process can be extracted, as described in Chapter 9 together with estimate of some of the systematic uncertainties. Concluding remarks are presented in Chapter 10.

7. Optimization of the Z-window on Dijet Invariant Mass

The generic jet corrections up to L5 return a jet which is supposed to correspond to the hadron level. To get a dijet invariant mass in $WZ \to \ell\nu b\bar{b}$ events which is centered on the Z mass one must in addition apply corrections to account for the loss of energy flow outside the jet cone due to reclustering algorithm, gluon radiation and heavy flavor nature of the jet. The way jets are defined, corrected and used is crucial within this context, and some of the possible scenarios are explored in this chapter by studying two different WZ PYTHIA MC samples: one includes all W and Z decays with the known branching fractions, while the other one has the WZ pair forced to decay to $\ell\nu b\bar{b}$. The forced sample is used to construct the specific corrections and the inclusive one is used to test them and to derive all the predictions needed for estimating the sample composition.

7.1 b-tagging Information for `JetClu` Jets with $R = 0.7$

Since the purpose of this study is to identify $Z \to b\bar{b}$ decays, the specific corrections are built from studying the desired signal and must be applied only to the selected jets in tagged events before introducing the cut on dijet invariant mass. However, as stated in Section 6.1, SECVTX information is available and complete only for $R = 0.4$ jets in the standard CDF framework.

In order to check the effects of the choosing $R = 0.7$, the optimal choice would be to reprocess the datasets allowing the b-tagger to run over $R = 0.7$ jets too. A different choice, which is more straightforward and less demanding in terms of computing resources, is to match the jets reconstructed with $R = 0.4$ to those reconstructed with $R = 0.7$ and to transfer the SECVTX information from $R = 0.4$ jets to $R = 0.7$ jets. This was considered a good enough approach to the goal and was adopted in this study.

The chosen matching criterion is the $\Delta R_{0.4,0.7} < R_{cut} = 0.4$ one. $R_{cut} = 0.4$ has been chosen in order not to allow the axis of the $R = 0.7$ jet to fall outside the $R = 0.4$ jet. The reasonableness of the choice is confirmed by the distribution of the minimum ΔR between any $R = 0.4$ jet and all the $R = 0.7$ jets reconstructed in the same event (Figure 7.1), where the rate of pairs matched at $\Delta R = R_{cut}$ is more than one order of magnitude smaller than that of aligned pairs.

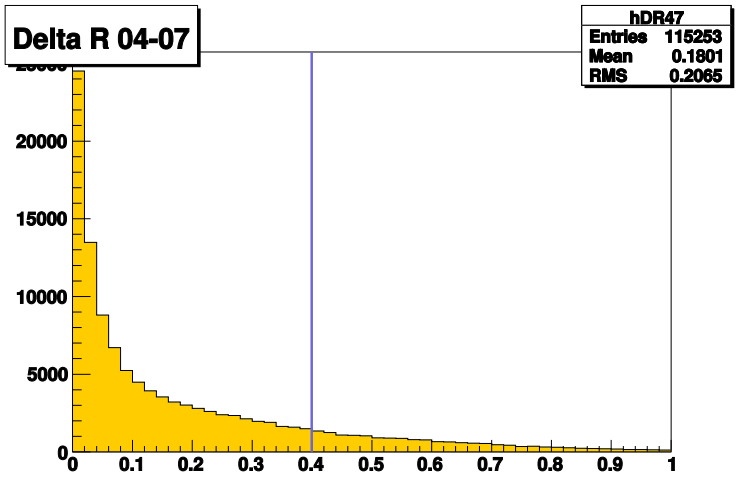

Figure 7.1: Distance in the $\eta \times \phi$ space between jets described with $R = 0.4$ and $R = 0.7$.

7.2 Construction of the Specific Jet Energy Corrections

The specific jet energy corrections aim is to derive from the hadron-level jet in tagged events the momentum of the primary b-quark. Since the degradation of the information in this step is influenced by jet multiplicity, underlying event and kinematics of the process, the specific corrections should be analysis dependent. The specific jet corrections described below were tuned to reconstruct at best the Z mass and define at best the acceptance window around it.

The forced $p\bar{p} \rightarrow WZ + X \rightarrow \ell\nu b\bar{b} + X$ MC PYTHIA sample is large enough to allow for a set of detailed studies. All MC samples used in this analysis are run-dependent: the information provided after the full detector simulation reflects the actual availability of the different subdetectors in the different runs and the number of generated events per run correctly depends on the measured instantaneous and integrated luminosity of each run. The only unrealistically large parameter is the cross section of the signal process, to allow for a larger statistics of simulated events.

Pretagged events are selected out of the whole sample, according to the prescriptions of Chapter 6. $Z \rightarrow b\bar{b}$ decays are selected in the `hepg` bank, the decay tree of the simulated event. The basic idea of these corrections is similar to the one of CDF Run II top quark mass specific jet corrections [48]: the relative response factor (RRF)

$$\mathcal{K} = \frac{p_T^b - p_T^{jet,L5}}{p_T^{jet,L5}} \tag{7.1}$$

is obtained from MC simulations where jets are associated to the corresponding b-partons,

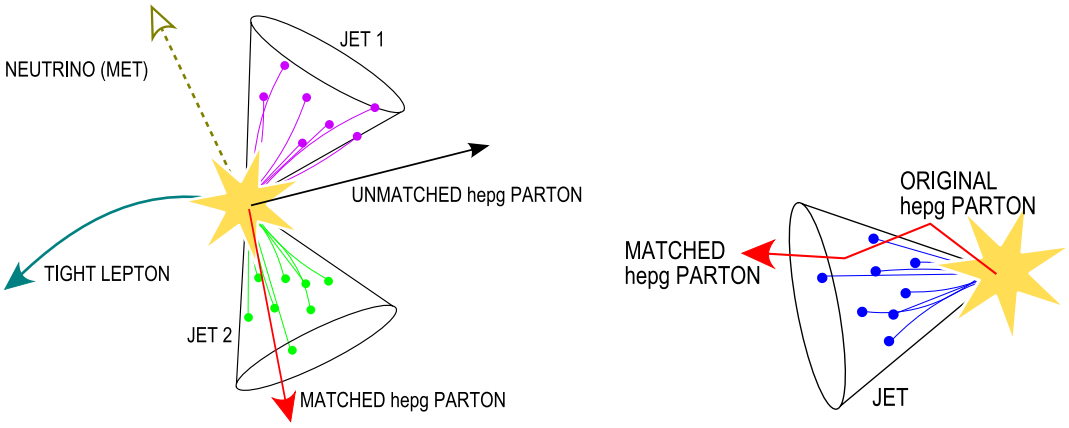

Figure 7.2: Matching procedure in the construction of the specific jet energy corrections. On the right side of the picture the effect of parton showering by PYTHIA is shown, with emphasized "mismatches". The "original" primary parton is the prompt one while the "matched" parton is the propagated one.

and is then applied to the L5 correted jet as[(1)]

$$p_{\mu}^{jet,SC} = p_{\mu}^{jet,L5} \cdot (1 + \mathcal{K}) \leftrightsquigarrow p_{\mu}^{b} \ . \tag{7.2}$$

The jet-to-parton association is done with the $\Delta R_{b,jet} < R_{jet}$ criterion. In an ideal world the "$\leftrightsquigarrow$" should be read as "=", but the relative response factor is a function of different variables and only an approximate equality can be obtained, mainly depending on the kinematics and topology of the jet. Equation (7.1) should then be changed into a response function (RF) also depending on jet η:

$$\mathcal{K}(\eta^{jet}, p_T^{jet,L5}) = \frac{p_T^{b} - p_T^{jet,L5}(\eta^{jet})}{p_T^{jet,L5}(\eta^{jet})} \ . \tag{7.3}$$

PYTHIA simulations can list the same quark many times, depending on how the parton showering is realized. During parton showering the vector momentum of the parton changes appreciably, making the following two questions arise:

- which parton should be matched to the jet?
- which parton should be used to compute the correction factor?

The solutions chosen in this analysis are based on reasonable assumptions, in consequence of a number of considerations:

- the last time one parton is listed in the `hepg` bank, it is the closest one in time to the hadron within which it is going to be bound, which is part of the final jet and should be inside the jet itself $\Longrightarrow$ the last parton is matched to the jet;

[(1)] As stated at the end of Section 5.1, the whole four-momentum of the jet is obtained from calorimetric information and the correction factors can be therefore applied also to E and p_z besides p_T.

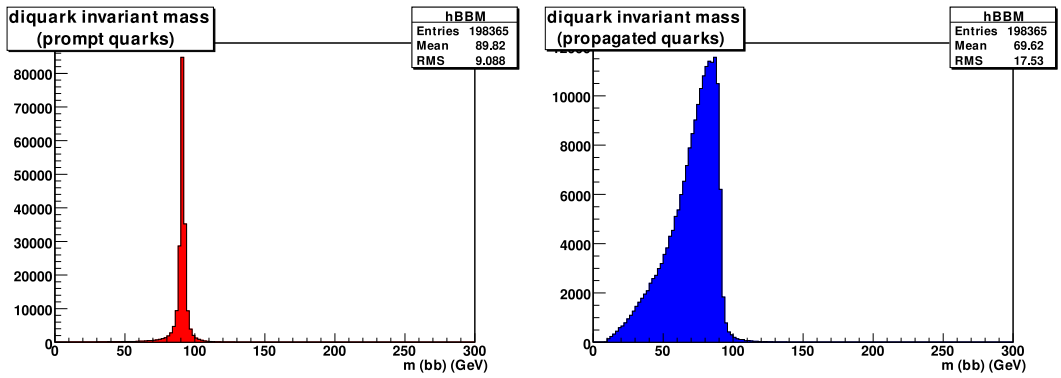

Figure 7.3: Invariant mass of b-quark pairs from Z decays reconstructed with prompt (left) and propagated (right) b-quarks.

- the first parton listed in the `hepg` bank is directly produced from the Z decay and gives a better dijet invariant mass, as shown in Figure 7.3 $\Longrightarrow$ the first parton is used to produce the jet corrections after the matching.

To check the dependence of $\mathcal{K}$ on η^{jet} and $p_T^{jet,L5}$, the $\eta^{jet} \times p_T^{jet,L5}$ space is binned assuming forward/backward symmetry. Due to the limited statistics of the PYTHIA sample, one must find the best compromise between number of bins and number of entries per bin, which are both the larger, the better. The optimal binning scheme found is shown in Figure 7.4. It features 56 bins with relatively large width in both variables. Once a parton is matched to a jet, the corresponding $\mathcal{K}$ factor is stored in a distribution associated to the bin in the $\eta^{jet} \times p_T^{jet,L5}$ space.

The large forced PYTHIA sample allows a dedicated study on the semileptonic decays of b-hadrons. Once a b-hadron decays semileptonically, part of its energy is carried away by neutrinos and is lost from the jet. If the final state lepton is a muon, the energy signaled by the calorimeter is further reduced because the muon behaves as a MIP. Since these decays of b-hadrons are frequent, a better resolution could be obtained by identifying such decays in order to apply the right correction to each jet. However, none of the available b-taggers is capable of discriminating between these semileptonic decays well enough to apply different corrections for different decays. This part of the study must then be taken as an investigation of a problem which should be solved in the future to overcome the limitations arising from it. The construction of such differential specific jet energy corrections is done by tagging the decay with a simple kinematical cut. If a final state e or μ in the `hepg` bank if found to be within a cone of $R = R_{jet}$ around the b parton, the decay is classified as semileptonic. If a match to both an electron and a muon is found, the priority is given to the muon because of the greater correction needed.

The basic idea is to parametrize the distribution of $\mathcal{K}$ as a function of η^{jet} and $p_T^{jet,L5}$, if possible. To do this, the distribution should be described by a function "as simple as possible". Well-known probability density functions were preferred because of ease of handling. The best

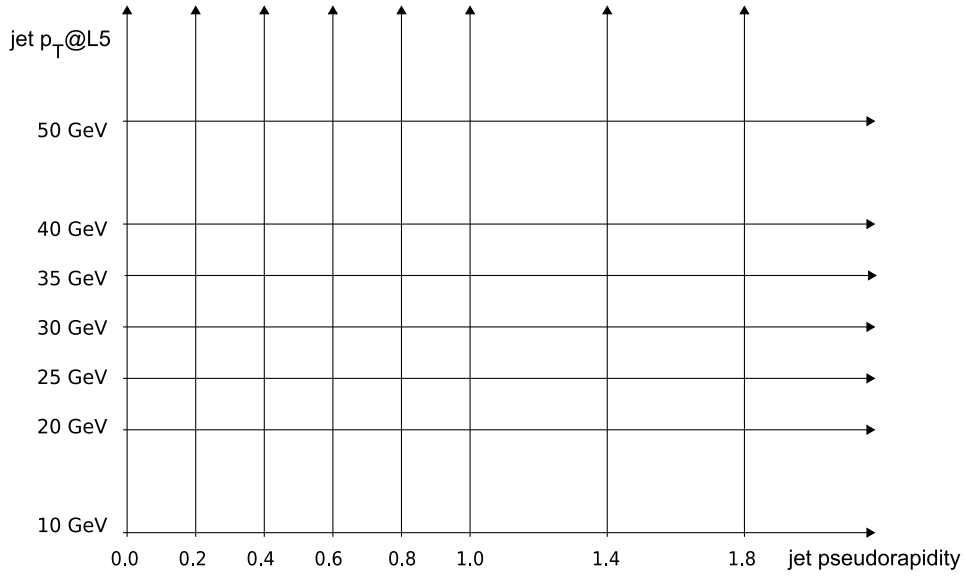

Figure 7.4: Binning of the $\eta^{jet} \times p_T^{jet,L5}$ space in the construction of specific jet energy corrections.

compromise between simplicity of the parametrization and accurate description of the distribution is obtained with the weighted sum of two Gaussians (labeled as W-wide and N-narrow):

$$f(\mathcal{K}) = \mathcal{N} \cdot (w_N \cdot \mathcal{G}(\mathcal{K}, \mu_N, \sigma_N) + (1 - w_N) \cdot \mathcal{G}(\mathcal{K}, \mu_W, \sigma_W)) \quad , \tag{7.4}$$

where $\mathcal{N}$ is the global normalization factor and w_N the weight of the narrow Gaussian. The different parameters are obtained by fitting the histograms with MINUIT according to (7.4) in the $-1 < \mathcal{K} < 4$ region. Some of the parameters are constrained. In particular, w_N is mantained between 0 and 1 and the mean values μ_N and μ_W are constrained not to fall in the lowest or in the highest bin within the fitting range. The initial values of the parameters are set as follows: $\mathcal{N}$ =integral of the histogram, $w_N = 0.8$, $\mu_{N,W}$ =mean of the histogram, $\sigma_{N,W}$ =RMS of the histogram. The fit procedure is iterated by setting the values obtained in a fit as the initial values of the next fit. Not all fits converge with the same goodness (χ^2/DOF) and some histograms could be better fitted with a different function, but the choice of a universal parametrization was preferred for sake of coherence in treating the different $\eta^{jet} \times p_T^{jet,L5}$ regions. Some examples of the $\mathcal{K}$ distributions together with the results of the fit are shown in Figures from 7.5 to 7.8. The fit χ^2 are all acceptable.

Specific corrections were built and tested both for $R = 0.4$ and $R = 0.7$ jets. Unfortunately the dependence on η and $p_T^{jet,L5}$ of the correction fit parameters cannot be easily represented by analytic functions, as a consequence of the small number and large width of the bins. Rather than constructing a probability density for $\mathcal{K}$ as a continuous function of η and $p_T^{jet,L5}$, each jet is corrected using the information extracted from the histogram associated to its bin.

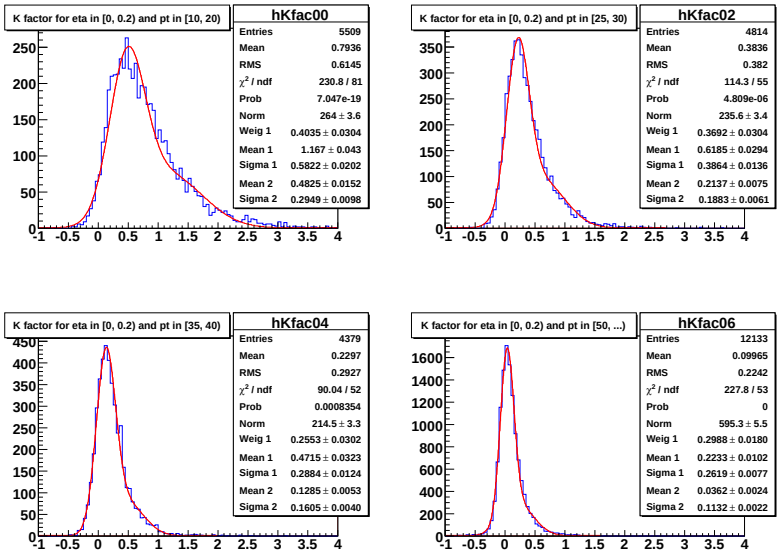

Figure 7.5: Examples of inclusive relative response functions for $R = 0.4$ selected jets: the $|\eta^{jet}|$ bin is kept fixed while different $p_T^{jet,L5}$ intervals are chosen.

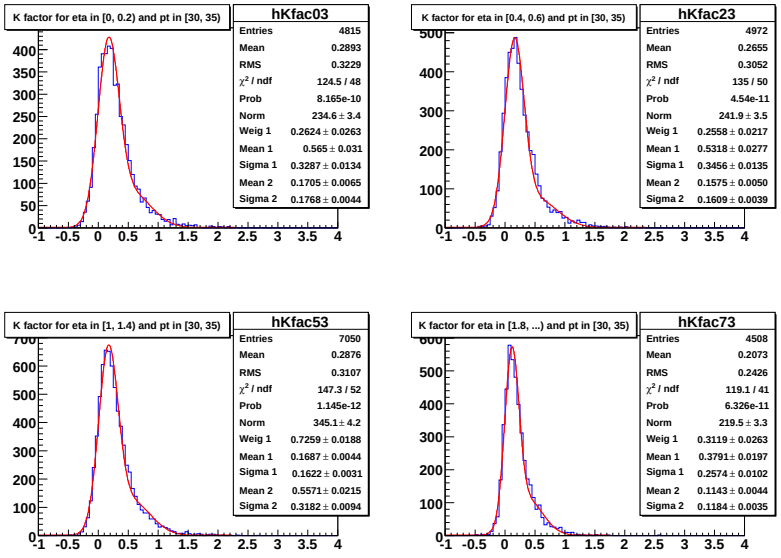

Figure 7.6: Examples of inclusive relative response functions for $R = 0.4$ selected jets: the $p_T^{jet,L5}$ bin is kept fixed while different $|\eta^{jet}|$ intervals are chosen.

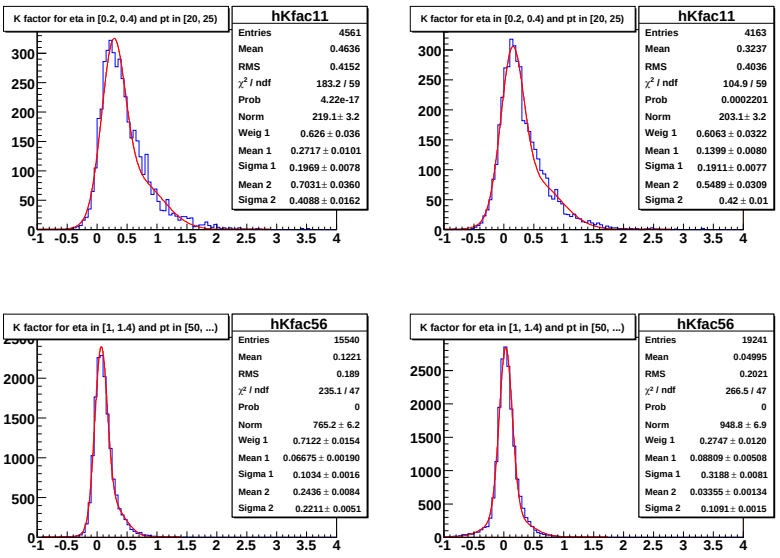

Figure 7.7: Examples of inclusive relative response functions for selected jets in two different $\eta^{jet} \times p_T^{jet,L5}$ bins: left column shows $R = 0.4$, right column $R = 0.7$.

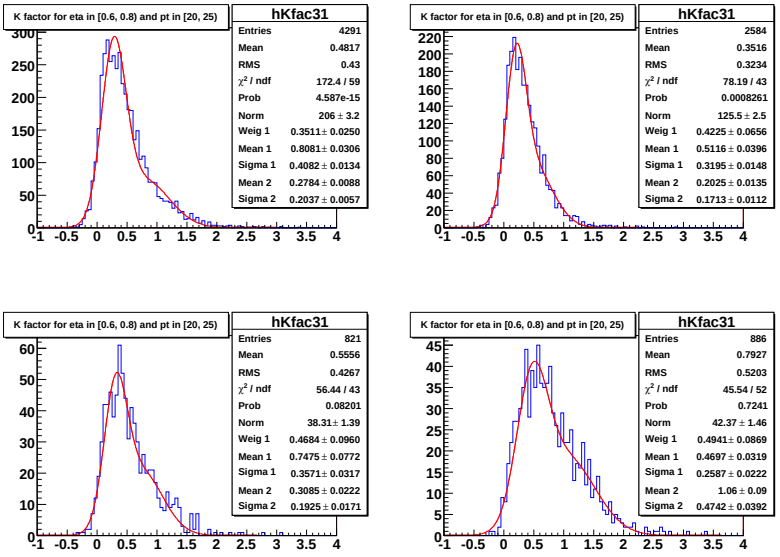

Figure 7.8: Examples of relative response functions for $R = 0.4$ selected jets in a fixed $\eta^{jet} \times p_T^{jet,L5}$ bin: the comparison is among response functions that are inclusive (top, left), limited to hadronic decays (top, right), limited to electron decays (bottom, left) and limited to muon decays (bottom, right).

7.3 Application of the Specific Jet Energy Corrections

Four different jet correction strategies have been considered for exploiting the $\mathcal{K}$-distributions:

1. the "simplest direct" way – each jet is corrected with the average value of the $\mathcal{K}$ distribution $\langle \mathcal{K} \rangle$ of the corresponding bin;

2. the "integral" way – each jet is corrected with the mean value $\bar{\mathcal{K}}$ of the probability density extracted from the fit to (7.4) in the corresponding bin;

$$\begin{aligned} \bar{\mathcal{K}} &= \tfrac{1}{\mathcal{N}} \textstyle\int_{-\infty}^{+\infty} \mathcal{K} \cdot f(\mathcal{K}) \mathrm{d}\mathcal{K} \\ &= \textstyle\int_{-\infty}^{+\infty} \mathcal{K} \cdot (w_N \cdot \mathcal{G}(\mathcal{K}, \mu_N, \sigma_N) + (1 - w_N) \cdot \mathcal{G}(\mathcal{K}, \mu_W, \sigma_W)) \, \mathrm{d}\mathcal{K} \\ &= w_N \cdot \mu_N + (1 - w_N) \cdot \mu_W \end{aligned} \tag{7.5}$$

3. the "random" way – the whole curve from the fit to (7.4) is exploited to extract the information: each jet is corrected with a value taken randomly in the $[-1,4]$ range according to $f(\mathcal{K})/\mathcal{N}$; the random value $\mathcal{K}_R$ is chosen following von Neumann's prescription[(2)] and the random number generator is based on the Mersenne-Twistor one [49];

4. the "most probable value (MPV)" way – each jet is corrected with the most probable value $\mathcal{K}_{MP}$ of the $\mathcal{K}$ distribution of the corresponding bin.

7.4 Test of the Specific Jet Energy Corrections

The specific corrections were tested on the inclusive PYTHIA sample looking at:

- specific jet corrections against L5;
- choice of jet cone radius;
- uncorrect assignment of the non-tagged jet to a b-quark from Z decay;
- unavailability of a good semileptonic decay tagger;
- specific jet correction strategy.

The dijet invariant mass distributions are fitted to a Gaussian in two steps. The first fit runs over the whole range $[0,200]$ GeV while the second fit is limited in the $\mu_0 \pm 2 \cdot \sigma_0$ region determined by the results[(3)] of the first fit. The results of the second fit are used to monitor which way of using the jet corrections is best and which features of the event reconstruction could be improved. The energy scale is given by the mean value μ while the resolution is given by σ/μ.

[(2)] Also known as "acceptance-rejection" method, its description can be found in [1], Section 33.3.
[(3)] μ_0 and σ_0 are the mean value and standard deviation of the Gaussian obtained after the first fit.

The results of the tests are listed in Table 7.1.

The effects of the choice of the cone radius are first explored on jets corrected at L5, together with the effect of the uncorrect assignment of the non-tagged jet to a b-quark. This happens when a gluon jet is selected as a b-jet. To see this effect, the corrections are tested on both the inclusive b-tagged sample ("all svx") and in its subsample where both the selected jets are matched to the b-quarks from Z decay ("right b-jet"). The performace of $R = 0.7$ cones is clearly better in terms of both scale and resolution (18% instead of 20% for $R = 0.4$). One must recall that L5 generic jet corrections bring the calorimeter-level jet to the particle level one, without including the effects of parton showering. The higher energy scale for $R = 0.7$ cones is a predictable effect since such jets are more energetic "by definition", because of a reduced OOC effect and an increased UE contribution. The wrong association of jets to b-quarks leads to non-negligible tails at low mass. The results of this test are shown in Figure 7.9.

Comparing the dijet invariant mass after the specific corrections and after L5 corrections is the next step. The effects of cone radius and of wrong association of jets to b-quarks are also checked. Specific corrections are first used in the "simplest direct" approach without distinguishing among the decays of the b-hadrons because $\langle \mathcal{K} \rangle$ is the extractable parameter which preserves most of information. A significant effect is the gain in energy scale, which is now closer to the Z mass ($= 91.18$ GeV). Further improvements are in resolution and shape of the distribution, which is better fitted by a Gaussian than at L5. However, the low mass tails are still clearly visible in the "all svx" case and the reconstructed dijet mass is not perfectly centered on the Z mass. Other applications of the specific corrections are tried in the attempt to cure these residual problems. The results of this test are shown in Figure 7.10.

Since the $\mathcal{K}$ distributions are asymmetric, particularly for low p_T central jets, and since they are wider for semileptonic b-hadron decays, the possibility of overcorrecting the jets is not remote. To check on this, jets are corrected according to the semileptonic decays of b-hadrons, which are checked at `hepg` level in the same way as the differential corrections are built. In the "right b-jet" case the best resolution (13%) is obtained, which can be taken as the limit of the dijet mass resolution that can ever be achieved in a calorimetric measurement of jet energy which makes no use of tracking information and is combined with the described correction procedure. The improvement in energy scale is 1 GeV. The results of this test are shown in Figure 7.11.

Since a first attempt to use the "MPV" approach produces a wrong Z mass by about 10 GeV, the method is rejected. The final check is focussed on the "integral" and "random" ways in the realistic case of possible wrong association of jets to b-quarks and corresponding to the current unavailability of a good semileptonic decay tagger. The "integral" method is comparable to the "simplest direct" one in terms of resolution while it leads to a slightly better mass scale, only by 2.2 GeV away from the Z mass. The best result in terms of mass scale is obtained with the "random" method, which exploits the full distribution including the tails. This is to be confronted with the resolution, which is the most important parameter and which is the worst among all. The

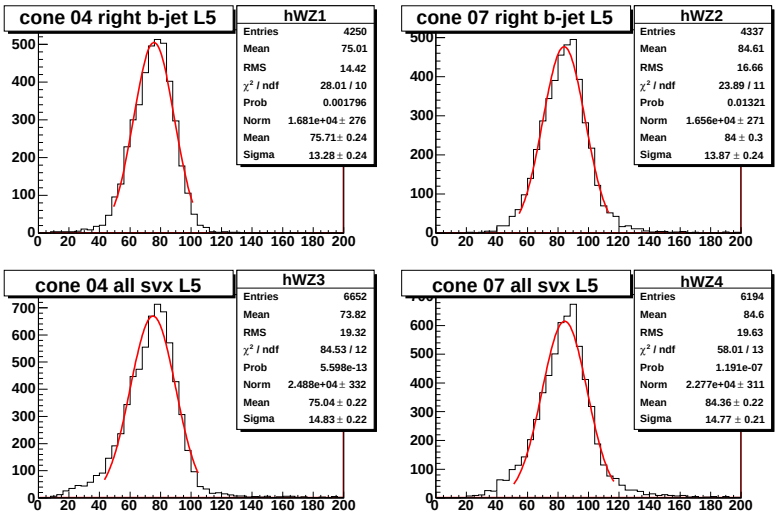

Figure 7.9: Test of the effects of the choice of cone radius (left: $R = 0.4$, right: $R = 0.7$) on the dijet invariant mass at L5 generic jet energy corrections. The effect of the correct b-to-jet association on the tails is evident (top: only correct association, bottom: inclusive).

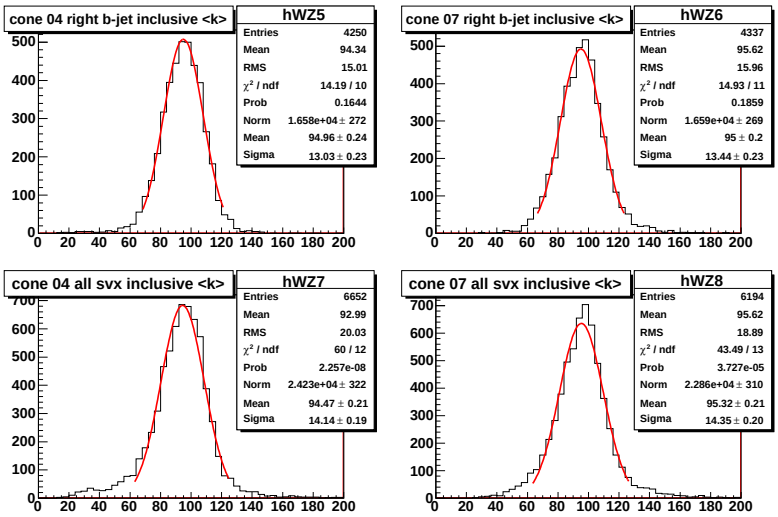

Figure 7.10: Test of the effects of the choice of cone radius (left: $R = 0.4$, right: $R = 0.7$) on the dijet invariant mass corrected with inclusive specific jet energy corrections used in the "simplest direct" way. The effect of the correct b-to-jet association on the tails is evident (top: only correct association, bottom: inclusive).

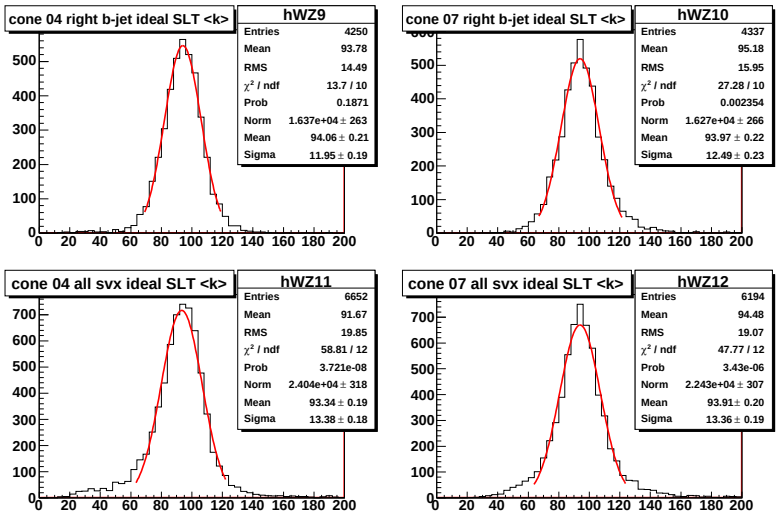

Figure 7.11: Test of the possible effects of an ideal tagger of b-hadrons decays on the dijet invariant mass corrected with specific jet energy corrections used in the "simplest direct" way. The effects of the correct b-to-jet association (top: only correct association, bottom: inclusive) and of the cone radius (left: $R=0.4$, right: $R=0.7$) are shown too.

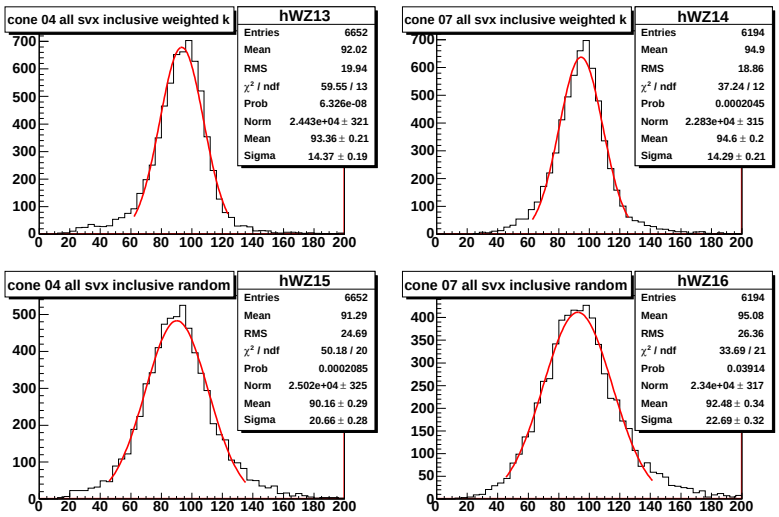

Figure 7.12: Test of the effects of using the results of the parametrization of the response function on the dijet invariant. The effect of cone radius is shown too (left: $R=0.4$, right: $R=0.7$).

R	b-to-jet	correction	usage	mean value (GeV)	resolution
0.4	correct	L5		75.7	0.18
0.7	correct	L5		84.0	0.17
0.4		L5		75.0	0.20
0.7		L5		84.4	0.18
0.4	correct	inclusive	simplest	95.0	0.14
0.7	correct	inclusive	simplest	95.0	0.14
0.4		inclusive	simplest	94.5	0.15
0.7		inclusive	simplest	95.3	0.15
0.4	correct	differential	simplest	94.1	0.13
0.7	correct	differential	simplest	94.0	0.13
0.4		differential	simplest	93.3	0.14
0.7		differential	simplest	93.9	0.14
0.4		inclusive	integral	93.4	0.15
0.7		inclusive	integral	94.6	0.15
0.4		inclusive	random	90.2	0.23
0.7		inclusive	random	92.5	0.25

Table 7.1: Summary of the tests of the specific jet energy corrections: the "b-to-jet" column refers to the correct parton-to-jet assignment, the "correction" and "usage" columns refer to the level of correction (L5 or specific) and to the application of the specific correction.

results of this test are shown in Figure 7.12.

7.5 Final Choice and Improvable Aspects

Since after the specific corrections no particular difference is found between $R = 0.4$ and $R = 0.7$ cones, $R = 0.4$ cones are chosen, as anticipated in Chapter 6. The best compromise between a good energy scale and a good resolution, within the realistic options which take into account the currently available reconstruction tools at CDF, is found for the "integral" approach (Figure 7.12, top left), which is therefore adopted throughout this work.

The Z mass window is defined as $[79.0, 122.2]$ GeV, or rather $[\mu - \sigma, \mu + 2\sigma]$, where μ and σ are the results of the fit to a Gaussian of the dijet invariant in the WZ MC, after jets are corrected with the chosen strategy. This asymmetric window, even if not exactly centered on the Z-peak, is chosen because the main backgrounds show a fast decreasing dependence on dijet invariant mass, so that such a choice can improve the S/B ratio, as in Figure 7.13.

This preliminary study leaves some open questions:

- the selection of candidate b-jets is not optimal, the jet-to-parton association must be improved to reduce the tails in the dijet invariant mass distribution;

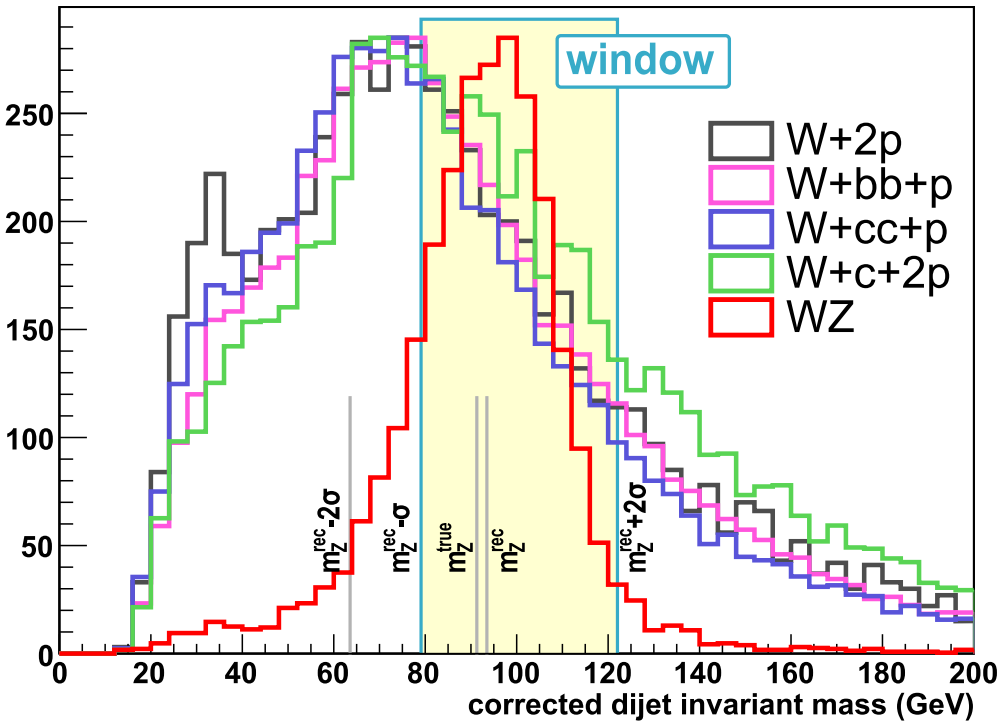

Figure 7.13: Comparison of the dijet invariant mass distributions for the signal and some processes contributing to W+multijet production in order to define an asymmetric dijet invariant mass window. The distributions are normalized to the same maximum value and include only b-tagged events.

- b-jets associated to semileptonic decays of b-hadrons show in average a greater response, a reliable tagger is needed to apply the appropriate correction;
- different constructions and applications of the corrections may be explored to get narrower and easier to exploit correction factor distributions in order to get the correct Z-peak.

8. Background Estimate with "Method 2"

To perform the measurement one needs to determine the sample composition in terms of signal and background events. The method described in this chapter is valid for all the selected lepton types. The known backgrounds for the process $p\bar{p} \to WZ + X \to \ell\nu$+2 jets can be divided into three categories:

- absolute backgrounds: EW processes of either theoretically well-known or measured cross section
- non-W QCD background: QCD production associated to a hadron faking the lepton and $\not\!\!E_T$, altogether faking the W;
- W+jets background: production of a W boson associated to hadron jets.

8.1 Overview of the Method

The so-called "method 2" background determination technique was developed for the first time by the CDF collaboration at the end of Run I and has been implemented in a number of slightly different ways during the years [50]. Depending on the analysis, it is used rather than "method 1", where rates of background processes are measured in kinematically close data control regions and extrapolated to the signal region. "Method 1" is used in measurements making use of SLT or in all-hadronic final states. "Method 2" combines both MC-based and data-driven estimates in order to evaluate separately the contribution of the different physical processes to the composition of the lepton+jets sample. The core of its philosophy is the data-driven normalization of the W+jets backgrounds, whose predicted cross section can remarkably change when the perturbatve calculation is extended to higher orders. The renormalization of the backgrounds, and therefore of the signal, is performed on pretagged events (indicated by N) while the number of tagged events M is used, together with the tagging efficiencies, to constrain the background composition:

$$\left.\begin{aligned} \mathcal{N}_{WZ} + \textstyle\sum_{EW} N_{EW} + \mathcal{N}_W &= N_{data} \cdot (1 - \mathcal{F}_{QCD}) \\ \mathcal{N}_{WZ} \cdot \varepsilon_{WZ} + \textstyle\sum_{EW} (N_{EW} \cdot \varepsilon_{EW}) + \mathcal{N}_W \cdot \varepsilon_W &= M_{data} - M_{QCD} \end{aligned}\right\} \tag{8.1}$$

In (8.1), $\mathcal{N}$ is a non-fixed component of the sample (either signal or W+jets) and ε_i are the tagging efficiencies. The treatment of the W+jets backgrounds and the determination of the non-W QCD fraction $\mathcal{F}_{QCD}$ are explained in Sections 8.4 and 8.3 respectively.

Process	Cross Section (pb)	
WW	12.4 ± 0.25	Theoretical
ZZ	1.58 ± 0.05	Theoretical
$Z \to \tau\tau$	265 ± 30	Measured
$t\bar{t}$	8.2 ± 1.1	Measured
single t, s-ch.	0.88 ± 0.05	Theoretical
single t, t-ch.	1.98 ± 0.08	Theoretical

Table 8.1: Cross sections used to scale EW backgrounds. The single t cross sections must be rescaled by a factor of $1/3$ because in the MC generated events the W was forced to decay into lepton-neutrino pairs.

The tagging efficiencies are obtained from large samples of PYTHIA (integrated with ALPGEN for W+jets and Z+jets $\to \tau\tau$+jets samples or MadEvent for single top samples) events. However, the definition of tagging efficiency in this case is not straightforward. While in $t\bar{t}$ studies ε_i refers to b-tagging, here tagged events are further required to show a dijet invariant mass in the Z mass window, which is defined in Section 7.5. This choice is made because the specific jet energy corrections correct only b-jets by construction and the identification of b-jets with SECVTX is performed with high confidence. By the point of view of the specific jet energy corrections, all tagged events are treated as if they were events with two b-jets and both jets are corrected accordingly. From now on the definition of tagged event will include the condition of the two selected jets being in the Z mass window. The tagging efficiency[(1)] for each process is then defined as

$$\varepsilon = \frac{M}{N} \cdot \frac{M_{m_{jj}}}{M} \cdot \Phi_T = \varepsilon_{MC}^{tag} \cdot \varepsilon_{MC}^{m_{jj}} \cdot \Phi_T \quad , \tag{8.2}$$

where Φ_T is the SECVTX scale factor described in Section 5.3. Moreover, except when describing the calibration of Heavy Flavor Fractions in QCD data, the number of tagged events with dijet invariant mass in the Z window $M_{m_{jj}}$ will be marked as M for sake of simplicity. This background estimate method was found to work well in $t\bar{t}$ cross section measurements [46] [47], but has never been tried in diboson studies so far.

8.2 Absolute EW Backgrounds

The WZ production signature can be reproduced by many EW processes which have well-known theoretical (or measured) cross section and can be b-tagged too. The main sources of such backgrounds are:

- WW production, with one W decaying leptonically and the other one into a jet pair which is mistagged (mistags are easier in c-flavored jets);
- ZZ production, with one Z decaying to leptons, one of whom is missed or misidentified;

[(1)] ε_W is defined differently from (8.2), as in Section 8.3.

scale factor	avail. information	lacking information	chosen solution
CEM $\varepsilon_{L2,3}$	curve paramet.	σ of parameters	$\sigma_{\varepsilon_{L2,3}}/\varepsilon_{L2,3} = 5\%$
MET $\varepsilon_{L1,3}$	curve paramet.	σ of parameters	$\sigma_{\varepsilon_{L1,3}}/\varepsilon_{L1,3} = 5\%$
MET $\varepsilon_{L1,3}$ 0i/9	none		$\varepsilon_{L1,3}$ = the same as 0i/8
PEM $\varepsilon_{L2,3}$ 0i/9	none		$\varepsilon_{L2,3}$ = the same as 0i/8
CMX ε_{L2}	none		$\varepsilon_{L2} = 1.0 \pm 0.2$
BMU $\varepsilon_{L1,2,3}$	none		$\varepsilon_{L1+L2+L3} = 1.0 \pm 0.2$
BMU S_ℓ	very detailed information and large amount of different subcases		average value, greater σ: $S_{\mathrm{BMU}} = 1.06 \pm 0.03$

Table 8.2: Solutions chosen in order to bypass the missing information on trigger efficiencies and lepton ID scale factors.

	$\mathcal{A}$ for different lepton types				
process	CEM	PHX	CMUP	CMX	BMU
WZ	0.8143 ± 0.0059	0.3273 ± 0.0038	0.4401 ± 0.0044	0.2744 ± 0.0034	0.2484 ± 0.0033
WW	1.7311 ± 0.0088	0.5546 ± 0.0049	0.8903 ± 0.0063	0.5017 ± 0.0047	0.4146 ± 0.0043
ZZ	0.0356 ± 0.0012	0.0109 ± 0.0007	0.0512 ± 0.0015	0.0323 ± 0.0012	0.0290 ± 0.0011
$t\bar{t}$	0.3732 ± 0.0028	0.0707 ± 0.0012	0.2089 ± 0.0021	0.1015 ± 0.0015	0.0674 ± 0.0012
single t (s)	4.022 ± 0.021	0.7749 ± 0.0092	2.167 ± 0.016	1.067 ± 0.011	0.7290 ± 0.0089
single t (t)	4.066 ± 0.022	0.8086 ± 0.0095	2.152 ± 0.016	1.077 ± 0.011	0.7669 ± 0.0092
$Z \to \tau\tau$	0.0331 ± 0.0004	0.0113 ± 0.0003	0.0157 ± 0.0003	0.0093 ± 0.0002	0.0086 ± 0.0002

Table 8.3: Acceptance from MC simulations for signal and EW backgrounds. All numbers are expressed in %, trigger efficiency and lepton ID scale factors are included, uncertainty is statistical only.

- Z+jets production[(2)], with $Z \to \tau^+\tau^- \to \ell\nu$+ hadrons, with a SECVTX tag on the $\tau \to$ 3-prong decay;
- $t\bar{t}$ production, where jets are merged (in the single lepton final state) or one lepton is missed by the tracker or is misidentified (in the dilepton final state);
- single top production, both in the s and t channels.

The absolute EW background estimate is purely MC-driven and the expected number of pretagged events for each process is given by the cross section and the acceptance $\mathcal{A}_{EW}$:

$$N_{EW} = \int \mathcal{L}\mathrm{d}t \cdot \sigma_{EW} \cdot \mathcal{A}_{EW} \quad . \tag{8.3}$$

The cross sections used for this analysis are listed in Table 8.1. The acceptance $\mathcal{A}_{EW}$ cannot be defined simply as the ratio between the number of pretagged events and the number of generated events N_{MC}/N_{gen}, because the effect of trigger efficiency and lepton identification is different

[(2)] Even if the cross section of this process is subject to the same theoretical uncertainties as W+jets, its small acceptance allows treating it as an EW background.

process	$\varepsilon_{MC}^{tag} \cdot \varepsilon_{MC}^{m_{jj}}$
WZ	8.70 ± 0.12
WW	2.64 ± 0.05
ZZ	7.39 ± 0.41
$t\bar{t}$	15.65 ± 0.18
single t (s)	17.24 ± 0.13
single t (t)	10.38 ± 0.18
$Z \to \tau\tau$	0.15 ± 0.05

Table 8.4: Combined efficiency of b-tagging and cut on dijet invariant mass after specific jet energy corrections from MC simulations for signal and EW backgrounds. All numbers are expressed in % and must be rescaled by Φ_T (uncertainty does not include contribution by Φ_T).

from MC to data [51]. Each trigger used had its data/MC efficiency ratio computed and the same was done for the lepton identification scale factors. These numbers depend on the data acquisition period and on the kinematics of the event. The electron triggers in particular are rather sensitive to the raw measured E_T of the EM cluster. The scale factor of each event is the product of the measured trigger efficiency (of each of the three trigger levels when such an information was available) and the lepton ID scale factor: $S_i = S_\ell \cdot \prod_{j=1}^{3} \varepsilon_{Lj}$. The sum of the individual scale factors of each event was accordingly replaced to N_{PT}:

$$\mathcal{A}_{EW} = \frac{\sum_{i=1}^{N_{MC}} S_i}{N_{gen}} = \frac{N_{MC}^{scaled}}{N_{gen}} \quad . \tag{8.4}$$

The propagated uncertainty on the event scale factors is saved as a source of systematic uncertainty in the measurement. The information about the latest periods of data taking and some of the triggers is not always complete. Different solutions are adopted for the different problems, as listed in Table 8.2. If the efficiency relative to some trigger level is quoted as "100%", it has been assumed errorless. The combined efficiency of b-tagging and dijet invariant mass cut after specific jet energy corrections are computed with respect to non-rescaled pretagged events and are inclusive of lepton type. This can be done because jet selection is independent from lepton selection. The acceptances and efficiencies of combined b-tagging and dijet invariant mass cut are listed in Table 8.3 and Table 8.4 respectively.

8.3 W+Jets Background

The core of the "method 2" background calculation is the determination of the flavor composition of QCD jets associated to a W boson. The W+jets background is expected to be the main one, since the inclusive cross section measured by CDF in Run II [52] is

$$\sigma(p\bar{p} \to W^{\pm} + X) \cdot B(W \to \ell\nu) = 2775 \pm 10\ (\text{stat}) \pm 53\ (\text{syst}) \pm 167\ (\text{lumin})\ \text{pb} \quad ,$$

to be compared to the NLO calculation based on van Neerven's work [53] of 2687 ± 54 pb. The main assumptions of the procedure described in the this section is that the fraction of W+jets events containing a real heavy flavor hadron are more stable than the absolute cross sections at higher order of perturbative calculation. These are called the Heavy Flavor Fractions (HFFs or $\mathcal{F}_{HF}$). Then the W+jets contribution is obtained then as:

$$\left.\begin{aligned} \mathcal{N}_W &= N_{data} \cdot (1 - \mathcal{F}_{QCD}) - \mathcal{N}_{WZ} - \textstyle\sum_{EW} N_{EW} \\ \mathcal{M}_W &= \mathcal{N}_W \cdot (\textstyle\sum_{HF} \mathcal{F}_{HF} \cdot \varepsilon_{HF} + (1 - \textstyle\sum_{HF} \mathcal{F}_{HF}) \cdot \varepsilon_{LF}) \end{aligned}\right\} \tag{8.5}$$

• Determination of the Heavy Flavor Fractions in the W+2 Jets Sample

The determination of the HFFs is based on leading order ALPGEN MC samples, interfaced to PYTHIA, and is obtained by combining four processes:

- W in association to 0/1/2/3/4 light quarks;
- $W + b\bar{b}$ in association to 0/1/2 light quarks;
- $W + c\bar{c}$ in association to 0/1/2 light quarks;
- $W + c$ (or $W + \bar{c}$) in association to 0/1/2/3 light quarks.

Since these MC samples are generated forcing the W to decay into one generation of $\ell\nu$ pairs, a total number of 45 different MC datasets are used, allowing for $W \to \tau\nu_\tau$ contamination. As stated in Section 4.4, jets are user-defined and the detector level configuration can be strongly influenced by gluon radiation or jet overlap. Therefore also events with many, or none, generated quarks at the Matrix Element (ME) level can pass the event selection. Moreover, additional jets, either with or without heavy flavor content, can be produced during Parton Showering (PS) and therefore events from different MC samples may end up in the same region of phase space. This overlap must be removed to avoid double counting.

The measurement of HFFs is performed on pretagged events. The removal of "overlap events" is based on detector-level jets, since the separation of the quarks in HF pairs are quite remarkably different from ME and PS production. Using a "figurative" approach, one can say that HF quark pairs from ME generate two different jets, while those from PS end up into the same jet. These consideration are translated into practice by trying to match each HF quark in the `hepg` bank to the two selected jets, with the usual $\Delta R_{q,jet}$ criterion. The event is removed if both the ME HF quarks are matched to the same jet or if the PS HF quarks are not matched to the same jet. In this case the problem described in Section 7.2 did not arise because the quarks marked as ME quarks or PS quarks occur only once in the decay tree. The non-vetoed events are called "unique pretagged events". Four kinds of HFFs are defined:

- $\mathcal{F}_{1B}$ – events with only 1 jet containing a real b-hadron;
- $\mathcal{F}_{2B}$ – events with both selected jets containing a real b-hadron;

- $\mathcal{F}_{1C}$ – events with only 1 jet containing a real c-hadron;
- $\mathcal{F}_{2C}$ – events with both selected jets containing a real c-hadron.

In each unique pretagged event, the matching procedure is repeated for all the stable HF hadrons of the decay tree, contained in a dedicated bank. The number of jets matched to a b- or c-hadron is counted. The jet is checked for a match to a c-hadron only if the attempt to match it to a b-hadron failed, and the total sum of matched events N_{HF} is obtained, for each $HF = 1B,\ 2B,\ 1C,\ 2C$.

The final step in the measurement of HFFs is the weighting procedure to extract the combined information from all the 45 MC datasets. Each event is weighted according to its individual cross section

$$w = \frac{\sigma_{ALP}}{N_{GRL}} \ , \tag{8.6}$$

where σ_{ALP} is the LO cross section computed by ALPGEN and N_{GRL} is the number of events in the MC sample that pass the requirements of the Good Run List and which have the primary vertex in the $|z| < 60$ cm fiducial region. The HFFs are therefore defined as:

$$\mathcal{F}_{HF} = \frac{\langle N_{HF} \rangle}{\langle N_{unique} \rangle} = \frac{\sum_{i=1}^{45} w^i N^i_{HF} / \sum_{i=1}^{45} w^i}{\sum_{i=1}^{45} w^i N^i_{unique} / \sum_{i=1}^{45} w^i} = \frac{\sum_{i=1}^{45} w^i N^i_{HF}}{\sum_{i=1}^{45} w^i N^i_{unique}} \ . \tag{8.7}$$

The combined efficiencies of b-tagging and cut in dijet invariant mass are calculated by weighting the 45 MC datasets according to the definition of $\mathcal{F}_{HF}$:

$$\varepsilon_{HF} = \Phi_T \cdot \frac{\langle M_{HF} \rangle}{\langle N_{HF} \rangle} = \Phi_T \cdot \frac{\sum_{i=1}^{45} w^i M^i_{HF}}{\sum_{i=1}^{45} w^i N^i_{HF}} \ . \tag{8.8}$$

The results of the calculation of $\mathcal{F}_{HF}$ and ε_{HF} are listed in Table 8.5. Since no remarkable difference is found bewteen events with a selected high p_T electron or muon, the inclusive result is taken.

• Calibration of Heavy Flavor Fractions

The predicted heavy flavor content of jets must be corrected for known problems of MC simulations. Since W+multijet tagged events are too few to perform a good comparison of data against ALPGEN, this MC-to-data correction is obtained from a large sample of inclusive QCD data [54]. The heavy flavor fractions are rescaled by a calibration factor defined as:

$$\mathbb{K}_{HF} = \frac{\mathcal{F}^{data}_{HF}}{\mathcal{F}^{MC}_{HF}} \ , \tag{8.9}$$

with $\mathcal{F}_{HF}$ defined as the fraction of events with a real content of heavy flavor hadrons in selected jets. By assuming that the calibration factor $\mathbb{K}_{HF}$ is the same for events as for jets, one

$\mathcal{F}_{HF}$	electron	muon	inclusive
$1B$	0.866 ± 0.011	0.894 ± 0.015	0.878 ± 0.009
$2B$	0.508 ± 0.005	0.519 ± 0.005	0.513 ± 0.004
$1C$	11.797 ± 0.055	11.751 ± 0.064	11.778 ± 0.041
$2C$	1.473 ± 0.014	1.438 ± 0.014	1.458 ± 0.010
ε_{HF}	electron	muon	inclusive
$1B$	7.12 ± 0.22	7.49 ± 0.38	7.28 ± 0.21
$2B$	10.60 ± 0.17	10.22 ± 0.19	10.44 ± 0.13
$1C$	1.90 ± 0.05	1.86 ± 0.05	1.88 ± 0.03
$2C$	2.44 ± 0.12	2.45 ± 0.13	2.45 ± 0.09

Table 8.5: Raw HHFs (top) and combined efficiency of b-tagging and cut on dijet invariant mass after specific jet energy corrections (bottom) after the merging of MC simulations for $W+$multiparton production. All numbers are expressed in %, uncertainty is statistical only, efficiencies must be rescaled by Φ_T.

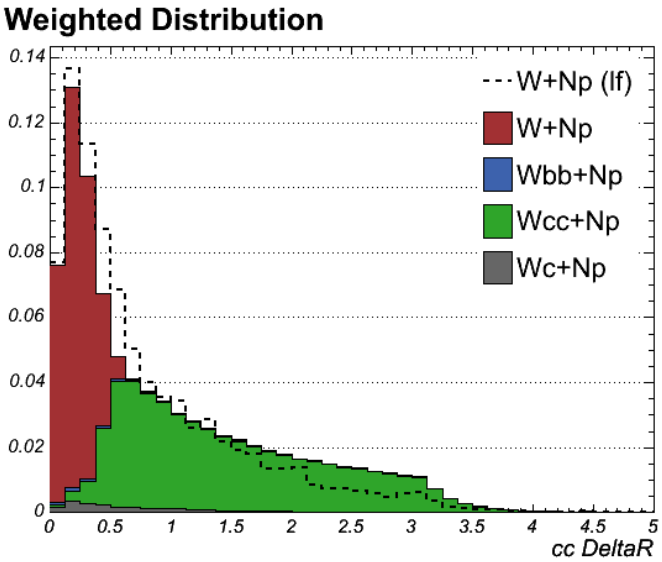

Figure 8.1: Distributions of ΔR between charm pairs from the dedicated ALPGEN samples (colored histogram) and from PYTHIA showers (dashed line), for pairs of $p_T > 20$ GeV; ALPGEN samples are combined together according to the overlap removal procedure described in the text.

can write, specializing to the case $HF = 1B,\ 2B$,

$$\left.\begin{aligned} \mathcal{F}_B^{data} &= \frac{N_B^{data}}{N^{data}} = \frac{M^{data}}{\varepsilon_{data}^{tag} \cdot N^{data}} \\ \mathcal{F}_B^{MC} &= \frac{N_B^{MC}}{N^{MC}} = \frac{M^{MC}}{\varepsilon_{MC}^{tag} \cdot N^{MC}} \end{aligned}\right\} \tag{8.10}$$

and therefore rewrite Eq. (8.9) as:

$$\mathbb{K}_B = \frac{\mathcal{F}_{jet,tag}^{data} \cdot \mathcal{F}_{B,tag}^{data}}{\mathcal{F}_{B,tag}^{MC} \cdot \Phi_T} \ , \tag{8.11}$$

where $\mathcal{F}_{jet,tag}^{data}$ is the fraction of SECVTX tagged jets in data, $\mathcal{F}_{B,tag}^{data}$ is the fraction of SECVTX tagged b-jets in data and $\mathcal{F}_{B,tag}^{MC}$ is the fraction of SECVTX tagged b-jets in ALPGEN events. Equivalent definitions apply for $HF = 1C,\ 2C$. The extraction of $\mathcal{F}_{B,tag}^{data}$ is performed by a fit to template distributions of some variable sensitive to the heavy flavor content of the jet whose shape is determined from MC samples. A larger $\mathbb{K}_{HF}$ than unity can be expected as a consequence of incorrect gluon splitting modeling in ALPGEN and higher order effects. The chosen variables in the measurement described in [54] are:

- positive excess of vertex mass m_{vtx} (the sign of the vertex mass is given by the sign of the SECVTX tag);
- pseudo-$c\tau$, defined as $L_{xy} \cdot m_{vtx}/p_T^{vtx}$, with L_{xy} defined as in Section 5.3.

MC samples are similar to those used for determining $\mathcal{F}_{HF}$, with the only difference being the absence of the W. Data are selected from an inclusive jet trigger stream where at least one jet has $E_T > 50$ GeV. Jets are corrected at L5 of generic corrections and are further required to have $E_T > 20$ GeV and $|\eta| < 2$ with one jet having $E_T > 70$ GeV to avoid the trigger turn on region.

This kind of measurement is rather long and complex and its results would be applicable to the measurement of WZ production cross section only if the jet selections were the same. This is not the case. According to the definitions of [54], jet counting in the measurement of $\mathbb{K}_{HF}$ takes into consideration only jets with $E_T > 20$ GeV and $|\eta| < 2$. The jet sample used in this WZ study is therefore composed of subsamples of the 0-, 1- and 2-jets bins. The results of the measurement of $\mathbb{K}_{HF}$ are listed for sake of completeness in Table 8.6, but cannot be used at face value for this work which will require further dedicated studies. The final result quoted by the authors of [54] is $\mathbb{K}_B = \mathbb{K}_C = 1.0 \pm 0.3$ which "conservatively covers the range of results". However at low jet multiplicity a higher value could be expected[(3)]. Moreover, the impact of $\mathbb{K}_{HF}$ on the measurement is expected to be large in the WZ cross section measurement because the W+jets background is orders of magnitudes greater than the signal and the parameters of the second equation of (8.1) can change a lot even for small steps in $\mathbb{K}_{HF}$. As a consequence, for the time being, the results included in this document are presented for both a set of different possible values of $\mathbb{K}_{HF}$ and for $\mathbb{K}_{HF} = 1.0 \pm 0.3$, which is taken as a reference value.

[(3)] One must recall that the described measurement of $\mathbb{K}_{HF}$ was performed as part of a measurement of the $t\bar{t}$ production cross section, which defines the "$\geqslant$ 3-jets bin" as the signal region.

HF	variable	leading	1-jet	2-jets	3-jets	4-jets	all
B	m_{vtx}	no	1.24 ± 0.10	0.94 ± 0.09	1.08 ± 0.15	0.80 ± 0.28	0.98 ± 0.07
B	$c\tau$	no	1.63 ± 0.10	1.12 ± 0.10	0.99 ± 0.18	1.10 ± 0.37	1.17 ± 0.08
C	m_{vtx}	no	1.26 ± 0.28	0.84 ± 0.21	1.04 ± 0.39	1.37 ± 0.87	1.24 ± 0.18
C	$c\tau$	no	1.23 ± 0.12	0.97 ± 0.15	0.67 ± 0.28	0.48 ± 0.52	1.19 ± 0.10
B	m_{vtx}	yes	1.60 ± 0.35	1.17 ± 0.08	1.05 ± 0.08	0.95 ± 0.13	1.09 ± 0.06
B	$c\tau$	yes	1.63 ± 0.97	1.60 ± 0.09	1.22 ± 0.10	1.11 ± 0.16	1.17 ± 0.07
C	m_{vtx}	yes	2.39 ± 0.74	1.38 ± 0.18	1.12 ± 0.22	1.13 ± 0.38	1.20 ± 0.14
C	$c\tau$	yes	3.70 ± 2.50	1.26 ± 0.12	0.88 ± 0.13	0.90 ± 0.24	1.17 ± 0.09

Table 8.6: Results of $\mathbb{K}_{HF}$ described in [54] for the tight SECVTX tagger: the column "leading" refers to the usage of the leading jet of the event in the measurement.

• Determination of the Mistag Rate in the W+Light Flavor Jets Sample

The rate at which jets without a real heavy flavor content are tagged as *b*-jets ("fake rate") is an important figure of merit for any *b*-tagger. Such mistags are due to the finite detector resolution leading to secondary vertices from mis-measured prompt tracks or from fake tracks, to interactions of the produced particles with the detector and to real secondary vertices from long-lived light flavor hadrons such as K_L or Λ. The effect of finite detector resolution can be assumed to cause equally positive and negative tags and a rough estimate of the mistags can be given by the number of negative tags which are of unphysical meaning. In a number of CDF studies the heavy flavor positive tag rate is found to be modeled in simulations with an accuracy up to 5%, while the negative tag rate is at least 30% off. The solution chosen is the so-called "mistag matrix".

The "mistag matrix" is a multi-dimensional parametrization of the tag rate in generic jets[(4)] in terms of the following variables:

- uncorrected jet energy;
- jet pseudorapidity;
- number of tracks associated to the jet;
- number of vertices in the event;
- z coordinate of the primary vertex of the events;
- scalar sum of the transverse energy of the event.

The mistag matrix parametrization allows to compute a tagging probability for both positive and negative tags. This prediction needs corrections to account for the presence of some heavy flavor jets in generic jets, for the effects of interactions in the detector material and for the nearly

[(4)]Data collected by triggering only on jets with different thresholds.

prompt decay of long-lived light flavor hadrons. If thinking in terms of events, the mistag probability of all jets in the events must be properly combined.

Since the application of the mistag matrix and the cut in dijet invariant mass are independent on each other, to easy the work the mistag matrix prediction is traced only over events with the dijet invariant mass in the Z window after specific jet energy corrections[5]. The W+light flavor tagging efficiency is given by the ratio between the predicted number of mistagged events $\not{M}$ (shown in Table 9.1) and the total number of pretagged events:

$$\varepsilon_{LF} = \frac{\not{M}}{N} \ . \tag{8.12}$$

Since this procedure is purely data-driven, the scale factor Φ_T is not applied.

8.4 Non-W QCD Background

The processes listed so far dealt with the expected backgrounds in a b-tagged "lepton+jets" sample. Additional background sources are QCD jet production where the W is faked by a fake lepton and $\not\!\!E_T$ of QCD or mismeasurement origin. In leptonic W decays the charged lepton is well isolated (Section 6.1) and the energetic neutrino leads to large $\not\!\!E_T$. These conditions define the signal region. The estimate of the number of non-W QCD events in the signal region is mainly data driven and is based on the assumption that lepton isolation and $\not\!\!E_T$ are uncorrelated in QCD processes without real W production.

The technique used in this analysis is the so-called "standard Isolation versus $\not\!\!E_T$ plot". The Isolation$\times\not\!\!E_T$ plane is divided into four regions:

- region "A": $\not\!\!E_T < 15$ GeV and Isolation> 0.2;
- region "B": $\not\!\!E_T < 15$ GeV and Isolation$\leqslant 0.1$;
- region "C": $\not\!\!E_T \geqslant 20$ GeV and Isolation> 0.2;
- region "D" (signal region): $\not\!\!E_T \geqslant 20$ GeV and Isolation$\leqslant 0.1$.

The borders of sideband regions (those defined by the strict inequalities) are chosen in order to keep the sideband regions and the signal region well separate from each other. However, these borders are arbitrarily defined and this arbitrariness is source of systematic uncertainty. According

[5] What stated about the correct order of applying the b-tagging and the specific jet energy corrections can be made more precise. The jets are corrected according to the specific corrections in all events but the information on the corrected dijet invariant mass is used only to build the mistag matrix prediction and to count the number of events satisfying the $Z \to b\bar{b}$ selection.

	CEM	PHX	CMUP	CMX	BMU
$\mathcal{F}_{QCD}^{raw}$	7.297	48.05	2.336	2.980	3.40
$\mathcal{F}_{QCD}^{corr}$	6.250	45.07	1.515	2.089	0.24
$\sigma_{\mathcal{F}_{QCD}}$ (stat)	0.069	0.69	0.044	0.071	0.18
$\sigma_{\mathcal{F}_{QCD}}$ (syst)	0.822	13.44	0.588	0.525	0.53
ε_{QCD}	0.655	0.642	0.662	0.572	1.53
$\sigma_{\varepsilon_{QCD}}$	0.046	0.044	0.026	0.015	0.59

Table 8.7: Non-W QCD fraction before and after correcting for signal, EW background and $W+$ multijet expectations and combined efficiency of b-tagging and cut in dijet invariant mass after specific jet energy corrections in non-W events for the different lepton types. All numbers are expressed in %.

to the above assumption, the following proportion can be used to estimate the number of QCD events in the signal region:

$$\frac{N_{QCD}^{A}}{N_{QCD}^{B}} = \frac{N_{QCD}^{C}}{N_{QCD}^{D}} \quad . \tag{8.13}$$

To a first approximation sideband events can be thought to be purely QCD events. However, particularly for region "B", this is not precise. Each event counting in the sideband regions is therefore corrected for the contribution of other processes as:

$$N_{QCD}^{sb} = N^{sb} - N_{WZ}^{sb} - \sum_{EW} N_{EW}^{sb} - N_{W}^{sb} \quad , \tag{8.14}$$

for each sideband region $sb = A,\ B,\ C$. The QCD fraction of events in the signal region $\mathcal{F}_{QCD}$ is then obtained as:

$$\mathcal{F}_{QCD} = \frac{N_{QCD}^{A}}{N_{QCD}^{C}} \cdot \frac{N_{QCD}^{B}}{N^{D}} \quad . \tag{8.15}$$

Since the non-W background estimate depends on the required fake lapton properties, it must be made separately by lepton type. The main uncertainty on $\mathcal{F}_{QCD}$ is given by the arbitrariness of the choice of the sideband region borders. This uncertainty is estimated by varying the borders of 0.1 in lepton isolation and by 5 GeV in $\not\!\!E_T$ and taken as half of the maximum dispersion of the obtained values. The effect is assumed to be the same for both the raw and the corrected $\mathcal{F}_{QCD}$, and to be conservative the uncertainty on corrected fraction is assumed to be the same as for the raw one.

The combined efficiency of b-tagging and cut in dijet invariant mass is assumed to be the same as in region "B". In this case, since the non-W background depends on the lepton type, the efficiency is different for the different lepton types and it does not need to be rescaled by Φ_T because the procedure is completely data-driven:

$$M_{QCD} = N_{QCD} \cdot \varepsilon_{QCD} = N_{data} \cdot \mathcal{F}_{QCD}^{corr} \cdot \frac{M_{data}^{B}}{N_{data}^{B}} \quad . \tag{8.16}$$

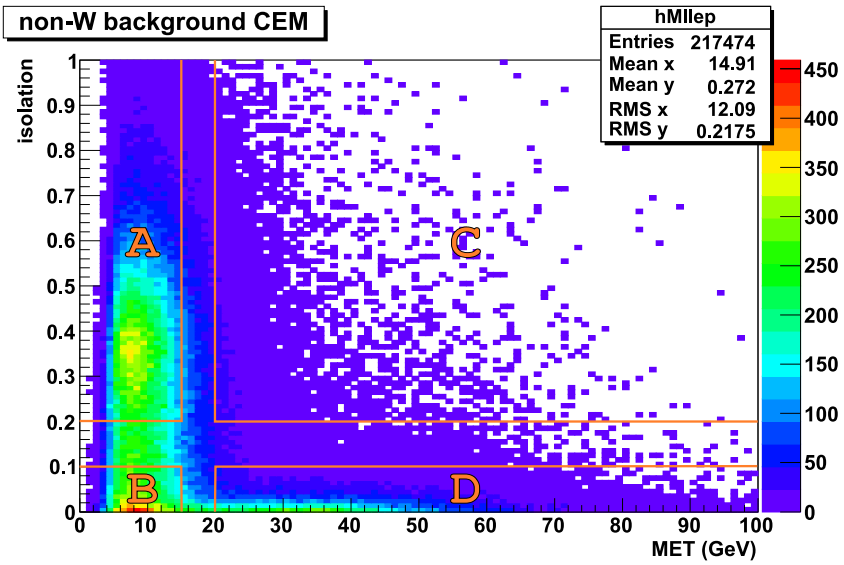

Figure 8.2: Isolation versus $\not\!\!E_T$ plot to estimate the non-W QCD background in CEM events.

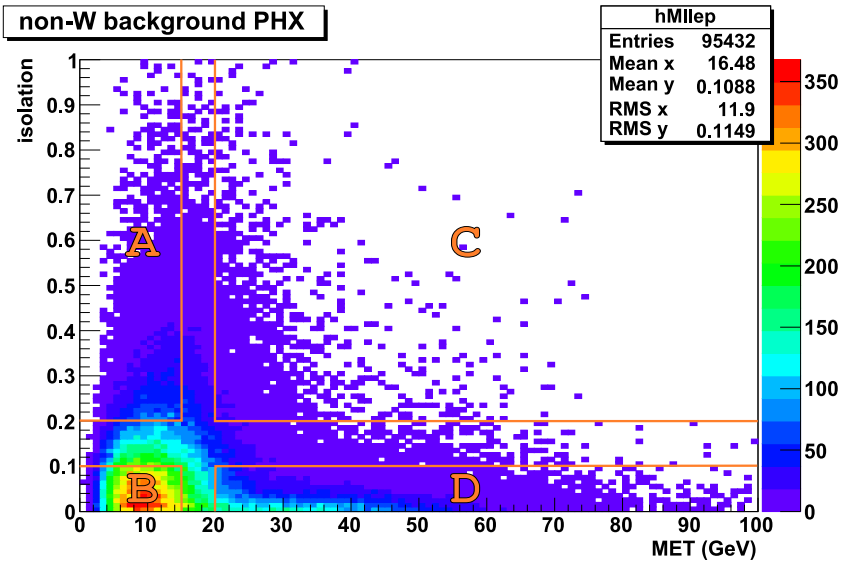

Figure 8.3: Isolation versus $\not\!\!E_T$ plot to estimate the non-W QCD background in PHX events.

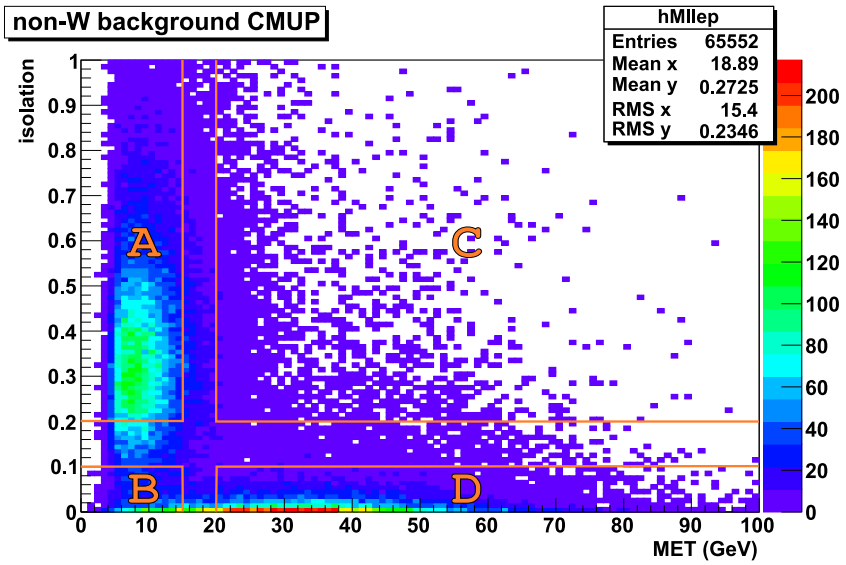

Figure 8.4: Isolation versus $\not\!\!E_T$ plot to estimate the non-W QCD background in CMUP events.

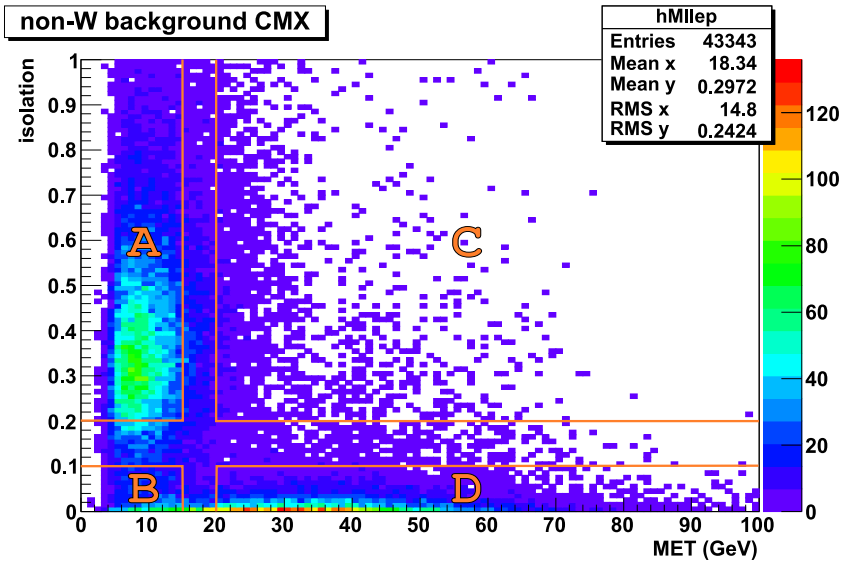

Figure 8.5: Isolation versus $\not\!\!E_T$ plot to estimate the non-W QCD background in CMX events.

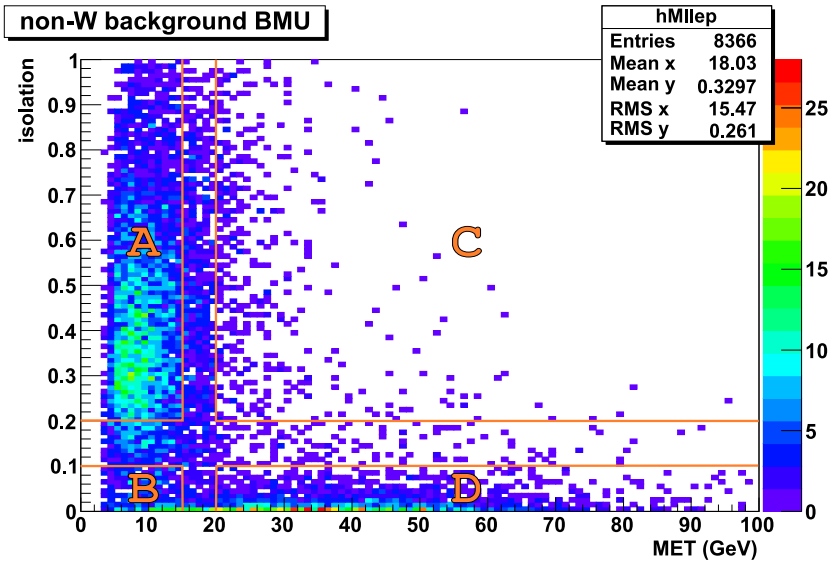

Figure 8.6: Isolation versus $\not\!\!E_T$ plot to estimate the non-W QCD background in BMU events.

The results of the $\mathcal{F}_{QCD}$ and ε_{QCD} calculations are given in Table 8.7. The lepton isolation versus $\not\!\!E_T$ plots are shown in Figures 8.2 to 8.6. As one can infer from Table 8.7, the forward leptons PHX and BMU suffer from a particularly significant non-W background. In the PHX case the lepton isolation versus $\not\!\!E_T$ suffers by a large systematic uncertainty. In the BMU case the uncertainties are also rather large and the difference between raw and corrected $\mathcal{F}_{QCD}$ is larger than one order of magnitude.

9. WZ Cross Section Limit

The final step in this counting experiment is to measure the cross section or put a limit to it. The total integrated luminosity used for the analysis is 1.375 fb^{-1}

9.1 The Maximum Likelihood Procedure

Since "method 2" exploits two constraints to extract the signal contribution and the renormalized W+multijet rate, one could in principle solve (8.1) with respect to $\mathcal{N}_{WZ}$ and $\mathcal{N}_W$ to get the result. However, the parameters in (8.1) define curves in the $\mathcal{N}_{WZ} \times \mathcal{N}_W$ plane which are subject to large errors. Therefore one should better take into account their uncertainty and shoot for cross section bands. The procedure adopted to extract the number of signal events exploits a likelihood to be maximized. The chosen likelihood is composed by two parts: the first one $\mathcal{L}_{bin}$ takes into account the binomial behavior of counting candidate $WZ \to \ell\nu b\bar{b}$ in pretagged data, the second one $\mathcal{L}_{par}$ accounts for the errors in the normalization constraints.

$\mathcal{L}_{bin}$ is defined from the overall probability of counting M_{data} events out of N_{data} events as determined by a per-event probability $\mathbf{p}$ which is function of the efficiencies ε_i and of the sample composition:

$$\mathcal{L}_{bin} = \mathbf{p}^{M_{data}} \cdot (1-\mathbf{p})^{N_{data}-M_{data}} \quad . \tag{9.1}$$

$\mathbf{p}$ is called "tagging probability per event" and is defined as the weighted mean of the various ε_i over the sample composition:

$$\mathbf{p} = \varepsilon_{WZ} \cdot \frac{\mathcal{N}_{WZ}}{N_{data}} + \sum_{EW} \varepsilon_{EW} \cdot \frac{N_{EW}}{N_{data}} + \left(\sum_{HF} \varepsilon_{HF} \mathcal{F}_{HF} + \frac{\not{M}}{N_{data}} \left(1 - \sum_{HF} \mathcal{F}_{HF} \right) \right) \cdot \frac{\mathcal{N}_W}{N_{data}} + \varepsilon_{QCD} \cdot \mathcal{F}_{QCD}^{corr} \tag{9.2}$$

where the $\mathcal{F}_{HF}$ have already been rescaled by the HF calibration factor $\mathbb{K}_{HF}$. The pretagged data normalization constraint is introduced in (9.2) with the approximation of $\mathcal{N}_{WZ} \ll \mathcal{N}_W$:

$$\mathcal{N}_W \simeq N_{data} \cdot (1 - \mathcal{F}_{QCD}) - \sum_{EW} N_{EW} \quad . \tag{9.3}$$

The only unknown in $\mathbf{p}$ is $\mathcal{N}_{WZ}$. All parameters defining $\mathbf{p}$ except for $\mathcal{N}_{WZ}$ and N_{data} are assumed to show a gaussian behavior. $\mathcal{L}_{par}$ is therefore given by a product of Gaussians, one for

	CEM	PHX	CMUP	CMX	BMU	total
N_{data}	31628	18063	15484	9177	1592	75944
M_{data}	183	143	100	41	18	485
$\not\!\!M$	49.2	34.57	22.50	12.20	4.14	122.6
$\sigma_{\not\!\!M}$	1.2	0.92	0.74	0.51	0.30	1.8

Table 9.1: Pretagged and tagged data events with dijet invariant mass in the Z mass window, and predicted mistagged events.

each of the parameters defining **p**:

$$\begin{aligned}\mathcal{L}_{par} &= \prod_{EW}\left(\mathcal{G}(\varepsilon_{EW},\bar{\varepsilon}_{EW},\sigma_{\varepsilon_{EW}})\cdot\mathcal{G}(N_{EW},\bar{N}_{EW},\sigma_{N_{EW}})\right)\cdot \\ &\quad \prod_{HF}\left(\mathcal{G}(\varepsilon_{HF},\bar{\varepsilon}_{HF},\sigma_{\varepsilon_{HF}})\cdot\mathcal{G}(\mathcal{F}_{HF},\bar{\mathcal{F}}_{HF},\sigma_{\mathcal{F}_{HF}})\right)\cdot \\ &\quad \mathcal{G}(\varepsilon_{QCD},\bar{\varepsilon}_{QCD},\sigma_{\varepsilon_{QCD}})\cdot\mathcal{G}(\mathcal{F}_{QCD}^{corr},\bar{\mathcal{F}}_{QCD}^{corr},\sigma_{\mathcal{F}_{QCD}^{corr}})\cdot \\ &\quad \mathcal{G}(\not\!\!M,\bar{\not\!\!M},\sigma_{\not\!\!M})\cdot\mathcal{G}(\varepsilon_{WZ},\bar{\varepsilon}_{WZ},\sigma_{\varepsilon_{WZ}})\ ,\end{aligned} \tag{9.4}$$

with the same conventions of (7.4). Overlined values in (9.4) are those predicted or measured according to the prescriptions of Chapter 8. The extraction of $\mathcal{N}_{WZ}$ is performed by minimizing with MINUIT

$$-2\ln\mathcal{L}_{tot} = -2\ln\mathcal{L}_{bin} - 2\ln\mathcal{L}_{par} \tag{9.5}$$

During the minimization procedure $\mathcal{N}_{WZ}$ is free to fluctuate in the $[-N_{data},N_{data}]$ range while all variables characterizing $\mathcal{L}_{par}$ are constrained to fluctutate within $\pm2\sigma$ around their central value. The range chosen for $\mathcal{N}_{WZ}$ allows negative values to take into account statistical fluctuations in small tagged samples. The input value in the minimization procedure for $\mathcal{N}_{WZ}$ is the one given by SM. The chosen $\pm2\sigma$ intervals include the contributions of Φ_T, theoretical/measured cross sections, systematic uncertainties on $\mathcal{F}_{QCD}$ and luminosity[(1)]. Since the HF calibration factor $\mathbb{K}_{HF}$ is not known, the uncertainties on the $\mathcal{F}_{HF}$ used in the fluctuation are statistical only. As it is desirable to understand if such a measurement is limited by the amount of collected data or by the systematic uncertainties, one should be able to separate them as much as possible. However this is not easy because of the way how the likelihood is defined. In order to allow appropriately for a good fluctuation of the parameters it would be best to take as σ their total uncertainty. The final uncertainty obtained this way from the likelihood accounts for the statistical fluctuations as well as for the effects of the sources of systematic uncertainties included in the likelihood itself ("external inputs" such as Φ_T, cross sections and luminosity). The effects of these "external inputs" are checked at a second time by shifting their central value of $\pm\sigma$ and repeating the procedure. In addition, the effects of other sources of systematic uncertainties which are not included in the likelihood, such as trigger efficiencies/lepton ID SF, are studied separately in a similar way.

As some of the different data samples corresponding to the various lepton types contain only a small number of candidate $Z\to b\bar{b}$ events, one should combine them in order to make optimal

[(1)] $\sigma_{\mathcal{L}}/\mathcal{L} = 6\%$.

$\mathbb{K}_{HF}$	best estimate	65% CL interval	95% CL interval
0.90	22.2	$[13.7, 31.1]$	$[5.7, 40.6]$
0.95	18.9	$[10.5, 27.8]$	$[2.6, 37.1]$
1.00	15.7	$[7.5, 24.5]$	$[-0.3, 33.8]$
1.05	12.7	$[4.5, 21.3]$	$[-3.2, 30.5]$
1.10	9.7	$[1.6, 18.3]$	$[-5.9, 27.4]$
1.15	6.8	$[-1.1, 15.3]$	$[-8.5, 24.3]$
1.20	4.1	$[-3.8, 12.4]$	$[-11.1, 21.3]$
1.25	1.8	$[-6.3, 9.6]$	$[-13.5, 18.4]$
1.30	-1.2	$[-8.8, 6.9]$	$[-15.9, 15.5]$

Table 9.2: Best estimate of the WZ production cross section and of the 68% and 95% CL limits for different values of $\mathbb{K}_{HF}$, which is assumed errorless. Cross sections are in pb.

use of the information. $-2\ln\mathcal{L}_{tot}$ is scanned by points for each lepton type as a function of the WZ production cross section in the $[-38, 200]$ pb in steps of 1 pb. While the cross section is fixed, $-2\ln\mathcal{L}_{tot}$ is minimized against all other parameters. The values obtained are summed over the five lepton types for each value of the WZ production cross section:

$$-2\ln\mathcal{L}_{tot}^{GLOB} = -2\sum_{LEP}\ln\mathcal{L}_{tot}^{LEP} \quad . \tag{9.6}$$

The behavior of $-2\ln\mathcal{L}_{tot}^{GLOB}$ around the minimum is parametrized with a polynomial of 4th degree $-2\ln\mathcal{L}_{tot}^{GLOB}(\sigma_{WZ}) \approx p_4(\sigma_{WZ})$. The limits at 68% CL or 95% CL are obtained from the values of the WZ production cross section corresponding to:

$$\begin{aligned} 68\%CL: &\quad p_4(\sigma_{WZ}) = p_4(\sigma_{WZ})|_{\min} + 1 \quad , \\ 95\%CL: &\quad p_4(\sigma_{WZ}) = p_4(\sigma_{WZ})|_{\min} + 4 \quad . \end{aligned} \tag{9.7}$$

9.2 Results and Overview of Systematic Uncertainties

Since the calibration factor $\mathbb{K}_{HF}$ is subject to a large uncertainty and has not been directly measured or extrapolated for the jet selection used in this work, the likelihood maximization procedure is repeated for different errorless values of $\mathbb{K}_{HF}$ in the $[0.90, 1.30]$ by steps of 0.05. The likelihood shapes are shown in Figure 9.1 and the results are listed in Table 9.2 and Figure 9.2.

In order to get a limit on the cross section one should choose a value for $\mathbb{K}_{HF}$. Other CDF groups, working on WH or single top production, normalize the W+jets background to data in the 1-jet bin to get the HF calibration factor to be used in the 2-jets bin. The value obtained this way is higher than those listed in Section 8.3: $\mathbb{K}_{HF} = 1.4 \pm 0.4$ [56]. The two numbers are compatible within one σ and $\mathbb{K}_{HF} = 1.0 \pm 0.3$ is chosen as reference value for the presented estimates. Since the jet selection is different, the appropriate value for the selected sample is likely to be to some extent different. The impact of such a difference on the estimated WZ production cross section

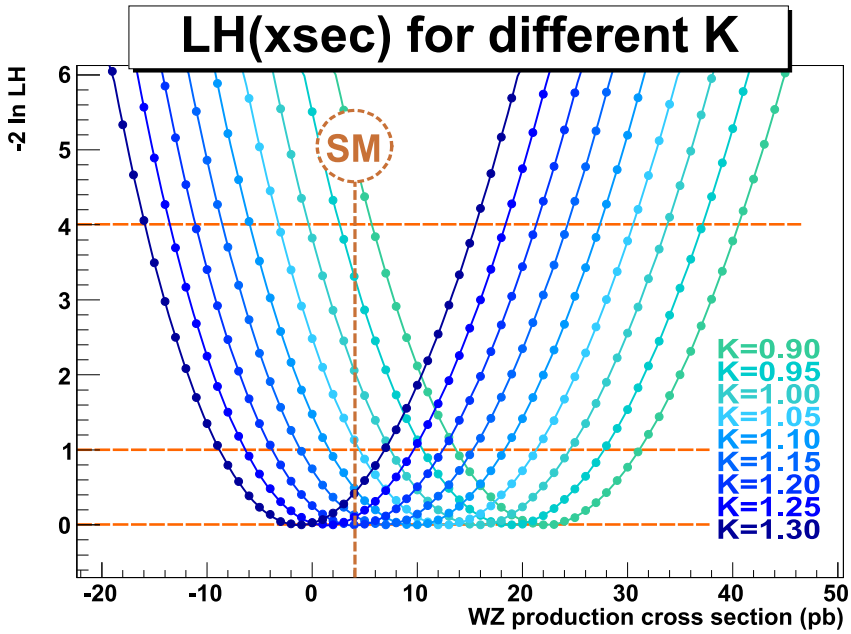

Figure 9.1: Behavior of $-2\ln\mathcal{L}_{tot}^{GLOB}$ as a function of WZ production cross section for different values of $\mathbb{K}_{HF}$, which is assumed errorless in this calculation.

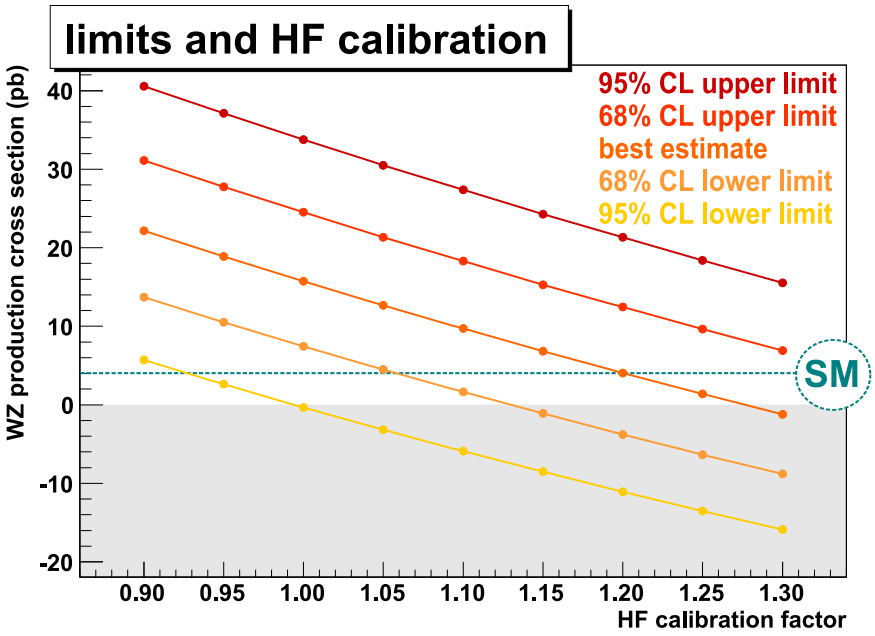

Figure 9.2: Best estimate of the WZ production cross section and of the 68% and 95% CL limits for different values of $\mathbb{K}_{HF}$, which is assumed errorless in this calculation.

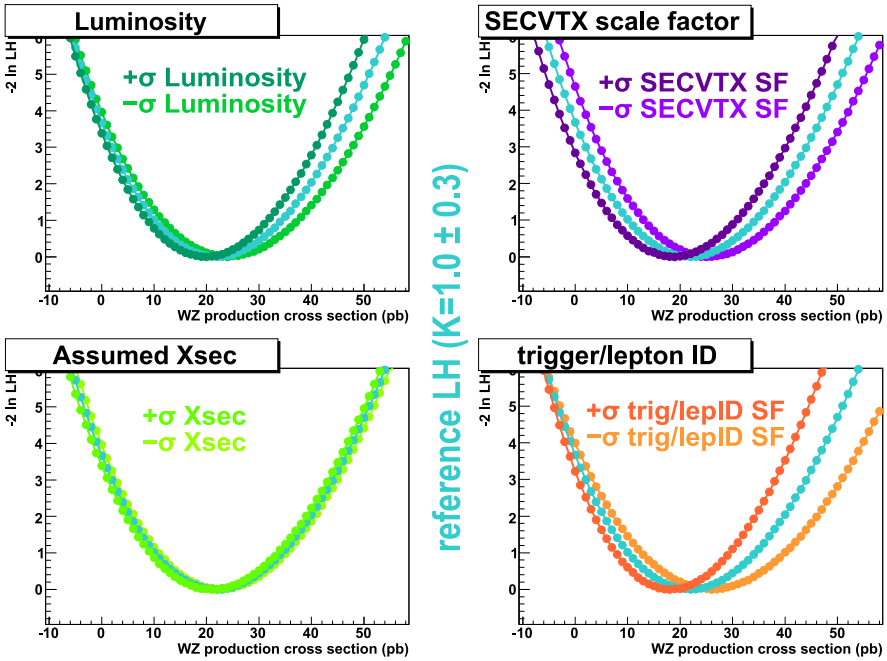

Figure 9.3: Evaluation of the contribution to the total uncertainty from uncertainty on integrated luminosity, Φ_T, assumed cross sections and trigger efficiency/lepton ID scale factor. Variations are shown with respect to the reference result for $\mathbb{K}_{HF} = 1.0 \pm 0.3$.

can be inferred from the previously described results. The likelihood maximization is repeated including the contribution of the uncertainty on the reference $\mathbb{K}_{HF}$ in the range of fluctuation of the different $\mathcal{F}$. The results are listed in Table 9.3.

The effects of the systematics included in the likelihood are checked by shifting the central value of the parameters by their uncertainty and looking at the effect this has on the likelihood itself. The comparison is done with respect to the reference likelihood characterized by $\mathbb{K}_{HF} = 1.0 \pm 0.3$. The studied effects are those due to the uncertainty on integrated luminosity, Φ_T and cross sections used in the absolute background estimate. The same procedure is repeated for the uncertainty in trigger efficiencies and lepton ID scale factors, which are not included in the likelihood. The results are listed in Table 9.3 and shown in Figure 9.3.

Other sources of systematic uncertainty which are not included in the likelihood will require further study. This study was not performed at this time for lack of time and because priority was given to study the dominant impact of the uncertainty on $\mathbb{K}_{HF}$ on the measurement, as was previously shown. These additional sources of systematic uncertainty are:

- jet energy scale, both at L5 generic jet corrections and after specific jet corrections – this effect can estimated by shifting the energy of each jet by its uncertainty and repeating the procedure;

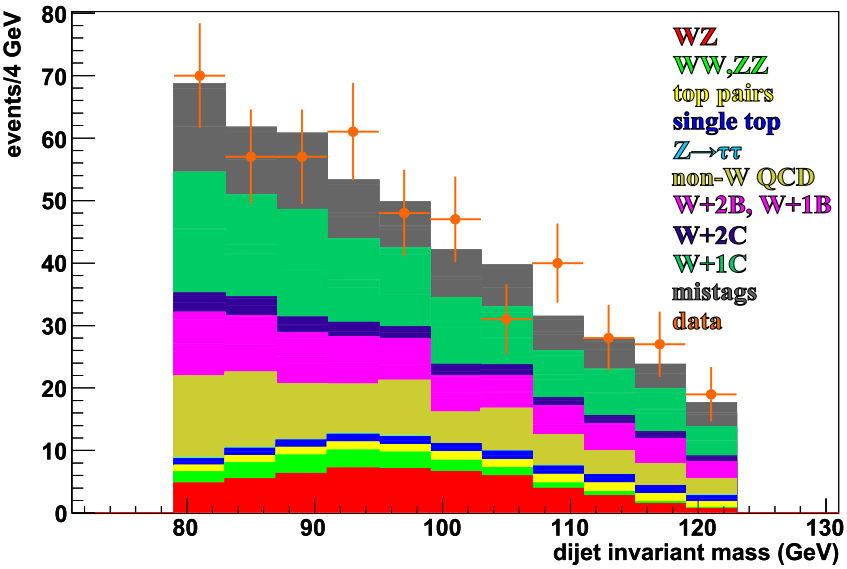

Figure 9.4: Dijet invariant mass in the Z-window after specific jet energy corrections of b-tagged events. Stacked colored histogram corresponds to MC while solid points represent data (non-W background shape is extracted from region "C" of the lepton isolation/MET plot). The weight of each part in the stack is given by the "method 2" estimate corresponding to the reference result with $\mathbb{K}_{HF} = 1.0 \pm 0.3$ (a best estimate of WZ cross section which is ~ 5 times larger than the SM expectation).

description	best estimate	65% CL interval	95% CL interval
$\mathbb{K}_{HF} = 1.0$ errorless	15.7	$[7.5, 24.5]$	$[-0.3, 33.8]$
$\mathbb{K}_{HF} = 1.0 \pm 0.3$ (ref.)	21.8	$[10.1, 34.3]$	$[-0.9, 47.7]$
$-\sigma$ integrated $\mathcal{L}$	24.1	$[11.6, 37.4]$	$[-0.1, 51.6]$
$+\sigma$ integrated $\mathcal{L}$	19.8	$[8.8, 31.6]$	$[-1.6, 44.2]$
$-\sigma$ SECVTX Φ_T	25.3	$[13.1, 38.3]$	$[1.7, 52.2]$
$+\sigma$ SECVTX Φ_T	18.7	$[7.3, 30.8]$	$[-3.3, 43.7]$
$+\sigma$ cross sections	22.6	$[10.9, 35.2]$	$[-0.1, 48.6]$
$+\sigma$ cross sections	21.0	$[9.2, 33.5]$	$[-1.7, 46.8]$
$+\sigma$ trigger/lepton ID SF	26.0	$[12.7, 40.0]$	$[0.0, 54.9]$
$+\sigma$ trigger/lepton ID SF	18.2	$[7.7, 29.4]$	$[-1.9, 41.5]$

Table 9.3: Evaluation of the effects of some sources of systematic uncertainty. Best estimate of the WZ production cross section and of the 68% and 95% CL limits for $\mathbb{K}_{HF} = 1.0 \pm 0.3$ are in pb.

- parton shower simulation – this effect can be checked by recalculating the relevant acceptances and efficiencies for the signal and the main backgrounds with a parton shower simulator different from PYTHIA (e.g. HERWIG);
- simulation of initial and final state radiation – this effect can be checked by recalculating the relevant acceptances and efficiencies for the signal and the main backgrounds in dedicated MC simulations with different ISR/FSR;
- parton distribution functions chosen in the simulation – this effect can be estimated by recalculating the relevant acceptances and efficiencies for the signal and the main backgrounds in dedicated MC simulations using different PDFs.

10. Conclusions and Prospects

Within the described framework and considerations, the 95% CL upper limit on the WZ production cross section, extracted with 1.375 fb^{-1} CDF data of high p_T lepton triggers in the final state with a candidate $W \to \ell\nu$ and two jets with at least one secondary vertex b-tag, is 48 pb. The uncertainty of the order of 50% on the best estimate leading to this limit is mainly statistical, while systematic uncertainty is larger as determined by the uncertainty on $\mathbb{K}_{HF}$.

This preliminary study of WZ production in the $\ell\nu b\bar{b}$ final state provided important information and left important open questions as well. Even with larger statistics, one should strive to make progress on event reconstruction and background understanding, in order to reduce all sources of uncertainty and be able to reach an observation.

- The reconstruction of the Z mass should be included in order to get as sharp a mass peak as possible. By doing this one would maximize the chance of observing a WZ signal and at the same time reduce the overlap of the Z on the H if the Higgs boson is very light. As shown in Chapter 7, the availability of an efficient b-tagger capable of identifying semileptonic decays of b-hadrons inside b-jets is crucial to reduce the tails in the dijet mass distribution and to sharpen the mass peak.

- The specific jet energy corrections should be improved both in conception and implementation to get the correct mass scale[(1)].

- The knowledge of the data/MC b-tagger scale factor Φ_T has a strong impact on the WZ cross section measurement. Although a precise measurement of the cross section may not be vital after a mass peak is seen, it would be very important to prove that one is on the right path when hunting for a peak. A more precise measurement of Φ_T would be is needed.

- The $W + HF$ background must be understood more reliably than in the present "method 2" implementation. This background should be further reduced by optimizing the sample selection cuts and by including kinematical selection parameters.

[(1)] The improvement of the mass scale is important in view of the search for a mass peak. Recent results from the Tevatron reduced the mass range of the Standard Model Higgs as indirectly determined by loop corrections to the W mass and by direct search at LEP. Any discrepancy in case of evidence of Higgs boson would be indicative of new physics.

Possible future improvements of this search are primarily the determination of $\mathbb{K}_{HF}$ for the selected candidate sample, either from measurement as described in Section 8.3, or from normalizing to data in sideband regions, such as at different jet multiplicity or at very low and very high dijet invariant mass.

Assuming that both statistical and systematic uncertainty will scale down with $1/\sqrt{\int \mathcal{L} dt}$[(2)], with 8 fb^{-1} integrated luminosity at the end of Run II a 1.0-1.5σ effect in a counting experiment can be expected. To gain in significance, reach a 3σ effect and claim for evidence of the process a more powerful analysis, such as kinematical shape analysis or the implementation of a neural network discriminator between signal and background, will be needed.

[(2)]This can be assumed because most scale factors, particularly $\mathbb{K}_{HF}$, are extracted from data.

A. Other Jet Reconstruction Algorithms

A.1 Jet Reconstruction by Relative p_T Algorithm

While cone algorithms are based on the observation that jet components are correlated in space, relative p_T algorithms rely on their correlation in momentum. The CDF relative p_T algorithm is called `Kt` (Figure A.1):

1. each tower with $E_T > 1$ GeV is treated as a seed for the jet reclustering and identified by its four-momentum $E^\mu = E \cdot (1, \sin\theta \cdot \cos\phi, \sin\theta \cdot \sin\phi, \cos\theta)$;
2. a fixed value is given to a reference parameter D[(1)];
3. the quantity $d_i = p_{T_i}^2$ is calculated for each precluster i;
4. the quantity d_{jk} is calculated for each precluster pair (j,k):

$$d_{jk} = \min\left(d_j, d_k\right) \cdot \frac{(\eta_j - \eta_k)^2 + (\phi_j - \phi_k)^2}{D^2} \quad ; \tag{A.1}$$

5. given a (i,j,k) triplet with fixed i, $d_{min}^{ijk} = \min_{ijk}(d_i, d_{jk})$;
6. if there is a (j^*,k^*) pair for which $d_{min}^{ij^*k^*} = d_{j^*k^*}$, the j^* and k^* preclusters are merged and their four-momentum is added, if not, the i precluster is called then a jet;
7. the procedure is repeated until all preclusters are promoted to jets[(2)].

A.2 Jet Reconstruction by Other Algorithms

Besides `JetClu`, two other cone-based algorithms are currently being developed at CDF: the `Seedless` algorithm and the `MidPoint` algorithm. The `Seedless` algorithm is unsensitive to infrared and collinear QCD divergences, but the large E_T fraction left unclustered and the poor stability of the algorithm when the jet centroid is close to the border of a tower are still preventing

[(1)] At CDF the standard D values are 0.4, 0.7, 1.0: the best coherence between `JetClu` and `Kt` is found when $D = R$.
[(2)] By construction, the jets cannot overlap and no merging or splitting procedures are needed.

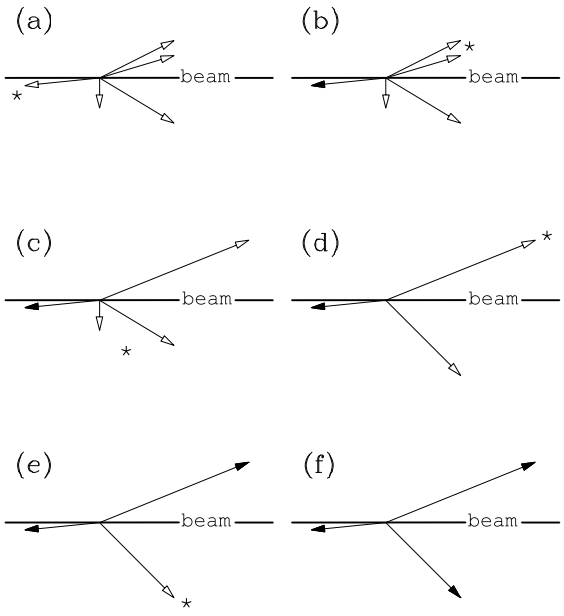

Figure A.1: Jet reconstruction by the `Kt` algorithm: for each step, a precluster classified as jet is marked with the black arrow and the (j,k) mergeable pair is marked with $\star$.

its implementation. The main difference between `JetClu` and the `Seedless` algorithm is that the latter one uses all nodes (vertices common to 4 towers in the $\eta \times \phi$ space) as initial seeds for "protojets". If the recalculated centroid falls out of the 4 towers identifying the node, it is rejected. Merging and splitting of jets are as in `JetClu`.

The `MidPoint` algorithm is also infrared safe but a fraction of the jet E_T can remain unclustered. The "protojet" identification is analogous to `JetClu` in as much as the centroid can move without restrictions during the iteration. If two protojets are closer than $2R$ in the $\eta \times \phi$ space, the middle point between the two centroids is used as centroid of a new protojet. The iteration is repeated until a stable solution is found. Merging and splitting of jets are as in `JetClu`.

B. Physical Properties of the Exploited Trigger Paths

Each trigger path is characterized by a sequence of requirements that detected physical objects must satisfy at the three trigger levels. Trigger paths contributing to the selected event sample are defined by[1]:

- `ELECTRON_CENTRAL_18`:

  L1: one trigger CEM tower with $E_T^{CEM} > 8$ GeV and one associated XFT track with $p_T^{XFT} > 8.34$ GeV;

  L2: in addition to L1, $E_T^{CEM} > 16$ GeV, $|\eta^{XFT}| < 1.317$, $p_T^{XFT} > 8$ GeV;

  L3: one reconstructed CEM object with $E_T > 18$ GeV associated to a COT track with $p_T^{COT} > 9$ GeV;

- `MET_PEM`:

  L1: one EM tower (CEM or PEM) with $E_T^{CEM} > 8$ GeV and raw $\not\!\!E_T > 15$ GeV;

  L2: in addition to L1, at least one PEM tower with $E_T^{CEM} > 20$ GeV;

  L3: one reconstructed PEM object with $E_T > 20$ GeV associated to a raw $\not\!\!E_T > 15$ GeV;

- `MUON_CMUP18`:

  L1: one trigger CMU segment with $p_T > 6$ GeV, associated CMP stubs and one associated XFT track with $p_T^{XFT} > 4.09$ GeV;

  L2: in addition to L1, confirmation of the availability of stereo COT segments in the track and $p_T^{XFT} > 14.77$ GeV;

  L3: one reconstructed CMUP muon with $p_T > 18$ GeV and distance on the transverse plane between the extrapolated COT track and CMU (CMP) hits less than 20 cm (10 cm);

- `MUON_CMX18`:

[1] Quoted objects are meant to be the minimum required.

L1: one trigger CMX segment with $p_T > 6$ GeV, trigger signal in CSX and one associated XFT track with $p_T^{XFT} > 4.09$ GeV;

L2: no requests in addition to L1;

L3: one reconstructed CMX muon with $p_T > 18$ GeV and distance on the transverse plane bewteen the extrapolated COT track and CMX hits less than 10 cm;

- `MUON_CMX18_L2_PT15`:

  L1: one trigger CMX segment with $p_T > 6$ GeV, trigger signal in CSX and one associated XFT track with $p_T^{XFT} > 4.09$ GeV;

  L2: in addition to L1, $p_T^{XFT} > 14.77$ GeV;

  L3: one reconstructed CMX muon with $p_T > 18$ GeV and distance on the transverse plane bewteen the extrapolated COT track and CMX hits less than 10 cm;

- `MUON_CMX18_&_JET10`:

  L1: one trigger CMX segment with $p_T > 6$ GeV, trigger signal in CSX and one associated XFT track with $p_T^{XFT} > 4.09$ GeV;

  L2: in addition to L1, confirmation of the availability of stereo COT segments in the track, $p_T^{XFT} > 14.77$ GeV and one jet with raw $E_T > 10$ GeV and $|\eta| < 3.6$; in this particular case the events are prescaled up to a factor 10 if the event rate is higher than the L3 processing capability;

  L3: one reconstructed CMX muon with $p_T > 18$ GeV and distance on the transverse plane bewteen the extrapolated COT track and CMX hits less than 10 cm;

- `MUON_CENTRAL_JET20_L1_BMU10_BSUR`:

  L1: one trigger IMU segment with $p_T > 10$ GeV and trigger signal in BSU;

  L2: in addition to L1, one jet with raw $E_T > 15$ GeV and $|\eta| < 1.1$;

  L3: one reconstructed `JetClu` jet with $R = 0.7$, $E_T > 20$ GeV and $|\eta| < 1.1$;

- `MUON_CENTRAL_JET20_L1_BMU10_PT11`:

  L1: one trigger IMU segment with $p_T > 10$ GeV, trigger signal in BSU and one associated XFT track with $p_T^{XFT} > 11.29$ GeV;

  L2: in addition to L1, one jet with raw $E_T > 15$ GeV and $|\eta| < 1.1$;

  L3: one reconstructed `JetClu` jet with $R = 0.7$, $E_T > 20$ GeV and $|\eta| < 1.1$.

C. Acceptance Tables

This Appendix lists the "acceptance tables" for the signal and the main backgrounds built from MC simulations. Each row corresponds to a step in the selection procedure and the number of events still present after the selection step is quoted. The row "other lepton vetoes" include the conversion veto for electrons, the cosmic veto and the χ^2 veto for muons. Selection up to "QCD veto" is the "pretag" one. Trigger selection step in MC is always satisfied. Effect of scale factors is not included.

lepton type	CEM	PHX	CMUP	CMX	BMU	all
initial	2333835	2333835	2333835	2333835	2333835	
good run list	2058054	2058054	2058054	2033837	2058054	
trigger	2058054	2058054	2058054	2033837	2058054	
tight lepton	112380	56898	64008	34489	26967	294742
MET	81429	39160	48677	26071	20561	215898
isolation	76291	37957	45658	24652	19623	204181
dilepton veto	67265	32505	39247	21056	16704	176777
Z veto	60582	29273	35803	19252	15229	160139
different inter. veto	58104	29273	35803	19252	15229	157661
other lepton vetoes	58101	29268	35802	19251	15184	157606
2 tight jets	16386	8944	10059	5647	4560	45596
1 tight + 1 loose jet	4702	2223	2979	1538	1172	12614
QCD veto	19848	10554	12119	6784	5470	54775
SECVTX	2260	1328	1305	733	657	6283
dijet mass window	1691	1020	984	567	505	4767

Table C.1: Acceptance table for the WZ signal (inclusive PYTHIA MC).

lepton type	CEM	PHX	CMUP	CMX	BMU	all
initial	2278552	2278552	2278552	2278552	2278552	
good run list	2014693	2014693	2014693	1990460	2014693	
trigger	2014693	2014693	2014693	1990460	2014693	
tight lepton	152683	62130	87415	43725	31784	377737
MET	133800	52965	75816	37851	27533	327965
isolation	124127	50938	70445	35398	25967	306875
dilepton veto	112391	45415	62997	31601	23045	275449
Z veto	108552	43727	61583	30895	22451	267208
different inter. veto	104382	43727	61583	30895	22451	263038
other lepton vetoes	104364	43727	61573	30894	22421	262979
2 tight jets	34173	14672	19785	9947	7315	85892
1 tight + 1 loose jet	8863	3835	5380	2736	1975	22789
QCD veto	41179	17751	23937	12099	8913	103879
SECVTX	1502	627	797	482	323	3731
dijet mass window	1105	462	568	359	244	2738

Table C.2: Acceptance table for the WW background (inclusive PYTHIA MC).

lepton type	CEM	PHX	CMUP	CMX	BMU	all
initial	2317502	2317502	2317502	2317502	2317502	
good run list	2045848	2045848	2045848	2021606	2045848	
trigger	2045848	2045848	2045848	2021606	2045848	
tight lepton	51167	25177	31358	16544	12789	137035
MET	18209	7629	15119	7841	6210	55008
isolation	16470	7264	14054	7333	5903	51024
dilepton veto	11923	4978	10173	5247	4360	36681
Z veto	5654	2363	6454	3424	2791	20686
different inter. veto	5009	2363	6454	3424	2791	20041
other lepton vetoes	5009	2363	6454	3424	2782	20032
2 tight jets	852	390	1301	698	587	3828
1 tight + 1 loose jet	276	121	342	209	158	1106
QCD veto	862	370	1400	791	634	4057
SECVTX	78	38	163	95	61	435
dijet mass window	40	22	122	67	49	300

Table C.3: Acceptance table for the ZZ background (inclusive PYTHIA MC).

lepton type	CEM	PHX	CMUP	CMX	BMU	all
initial	4719385	4719385	4719385	4719385	4719385	
good run list	4163778	4163778	4163778	4115328	4163778	
trigger	4163778	4163778	4163778	4115328	4163778	
tight lepton	391147	89501	237318	101019	58935	877920
MET	352392	80576	213587	91052	53288	790895
isolation	306174	76318	184183	79426	47868	693969
dilepton veto	270010	66066	160228	68696	41324	606324
Z veto	258246	63022	155770	66713	40081	583832
different inter. veto	247788	63022	155770	66713	40081	573374
other lepton vetoes	247756	63022	155739	66687	40048	573252
2 tight jets	18227	4700	11669	5073	2999	42668
1 tight + 1 loose jet	1782	472	1107	493	314	4168
QCD veto	18378	4642	11634	5072	3003	42729
SECVTX	10123	2678	6434	2840	1690	23765
dijet mass window	2827	749	1810	845	457	6688

Table C.4: Acceptance table for the $t\bar{t}$ background (inclusive PYTHIA MC).

lepton type	CEM	PHX	CMUP	CMX	BMU	all
initial	918173	918173	918173	918173	918173	
good run list	807912	807912	807912	798259	807912	
trigger	807912	807912	807912	798259	807912	
tight lepton	110007	27190	66107	29059	17562	249925
MET	98983	24110	58979	25966	15638	223676
isolation	89710	23053	53283	23487	14321	203854
dilepton veto	89030	22880	52890	23306	14214	202320
Z veto	88372	22707	52665	23209	14154	201107
different inter. veto	85489	22707	52665	23209	14154	198224
other lepton vetoes	85485	22706	52662	23207	14138	198198
2 tight jets	35603	9402	21949	9654	5788	82396
1 tight + 1 loose jet	5380	1648	3118	1436	1017	12599
QCD veto	38553	10260	23478	10379	6315	88985
SECVTX	22076	5917	13351	6052	3631	51027
dijet mass window	6560	1935	3904	1814	1132	15345

Table C.5: Acceptance table for the single top/s-channel background (forced $W \to \ell\nu$ MadEvent+PYTHIA MC).

lepton type	CEM	PHX	CMUP	CMX	BMU	all
initial	904783	904783	904783	904783	904783	
good run list	795952	795952	795952	786272	795952	
trigger	795952	795952	795952	786272	795952	
tight lepton	101807	31234	58620	27266	18382	237309
MET	91468	27893	52242	24376	16400	212379
isolation	85660	26732	49070	22747	15337	199546
dilepton veto	85168	26560	48794	22636	15248	198406
Z veto	84020	26259	48499	22490	15157	196425
different inter. veto	81320	26259	48499	22490	15157	193725
other lepton vetoes	81316	26255	48495	22486	15129	193681
2 tight jets	29702	8309	17916	7981	4987	68895
1 tight + 1 loose jet	10435	3506	6126	2900	1986	24953
QCD veto	38419	10892	22977	10311	6546	89145
SECVTX	14575	4456	8976	3996	2653	34656
dijet mass window	3807	1342	2287	1069	752	9257

Table C.6: Acceptance table for the single top/t-channel background (forced $W \to \ell\nu$ MadEvent+PYTHIA MC).

lepton type	CEM	PHX	CMUP	CMX	BMU	all
initial	5849525	5849525	5849525	5849525	5849525	
good run list	5160403	5160403	5160403	5099859	5160403	
trigger	5160403	5160403	5160403	5099859	5160403	
tight lepton	160154	96227	83069	46658	37839	423947
MET	72748	42261	38807	21494	17146	192456
isolation	66343	40045	36576	20341	16346	179651
dilepton veto	64083	38916	35157	19566	15747	173469
Z veto	63480	38467	34935	19427	15631	171940
different inter. veto	59851	38467	34935	19427	15631	168311
other lepton vetoes	59843	38466	34933	19426	15611	168279
2 tight jets	22460	12839	13784	7342	5524	61949
1 tight + 1 loose jet	7362	5412	4220	2396	2114	21504
QCD veto	9454	5676	5281	2861	2353	25625
SECVTX	208	85	139	55	44	531
dijet mass window	70	28	54	15	19	186

Table C.7: Acceptance table for the $Z+1$ light quark background (forced $Z \to \tau^+\tau^-$ ALPGEN+PYTHIA MC).

lepton type	CEM	PHX	CMUP	CMX	BMU	all
initial	1003193	1003193	1003193	1003193	1003193	
good run list	884526	884526	884526	874292	884526	
trigger	884526	884526	884526	874292	884526	
tight lepton	266042	133731	16	9	9	399807
MET	228617	113483	14	8	8	342130
isolation	211199	108631	1	0	1	319832
dilepton veto	211105	108552	1	0	1	319659
Z veto	209105	107396	1	0	1	316503
different inter. veto	202352	107396	1	0	1	309750
other lepton vetoes	202335	107394	1	0	1	309731
2 tight jets	106488	57202	1	0	0	163691
1 tight + 1 loose jet	29169	15819	0	0	0	44988
QCD veto	132204	71259	1	0	0	203464
SECVTX	2531	1244	0	0	0	3775
dijet mass window	781	403	0	0	0	1184

Table C.8: Acceptance table for the $W+2$ light quarks background (forced $W \to e\nu$ ALPGEN+PYTHIA MC).

lepton type	CEM	PHX	CMUP	CMX	BMU	all
initial	998930	998930	998930	998930	998930	
good run list	880766	880766	880766	870496	880766	
trigger	880766	880766	880766	870496	880766	
tight lepton	622	512	147780	79829	62161	290904
MET	518	375	123897	67307	53061	245158
isolation	315	293	113876	62423	49401	226308
dilepton veto	307	254	113827	62398	49382	226168
Z veto	304	251	113242	62079	49106	224982
different inter. veto	139	251	113242	62079	49106	224817
other lepton vetoes	139	251	113236	62076	49060	224762
2 tight jets	69	115	59199	32366	25675	117424
1 tight + 1 loose jet	14	42	16127	8990	7223	32396
QCD veto	34	117	72972	40236	32011	145370
SECVTX	2	1	1415	774	604	2796
dijet mass window	0	1	436	225	202	864

Table C.9: Acceptance table for the $W+2$ light quarks background (forced $W \to \mu\nu$ ALPGEN+PYTHIA MC).

lepton type	CEM	PHX	CMUP	CMX	BMU	all
initial	1543768	1543768	1543768	1543768	1543768	
good run list	1361642	1361642	1361642	1345912	1361642	
trigger	1361642	1361642	1361642	1345912	1361642	
tight lepton	419067	202658	342	171	110	622348
MET	363273	172847	310	156	97	536683
isolation	333188	164966	5	5	3	498167
dilepton veto	332767	164714	5	2	3	497491
Z veto	330375	163414	5	2	3	493799
different inter. veto	319446	163414	5	2	3	482870
other lepton vetoes	319408	163413	5	2	3	482831
2 tight jets	90142	46509	1	1	0	136653
1 tight + 1 loose jet	43723	22834	3	0	0	66560
QCD veto	130716	67632	3	0	0	198351
SECVTX	31151	16269	1	0	0	47421
dijet mass window	10340	5606	0	0	0	15946

Table C.10: Acceptance table for the $W + b\bar{b} + 1$ light quark background (forced $W \rightarrow e\nu$ ALPGEN+PYTHIA MC).

lepton type	CEM	PHX	CMUP	CMX	BMU	all
initial	1505827	1505827	1505827	1505827	1505827	
good run list	1324809	1324809	1324809	1309085	1324809	
trigger	1324809	1324809	1324809	1309085	1324809	
tight lepton	1467	720	228129	121749	93638	445703
MET	1218	535	192840	103657	80344	378594
isolation	525	442	176046	95324	74738	347075
dilepton veto	496	380	175802	95194	74635	346507
Z veto	494	376	175057	94755	74263	344945
different inter. veto	229	376	175057	94755	74263	344680
other lepton vetoes	229	376	175042	94747	74201	344595
2 tight jets	74	107	48886	26700	20754	96521
1 tight + 1 loose jet	23	37	23975	12925	10197	47157
QCD veto	41	118	70789	38631	30231	139810
SECVTX	10	37	16650	9285	7309	33291
dijet mass window	3	11	5496	3162	2465	11137

Table C.11: Acceptance table for the $W + b\bar{b} + 1$ light quark background (forced $W \rightarrow \mu\nu$ ALPGEN+PYTHIA MC).

lepton type	CEM	PHX	CMUP	CMX	BMU	all
initial	1981125	1981125	1981125	1981125	1981125	
good run list	1745577	1745577	1745577	1724968	1745577	
trigger	1745577	1745577	1745577	1724968	1745577	
tight lepton	523364	265556	59	31	24	789034
MET	450745	226198	53	27	21	677044
isolation	415231	216314	4	3	0	631552
dilepton veto	415058	216180	2	0	0	631240
Z veto	411984	214411	2	0	0	626397
different inter. veto	398548	214411	2	0	0	612961
other lepton vetoes	398510	214408	2	0	0	612920
2 tight jets	116437	63056	1	0	0	179494
1 tight + 1 loose jet	60095	32615	0	0	0	92710
QCD veto	172438	93534	0	0	0	265972
SECVTX	10044	5253	0	0	0	15297
dijet mass window	3135	1744	0	0	0	4879

Table C.12: Acceptance table for the $W + c\bar{c} + 1$ light quark background (forced $W \to e\nu$ ALPGEN+PYTHIA MC).

lepton type	CEM	PHX	CMUP	CMX	BMU	all
initial	1973546	1973546	1973546	1973546	1973546	
good run list	1740998	1740998	1740998	1720448	1740998	
trigger	1740998	1740998	1740998	1720448	1740998	
tight lepton	1311	921	289936	156772	123673	572613
MET	1097	661	243306	132393	105861	483318
isolation	677	525	223107	122236	98673	445218
dilepton veto	652	460	223024	122186	98637	444959
Z veto	647	450	222011	121620	98177	442905
different inter. veto	294	450	222011	121620	98177	442552
other lepton vetoes	294	450	221998	121610	98078	442430
2 tight jets	102	137	64870	35479	28639	129227
1 tight + 1 loose jet	45	71	33458	18280	14937	66791
QCD veto	89	163	95539	52455	42606	190852
SECVTX	4	5	5534	3061	2469	11073
dijet mass window	2	2	1717	987	786	3494

Table C.13: Acceptance table for the $W + c\bar{c} + 1$ light quark background (forced $W \to \mu\nu$ ALPGEN+PYTHIA MC).

lepton type	CEM	PHX	CMUP	CMX	BMU	all
initial	1976289	1976289	1976289	1976289	1976289	
good run list	1744952	1744952	1744952	1724408	1744952	
trigger	1744952	1744952	1744952	1724408	1744952	
tight lepton	581108	253681	125	61	33	835008
MET	500265	202358	109	54	29	702815
isolation	455428	192788	11	8	2	648237
dilepton veto	455151	192625	6	3	2	647787
Z veto	450351	190566	6	3	2	640928
different inter. veto	435325	190566	6	3	2	625902
other lepton vetoes	435284	190563	5	2	2	625856
2 tight jets	88651	38190	0	0	0	126841
1 tight + 1 loose jet	27591	12212	0	0	0	39803
QCD veto	114628	48860	0	0	0	163488
SECVTX	4777	2054	0	0	0	6831
dijet mass window	1615	704	0	0	0	2319

Table C.14: Acceptance table for the $W+c+2$ light quarks background (forced $W \rightarrow e\nu$ ALPGEN+PYTHIA MC).

lepton type	CEM	PHX	CMUP	CMX	BMU	all
initial	1980410	1980410	1980410	1980410	1980410	
good run list	1743367	1743367	1743367	1722791	1743367	
trigger	1743367	1743367	1743367	1722791	1743367	
tight lepton	1703	1090	329742	167287	123172	622994
MET	1407	807	276399	139174	101452	519239
isolation	893	605	249743	127146	94044	472431
dilepton veto	857	512	249569	127068	93997	472003
Z veto	848	503	247987	126178	93409	468925
different inter. veto	461	503	247987	126178	93409	468538
other lepton vetoes	461	503	247968	126159	93325	468416
2 tight jets	104	113	50618	25515	18731	95081
1 tight + 1 loose jet	15	25	15579	7854	5943	29416
QCD veto	62	107	65159	32753	24089	122170
SECVTX	6	5	2745	1449	1014	5219
dijet mass window	1	4	912	491	349	1757

Table C.15: Acceptance table for the $W+c+2$ light quarks background (forced $W \rightarrow \mu\nu$ ALPGEN+PYTHIA MC).

Bibliography

[1] Particle Data Group: *Review of Particle Physics*
Jour. Phys. G **33**, 1 (2006)

[2] A. Seiden: *Particle Physics, A Comprehensive Introduction*
Addison Wesley (2004)

F. Halzen, A. D. Martin: *Quarks and Leptons: an Introductory Course in Modern Particle Physics*, John Wiley & Sons (1983)

[3] S. L. Glashow: *Partial Symmetries of Weak Interactions*
Nucl. Phys. **22**, 579 (1961)

J. Goldstone, A. Salam, S. Weimberg: *Broken Symmetries*
Phys. Rev. **127**, 965 (1962)

S. Weimberg: *A Model of Leptons*
Phys. Rev. Lett. **19**, 1264 (1967)

S. L. Glashow, J. Iliopoulos, L. Maiani: *Weak Interactions with lepton-hadron Symmetry*
Phys. Rev. D **2**, 1985 (1970)

[4] P. W. Higgs: *Broken Symmetries, Massless Particles and Gauge Fields*
Phys. Lett. **12**, 132 (1964)

P. W. Higgs: *Broken Symmetries and the Masses of Gauge Bosons*
Phys. Rev. Lett. **13**, 508 (1964)

P. W. Higgs: *Spontaneous Symmetry Breakdown Without Massless Bosons*
Phys. Rev. **145**, 1156 (1966)

[5] P. Duinker: *Review of e^+e^- physics at PETRA*
Rev. Mod. Phys. **54**, 325 (1982)

[6] T. Müller: *Production Properties of the Intermediate Vector Bosons W and Z at the CERN $p\bar{p}$ Collider*, CERN-EP/88-48, April 7, 1988

[7] The UA1 Collaboration: *Experimental observation of isolated large transverse energy electrons with associated missing energy at $\sqrt{s} = 540$ GeV*
Phys. Lett. B **122**, 103 (1983)

The UA2 Collaboration: *Observation of single isolated electrons of high transverse momentum in events with missing transverse energy at the CERN $\bar{p}p$ collider*
Phys. Lett. B **122**, 476 (1983)

[8] The UA1 Collaboration: *Experimental observation of lepton pairs of invariant mass around 95 GeV/c^2 at the CERN SPS collider*
Phys. Lett. B **126**, 398 (1983)

The UA2 Collaboration: *Evidence for $Z^0 \to e^+e^-$ at the CERN $\bar{p}p$ collider*
Phys. Lett. B **129**, 130 (1983)

[9] K. Hagiwara *et al.*: *Measuring the WWZ coupling at the Fermilab Tevatron*
Phys. Rev. D **41**, 2113 (1990)

[10] M. S. Neubauer: *Diboson Physics at the Tevatron*
hep-ex/0605066, Proceedings of XLI Réncontres de Moriond, QCD and HE hadronic interactions, La Thuile, Italy, March 18-25, 2006

J. Sjölin: *Diboson Physics at the Tevatron*
hep-ex/0605094, Proceedings of XLI Réncontres de Moriond, EW iteractions and unified theories, La Thuile, Italy, March 11-18, 2006

The DØ Collaboration: *Measurement of $W\gamma$ and $Z\gamma$ production in $p\bar{p}$ Collisions at $\sqrt{s} = 1.96$ TeV*, Phys. Rev. Lett. **94**, 211801 (2005)

The DØ Collaboration: *Limits on anomalous trilinear gauge couplings from $WW \to e^+e^-$, $WW \to e^\pm\mu^\mp$ and $WW \to \mu^+\mu^-$ events from $p\bar{p}$ collisions at $\sqrt{s} = 1.96$ TeV*
Phys. Rev. D **74**, 057101 (2006)

[11] The DØ Collaboration: *Production of WZ Events in $p\bar{p}$ Collisions at $\sqrt{s} = 1.96$ TeV and Limits on Anomalous WWZ Couplings*
Phys. Rev. Lett. **95**, 141802 (2005)

The CDF Collaboration: *Observation of WZ Production*
Phys. Rev. Lett. **98**, 161801 (2007)

[12] J. D. Degenhardt *et al.*: *Measurement of the $p\bar{p} \to WZ + X$ cross section at $\sqrt{s} = 1.96$ TeV and limits on WWZ trilinear gauge couplings*
DØ note 5417-CONF, August 7, 2007

P. Pétroff: *W and Z Physics at the Tevatron*
Presentation held at the XXIII International Symposium on Lepton and Photon Interactions at High Energy (LP07), Daegu, Korea, August 13-18, 2007

[13] The CDF Collaboration: *Limits on Anomalous Triple Gauge Couplings in $p\bar{p}$ Collisions at $\sqrt{s} = 1.96$ TeV*, hep-ex/07052247, to be published in Phys. Rev. Lett.

Anna Sfyrla: *Search for WW and WZ production in lepton-neutrino plus dijet final state at Run II using 1.29 fb^{-1} of data*

CDF note 8740, April 3, 2007
Presentation held at APS Meeting, Jacksonville, FL, April 14-17, 2007

[14] Fermilab Accelerator Division: *Documentation Web Page*
`http://beamdocs.fnal.gov/AD-public/DocDB/ListTopics`

[15] Fermilab Accelerator Division: *Details of Accelerator Chain*
`http://www-bd.fnal.gov/public/chain.html`

[16] R. Moore: *Performance and Future of the Tevatron*
Presentation held at Hadron Collider Physics (HCP 2007), La Biodola, Elba, Italy, May 21-25, 2007

[17] The CDF Collaboration: *The CDF II Detector Technical Design Report*
Fermilab Publication FERMILAB-PUB-96/390-E, October, 1996

The CDF Collabration: *Summary of the CDF RunII Detector Parameters*
`http://www-cdf.fnal.gov/internal/detectors/parameters.html`

[18] The CDF Collaboration: *Proposal for Ehnancement of the CDF II Detector: an Inner Silicon Layer and a Time of Flight Detector*
Fermilab Proposal FERMILAB-PROPOSAL-909 (and updates), October 23, 1998

[19] A. Sill: *CDF Run II silicon tracking projects*
Nucl. Instr. Meth. A **447**, 1 (2000)

M. C. Kruse: *Silicon Detector Upgrades for the Tevatron Run 2*
FERMILAB-CONF-02/253-E. Published Proceedings 31st International Conference on High Energy Physics (ICHEP 2002), Amsterdam, The Netherlands, July 24-31, 2002

[20] A. Affolder *et al.*: *Intermediate silicon layers detector for the CDF experiment*
Nucl. Instr. Meth. A **453**, 84 (2000)

[21] C. S. Hill: *Operational experience and performance of the CDFII silicon detector*
Nucl. Instr. Meth. A **530**, 1 (2004)

[22] A. Affolder *et al.*: *CDF Central Outer Tracker*
Nucl. Instr. Meth. A **526**, 249 (2004)

[23] Ch. Paus *et al.*: *Design and performance tests of the CDF time-of-flight system*
Nucl. Instr. Meth. A **461**, 579 (2001)

D. Acosta *et al.*: *A Time-of-Flight detector in CDF-II*
Nucl. Instr. Meth. A **518**, 605 (2004)

[24] R. D. Erbacher: *Calorimetry in CDF Run 2*
FERMILAB-CONF-02/251-E. Published Proceedings 31st International Conference on High Energy Physics (ICHEP 2002), Amsterdam, The Netherlands, July 24-31, 2002

S. Kuhlmann *et al.*: *The CDF calorimeter upgrade for Run IIb*
Nucl. Instr. Meth. A **518**, 39 (2004)

L. Breccia *et al.*: *Test of 2000 phototubes for the CDF endplug calorimeter upgrade*
Nucl. Instr. Meth. A **532**, 575 (2004)

[25] A. Artikov *et al.*: *CDF Central Preshower and Crack Detector Upgrade*
FNAL-PUB-07-023-E, June, 2007

[26] M. Albrow *et al.*: *The CDF plug upgrade electromagnetic calorimeter: test beam results*
Nucl. Instr. Meth. A **480**, 524 (2002)

[27] G. Apollinari *et al.*: *Shower maximum detector for the CDF plug upgrade calorimeter*
Nucl. Instr. Meth. A **412**, 515 (1998)

[28] M. Albrow *et al.*: *Intercalibration of the longitudinal segments of a calorimeter system*
Nucl. Instr. Meth. A **487**, 381 (2002)

[29] S. Cabrera *et al.*: *Making the most of aging scintillator*
Nucl. Instr. Meth. A **453**, 245 (2000)

A. Artikov *et al.*: *Design and construction of new central and forward muon counters for CDF II*, Nucl. Instr. Meth. A **538**, 385 (2005)

[30] D. Acosta *et al.*: *The CDF Cherenkov luminosity monitor*
Nucl. Instr. Meth. A **461**, 540 (2001)

D. Acosta *et al.*: *The performance of the CDF luminosity monitor*
Nucl. Instr. Meth. A **494**, 57 (2002)

[31] K. Goulianos, S. Lami: *Performance of a prototype position sensitive towerless calorimeter*, Nucl. Instr. Meth. A **430**, 34 (1999)

K. Goulianos *et al.*: *The CDF MiniPlug calorimeters*
Nucl. Instr. Meth. A **496**, 333 (2003)

K. Goulianos *et al.*: *The CDF MiniPlug calorimeters at the Tevatron*
Nucl. Instr. Meth. A **518**, 42 (2004)

[32] G. Gómez-Ceballos *et al.*: *Event Builder and Level 3 at the CDF experiment*
Nucl. Instr. Meth. A **518**, 522 (2004)

[33] A. Bardi *et al.*: *SVT: an online Silicon Vertex Tracker for the CDF upgrade*
Nucl. Instr. Meth. A **409**, 658 (1998)

W. Ashmanskas *et al.*: *The CDF online Silicon Vertex Tracker*
Nucl. Instr. Meth. A **485**, 178 (2002)

W. Ashmanskas *et al.*: *The CDF Silicon Vertex Trigger*
Nucl. Instr. Meth. A **518**, 532 (2004)

[34] F. D. Snider *et al.*: *Tracking at CDF: Algorithms and experience from Run I and Run II*
Nucl. Instr. Meth. A **566**, 133 (2006)

F. Bedeschi: *Tracking and alignment basics*
CDF note 6743, October 28, 2003

[35] P. Azzi *et al.*: *Histogram tracking in the COT*
CDF note 5562, February 21, 2001

[36] B. R. Ko *et al.*: *SVXII Stand-alone Tracking*
CDF note 6440, May 7, 2003

[37] K. Bloom, W. M. Yao: *"Outside-In" Silicon Tracking at CDF*
CDF note 5991, June 5, 2002

C. Hays *et al.*: *Inside-out tracking at CDF*
Nucl. Instr. Meth. A **538**, 249 (2005)

[38] J. Goldstein *et al.*: *Silicon Tracking for Plug Electrons*
CDF note 5970, May 16, 2002

[39] The CDF Collaboration: *Topology of three-jet events in $p\bar{p}$ collisions at $\sqrt{s} = 1.8$ TeV*
Phys. Rev. D **45**, 1448 (1992)

G. C. Blazey *et al.*: *Run II Jet Physics*
CDF note 5293, April 18, 2000

[40] G. Latino: *Calorimetric Measurements in CDF: a New Algorithm to Improve the Energy Resolution of Hadronic Jets*
Ph. D. Thesis, Università di Cassino, 2001

[41] A. Bhatti *et al.*: *Determination of the jet energy scale at the Collider Detector at Fermilab*
Nucl. Instr. Meth. A **566**, 375 (2006)

J. Adelman *et al.*: *Generic Jet Scale Corrections for Run II*
CDF note 7358, December 12, 2005

[42] C. Neu: *CDF b-tagging: Measuring Efficiency and False Positive Rate*
International Workshop on Top Quark Physics, Coimbra, Jan 2006; in Proc. of Science

T. Wright: *B-Tagging at CDF and D0, Lessons for LHC*
FERMILAB-CONF-06-313-E. Published Proceedings Symposium on Hadron Collider Physics (HCP 2006), Durham, North Carolina, May 22-26, 2006

[43] F. Garberson *et al.*: *Combination of the SecVtx 1.2 fb^{-1} b-Tagging Scale Factors*
CDF note 8666, March 13, 2007

[44] L. Cerrito, A. Taffard: *A Soft Muon Tagger for Run II: Summer-04 Version*
CDF note 7122, July 19, 2004

A. Abulencia *et al.*: *Measurement of $p\bar{p} \rightarrow t\bar{t}$ production cross section in the l+jets SLT muon tagged sample with 760 pb^{-1}*
CDF note 8482, September 28, 2006

[45] E. P. Cortesón: *Measurement of the $t\bar{t}$ production cross section in $p\bar{p}$ collisions at $\sqrt{s} =$ 1.96 TeV using lepton+jets events in the CDF detector at Fermilab*
Ph. D. Thesis, Universidad de Cantabria, 2007

[46] The CDF Collaboration: *Measurement of the $t\bar{t}$ production cross section in $p\bar{p}$ collisions at $\sqrt{s} = 1.96$ TeV using lepton + jets events with secondary vertex b-tagging*
Phys. Rev. D **71**, 052003 (2005)

H. Bachacou *et al.*: *Heavy Flavor Contributions to the SECVTX-tagged W+Jets Sample*
CDF note 7007, July 30, 2004

A. Foland *et al.*: *Preliminary Method 2 Backgrounds for Top Pair Production in Lepton Plus Jets Events with SECVTX Using 318.5 pb^{-1} of $p\bar{p}$ Data*
CDF note 7486, July 13, 2005

S. Budd *et al.*: *Measurement of the $t\bar{t}$ Production Cross Section in SECVTX-Tagged Lepton + Jets Events*, CDF note 8037, February 15, 2006

[47] M. Franklin *et al.*: *Heavy-Flavor Content of the W+Jets Sample*
CDF note 8765, April 10, 2007

M. Franklin *et al.*: *Method 2 Backgrounds for 1.12 fb^{-1} Lepton+Jets Analyses*
CDF note 8766, April 10, 2007

M. Franklin *et al.*: *Measurement of the Top Pair Cross Section in Lepton+Jets in 1.12 fb^{-1}*
CDF note 8767, April 10, 2007

[48] J. F. Arguin, P. K. Sinervo: *Revisiting the Top Specific Jet Energy Corrections*
CDF note 6404, December 15, 2003

N. Yang, P. K. Sinervo: *Effects of Using Top Quark Mass Specific Jet Energy Corrections on Top Quark Mass Measurement*
CDF note 8020, January 4, 2006

[49] M. Matsumoto, T. Nishimura: *Mersenne Twistor: A 623-dimensionally equidistributed uniform pseudorandom number generator*
ACM Transactions on Modeling and Computer Simulation, **8**, 3 (1998)

[50] CDF Top Group: *Method 2 Workshop*
Presentations held at the CDF Method 2 Workshop, Fermilab, May 11, 2007

[51] CDF Lepton Working Group: *Scale Factors Web Page*
`http://www-cdf.fnal.gov/internal/physics/joint_physics/leptons/SF/list.html`

[52] The CDF Collaboration: *First Measurements of Inclusive W and Z Cross Sections from Run II of the Tevatron Collider*
Phys. Rev. Lett. **94**, 091803 (2005)

The CDF Collaboration: *First Measurement of the Ratio of Central-Electron to Forward-Electron W Partial Cross Sections in $p\bar{p}$ Collisions at $\sqrt{s} = 1.96$ TeV*
Phys. Rev. Lett. **98**, 251801 (2007)

[53] A. D. Martin *et al.*: *Uncertainties of predictions from parton distributions: Theoretical errors*, Eur. Phys. J. C **35**, 325 (2004)

P. J. Sutton *et al.*: *Parton distributions for the pion extracted from Drell-Yan and prompt photon experiments*
Phys. Rev. D **45**, 2349 (1992)

P. J. Rijken, W. L. van Neerven: *Order α_S^2 contributions to the Drell-Yan cross section at fixed target energies*
Phys. Rev. D **51**, 44 (1995)

R. Hamberg, W. L. van Neerven, T. Matsuura: *A complete calculation of the order α_S^2 correction to the Drell-Yan K-factor*
Nuclear Physics B **359**, 343 (1991)

[54] M. Franklin *et al.*: *Calibration of Heavy-Flavor Production in QCD Data*
CDF note 8768, April 10, 2007

[55] S. Budd, T. Junk, C. Neu: *SECVTX Mistag Parameterization for winter 2006*
CDF note 8072, February 2, 2006

S. Budd *et al.*: *Tight, Loose and Ultratight SECVTX Tag Rate Matrix with 1.2 fb^{-1}*
CDF note 8519, December 13, 2006

[56] F. Cannelli *et al.*: *Evidence for Single Top Quark Production in 1.51/fb of CDF Data using the Matrix Element Technique*
CDF note 8968, August 20, 2007

Acknowledgements

During this long and challenging experience I frequently dealt with accidents I went through thanks to the generous help of many people. I never met some of them and their help was therefore particularly appreciated.

I would like to thank Mark Neubauer, the CDF Diboson Group and Mark Kruse for the care they showed in my progress and needs and for sharing their expertise with me, especially Anna Sfyrla, who always found the time to bear and answer my ingenuous questions with a very kind smile. I am grateful to Sarah Budd, Jon Efron and Christopher Neu (who spent encouraging words for me) for enlighting me about the misteries of SECVTX and mistag matrix. I would like to thank Daniel Sherman, who gave me frequent feedbacks when I compared my "method 2" implementation with the results of his $t\bar{t}$ cross section measurement, Charles Plager and Kevin Lannon who helped me in fixing my event selection, Valentin Necula, Craig Group and Doug Benjamin, who produced fast some MC samples "on demand" and all the people who provided me with miscellaneous information. I owe Gabriele Compostella a beer and that's all.

I feel grateful to Marco Trovato, who shared with me the hardest moments of these months and promptly told me useful news, Guram Chlachidze, who was always capable of finding time to listen to my doubts when I was at Fermilab, and professor Tarcisio Del Prete, who enlighted me about some troubling statistical issues. Michele Giunta, connoisseur of good music (*"... e la morale è sempre quella ..."*), and Giuseppe Latino, my true guru about jets and jet corrections, were my source of ideas and alternative points of view to understand what was going on when things were driving me nuts and never let me feel alone: thank you very much!

Last, but not least, my leading team: Gueorgui Velev who gave me the starting push, checked the most troublesome bugs of my codes and at last managed to include me among his thousands commitments, and Giorgio Bellettini who has followed my growth since three years ago. He put me in the condition of doing unusual experiences, followed my steps, carefully revised this thesis and listened to me showing deep interest even when he was not supposed to.

After "professional" acknowledgments, I cannot forget the human help I got from my parents Greta and Olvrado and all my relatives who reminded me I could make it and never complained about my choices and my being far away from home in consequence of them. I was lucky I had many friends supporting me during these five years, and now their minute of glory comes

too. I hope I did not forget any ...: Silvietta, Daniela, Dario, Sandrino, Piero, Cecilia, Roberto, Giovanna, Charlie, Anna, Pierpa, Nicola CC, Paolino, el Mysa, John, Pigo, Alessio, Kork, Mæz, Fuso, Vitto, Poppi, Kov, il Sire, Nico e tutto il Settimo (HERI, HODIE, SEMPER!), Ely, Cicca, Orgio, Nino e Paola, Eugenio, Rebe, Franz, Giulia, il Colonnello, Pier, Lù, Vale, Isa, la Pater, Diego, Enrico, il Biondo, Giacomino, Giovanni, Luca, Markov, Matteo, Mircea, Rosa, Stefano, Giopiz, Veronica, tutti i seguaci del "biribiri", Giuseppe e Lorella, Arnaldo e Luigina, Daniele, Flores e il Ren-Bu-Kan, Ennio, Dean, Frank, el capitan de la compagnia, Jake & Elwood and 'Ggricoltore Agricolo, che dà consilli e non sballia mai!

A final special thought is for Francesca and Roberto: if I wrote this thesis, it is their fault too.